Breast Cancer Detection Using Microwaves and Microwave-Thermography Techniques

by

Dawood Alsaedi

A thesis
presented to the University of Waterloo
in fulfillment of the
thesis requirement for the degree of
Doctor of Philosophy
in
Electrical and Computer Engineering

Waterloo, Ontario, Canada, 2021

Examining Committee Membership

The following served on the Examining Committee for this thesis. The decision of the Examining Committee is by majority vote.

External Examiner:	Emily Porter Assistant Professor, Electrical & Computer Engineering The University of Texas at Austin
Supervisor(s):	Omar M. Ramahi Professor, Dept. Electrical & Computer Engineering University of Waterloo
Internal Member:	Zhou Wang Professor, Dept. Electrical & Computer Engineering University of Waterloo
	Bo Cui Professor, Dept. Electrical & Computer Engineering University of Waterloo
Internal-External Member:	Eihab Abdel-Rahman Professor, Dept. System Design Engineering, University of Waterloo

Author's Declaration

I hereby declare that I am the sole author of this thesis. This is a true copy of the thesis, including any required final revisions, as accepted by my examiners.

I understand that my thesis may be made electronically available to the public.

Abstract

The accelerated growth in Microwave Imaging (MWI) and Microwave Detection (MWD) is driven by microwave ability to penetrate materials that are considered opaque at a shorter wavelength. This elevates MWI potential to cover a wide range of applications, including but not limited to: security checking; civil and industrial operations; and medical diagnostics. Involving microwaves in the biomedical field relies on two additional microwave features: a) a microwave interacts differently with biological tissue, based on the tissue's electrical properties; and b) a microwave is considered as non-ionizing radiation, thus it presents low to no risk to biological tissue. This has instigated the implementation of microwaves in different areas of biomedical diagnostics, such as brain haemorrhages, meniscus tears, and breast cancer detection.

The first part of this dissertation presents a microwave thermography hybrid breast cancer detection technique consists of a microwave radiation source, an infrared heat detector, and a machine learning algorithm. Since many conventional MWI approaches collect transmission signals along with reflected signals, this technique is based on recording the electromagnetic wave after passing through the entire breast. A sensitive film is placed behind the breast (opposite direction of the radiation source) to absorb the transmitted wave that propagates according to the dielectric properties of the breast tissue. The captured heat pattern is used as a guide for determining the presence of an anomaly within the breast tissue. Machine learning is used to enhance the detection accuracy and to provide further information about the tumor's features, such as size and location. The proposed modality shows a capability to detect and determine the size and location of an artificial tumor with a 5 mm radius and a 2:1 permittivity contrast with normal tissue.

A new breast cancer detection modality that uses a metasurface as the imaging medium and a microwave radiation source is introduced in the second part of this thesis. In contrast with previous microwave imaging techniques, or imaging techniques in general, instead of providing an image of the internal breast tissue (i.e., a slice/cut through the breast), the proposed technique provides an impression of the breast tissue. The impression which, in principle, is similar to the impression captured by an x-ray film, is captured by a metasurface, which is an ensemble of electrically-small resonators. Each cell records the strength of the incident power that impinges on it. This metasurface may be viewed as analogous to a low-frequency scaling of the x-ray film. The metasurface receives the transmitted energy through the breast, which resembles the mammography approach. While mammography faces a major challenge in detecting tumors in dense breasts, the metasurface proposed here utilizes a low frequency radiation source, thus allowing higher penetration through dense breast tissue. Similar to the first part of the thesis, by building a proper machine

learning code, the detection capability is then enhanced by engaging a Convolution Neural Network (CNN) to determine the tumor's features.

In the third part of this thesis, flexible-conformal metasurface films are introduced for utilization as a wearable breast cancer detection modality. This technique involves two metasurface arrays with electrically small and closely spaced resonators as a transmitter and receiver. The microwave radiation of the metasurface transmitter is received at the other side of the breast by the metasurface receiver to form an image of the received electromagnetic power. The receiver is expected to provide an electromagnetic energy pattern instead of an image that represents the breast's internal contents. The power pattern is influenced differently according to the electrical properties of the breast tissue, thus a unique power impression can be obtained for both a healthy breast and a breast that contains a cancerous tumor. By using flexible metasurface films, the antenna number-penetration-resolution trade-off that limits the capability of conventional MWI techniques can be minimized. In addition, the necessity for antenna miniaturization to enhance the resolution can be avoided, and the long mechanical scan can be replaced with just a few scanning steps of the metasurface sheet.

Acknowledgements

First and foremost, all praises are due to Allah for giving me the guidance and the strength to accomplish this work. My sincere thanks to Allah for surrounding me with family and friends who have been so supportive during this journey.

I want to express my deepest gratitude to my supervisor Prof. Omar M. Ramahi. I want to express my thanks for his supervision, encouragement, and support during my Ph.D. years.

I would also like to deliver my sincere gratitude to the committee members, Prof. Eihab Abdel-Rahman, Prof. Emily Porter, Prof. Bo Cui, and Prof. Zhou Wang, for reviewing my thesis, serving my Ph.D. defense, and for providing invaluable feedback.

My sincere acknowledgment to my previous and current colleagues, Abdulrahman Alorinan, Mohamed El Badawe, Abdulbaset Ali, Mohammed AlShareef, Ali Albishi, Melad Olaimat, and Youcef Chaouche for their support and encouragement.

Myconvey my unparalleled gratitude to my dear parents and siblings for their endless support throughout this academic journey. I owe a debt of gratitude to my wife for her infinite patience, support, and inspiration to achieve my goals. Wordless thanks to my kids, who are the source of encouragement and strength.

Last but not least, Special thanks to Taif University, Saudi Arabia, for financially supporting this work.

Dedication

This is dedicated to my parents, wife, siblings, and kids.

Table of Contents

List of Figures

List of Abbreviations

CNN Convolution Neural Network v, viii, ix, xii, xiv, 13, 27, 37–41, 50, 61–66, 70

ELC Electric Inductive Capacitive xiii, xv, 53–55, 57, 74, 75, 77, 80

IR infrared 4, 8–10, 25, 27

LIT lock-in thermography 42, 45

MRI Magnetic resonance imaging 2, 13, 24, 61

MT Microwave Thermography 9, 10

MWD Microwave Detection iv, 4, 24

MWI Microwave Imaging iv, v, xi, 3–5, 7, 8, 13, 24, 36, 74, 83, 87

MWT Microwave tomography 4–7

NDT Non-Destructive Tests 8–10

OUT Object Under Test xi, 29, 51, 52

UWB Ultrawideband 7, 8

List of Tables

بِسْمِ اللَـهِ الرَحمَـن الرَحيمِ

In the name of Allah, the most Gracious, the most Merciful

Chapter 1

Introduction

1.1 Overview

According to a report from the World Health Organisation, approximately 2.3 million women developed breast cancer in 2020, while approximately 685,000 deaths occurred on a global level, which makes this the world's most prevalent cancer [1]. The Canadian Cancer Society predicted that, in the same year, 109,600 women would be diagnosed with cancer, with the expected number of breast cancer cases reaching 27,400, which is 25% of overall female cancer cases. Moreover, it is expected that every day approximately 14 Canadian women will die from breast cancer [2]. Fig. 1.1 illustrates the U.S. statistics that estimate that, in 2021, 281,550 new cases of breast cancer will be diagnosed, and that 43,600 women are expected to die from breast cancer [3]. In addition, 1 in 8 Canadian and U.S. females are estimated to be diagnosed with breast cancer over the course of their life, making breast cancer the most likely cancer among Canadian females compared to other types [2, 3].

X-ray mammography is the most common breast screening technique used for breast cancer detection. Although mammography has a short testing time and high resolution imaging, several limitations decrease its detection capability. In dense breasts, mammography has difficulty in distinguishing between healthy and malignant tissue since both appear with no contrast on the image [4]. Moreover breast cancer studies report up to 25% of undetectable cancer tumors (false negatives) using the mammography method [5]. In addition to this limitation, x-ray mammography is considered as an ionizing radiation that may cause harmful effects on the human body [6]. Finally, some patients experience

a painful compression in the breast during mammography testing [7].

Magnetic resonance imaging (MRI) is a non-ionizing technique that can be used for breast imaging. MRI utilizes pulsing radio waves with the presence of a magnetic field that can provide a high resolution medical image. The resulting valuable image of high density breast tissue cannot be achieved by x-ray mammography. Moreover, MRI can detect a small cancerous tumor that could not otherwise be detected by other breast imaging techniques [8, 4]. However, MRI is a very expensive and time consuming diagnosis technique, hence it is used as a complementary tool for x-ray mammography to confirm the presence of a tumor in the breast [9].

Ultrasound (sonography) is another imaging method that is used for breast cancer detection. In this technique, sound waves are sent through the breast and the reflected waves are reconstructed to form an image of the tissue layers of the breast, hence normal and malignant tissue can be determined. Although this is a convenient technique from the patient perspective, and is also low cost, ultrasounds are not used individually for breast imaging since they cannot detect some forms of cancerous tumors [2, 10]. Therefore, as in MRI, this technique is used to complement x-ray mammography in the case of dense breasts, in order to improve the sensitivity of the imaging system [11].

The microwave technique, which utilizes the wave in the microwave range, is another proposed (still not medically available) method for breast cancer screening. The detection principle of the microwave technique is based on the difference in electrical properties between normal and malignant breast tissue [12]. During screening, the breast is illuminated by electromagnetic waves that have the capability to partially penetrate the breast tissue (depending on the frequency and material properties). A part of these waves is reflected or scattered, depending on the electrical properties of each tissue. The reflected and scattered waves are collected using antennas to reconstruct the geometrical and/or dielectric map of the breast tissue [13]. Since this imaging technique is considered as non-ionizing and non-invasive, it has attracted significant development that has resulted in 3D imaging data. Compared to other breast imaging techniques, it is very low cost. However, many challenges come with microwave imaging, such as mismatching at air-skin interface, which results in a remarkable effect on both image quality and accuracy [4]. The reconstruction of the data requires a specific algorithm that has a significant impact on image quality. In addition, the size of the antennas (receivers) has to be small to allow for increasing the number of antennas in the system, hence more information can be collected. However, in general, a smaller antenna means using a higher frequency, which has lower penetration

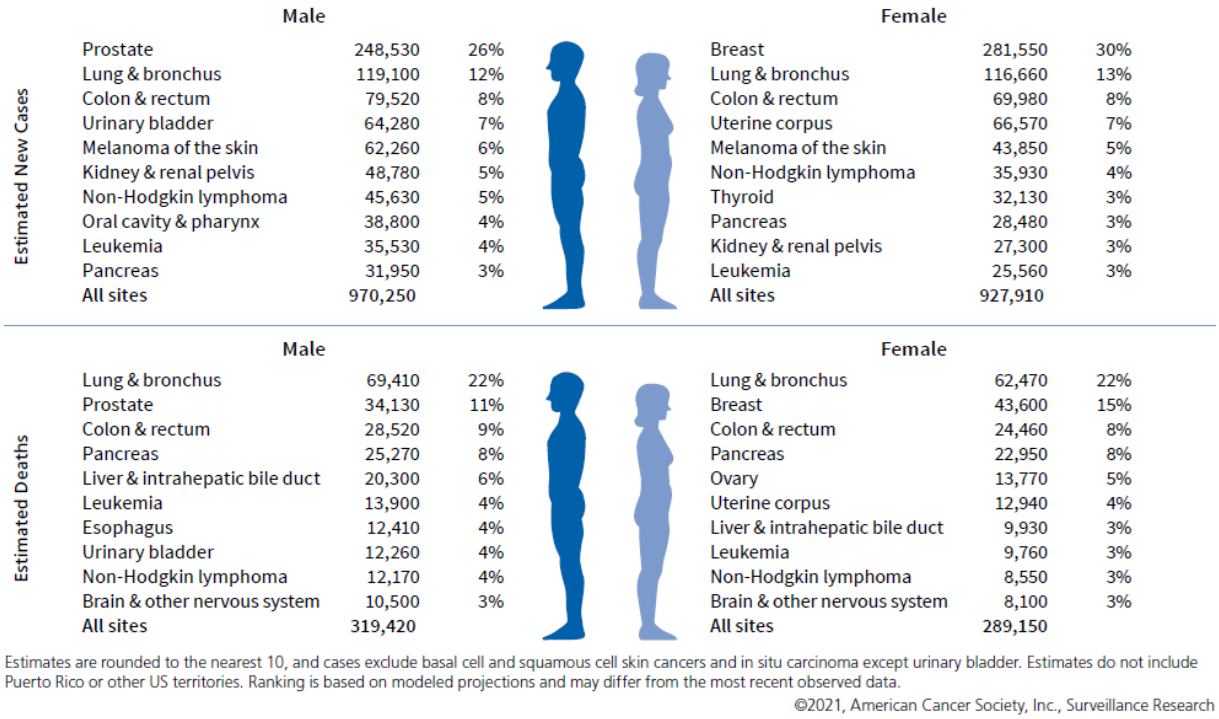

Figure 1.1: US cancer statistics for new cancer cases and deaths.

capability for breast tissue. Moreover, increasing the number of antennas causes a mutual coupling between the adjacent elements. In the microwave-imaging system, this results in a trade-off between image resolution and antenna size [4].

1.2 Microwave Imaging for Breast Cancer Detection

The limitations of detection capability, harmful radiation components, and the expensive access cost of recent breast imaging modalities introduce MWI as an promising alternative breast cancer detection technique. MWI is based on the variation in electrical properties between healthy and cancerous breast tissue over the microwave frequency range. The scattered microwave is expected to be influenced by the difference in electrical properties that will be collected to build an image of the internal breast tissue construction. Ex vivo studies report that the significant differences in water content between healthy and malignant breast tissue result in a contrast in dielectric properties [14, 15, 16, 17, 18]. The

stated healthy-to-malignant electromagnetic property variation ratio in biological breast tissue ranges from 10% up to 300%, which is sufficient to form the detection principle of microwave imaging or detection techniques [19, 20]. Utilizing this variation in electromagnetic properties, extensive investigation and development in MWI and MWD techniques have been conducted, both numerically and experimentally. MWI studies reported a non-ionizing and non-invasive 3D imaging modality for breast cancer detection at a lower cost compared to other breast imaging modalities [21, 22, 23, 24, 25].

The experimental implementation of MWI has taken several forms and can be classified into three categories: passive, active, and hybrid as seen in Fig 1.2. Passive MWI utilize a radiometry device to detect the variation on the temperature between healthy and cancerous tissue which develops higher temperature than the rest of the breast tissue [26, 27, 28]. In active MWI, the breast is subjected to radiation by electromagnetic wave in microwave regime and the scattered wave is collected to form an image of the internal breast tissue. Different scattering signals results from the healthy and malignant tissue due to the contrast in the electrical properties [29, 30]. The hybrid approach utilized two different radiation and detection tools for breast cancer detection. A microwave source is used to illuminate the breast whereas an ultrasound transducer is used to record the acoustic waves that is radiated by breast tissue. As a result of the higher conductivity of the malignant tissue compared to the healthy tissue, higher electromagnetic energy is absorbed, hence a higher acoustic waves radiation occurs [31, 32].

1.2.1 Microwave Tomography Technique

Active microwave imaging can be typically divided into two categories: tomography and radar-based microwave imaging, as shown in Fig 1.2. The Microwave tomography (MWT) technique utilizes the reflected microwave signal from the breast to form an image that reconstructs the dielectric (permittivity and conductivity) profile of breast tissue. Reconstructing the image is accomplished by solving the inverse scattering problem that estimates the absorbed and scattered signals from the internal breast tissue. This technique provides the quantitative features of the cancerous tissue, such as the size and location of the tumor [33, 34].

Several studies into breast cancer detection investigate the capability of the MWT technique, theoretically, experimentally, and clinically [35, 36, 37, 38, 39]. A group from Dartmouth College in the USA was one of the earliest research groups to implement MWT for breast cancer detection [40, 41, 42]. In 2000, Meaney et al. [35] introduced the first clinical prototype system using infrared (IR) for breast cancer detection. An array of 16

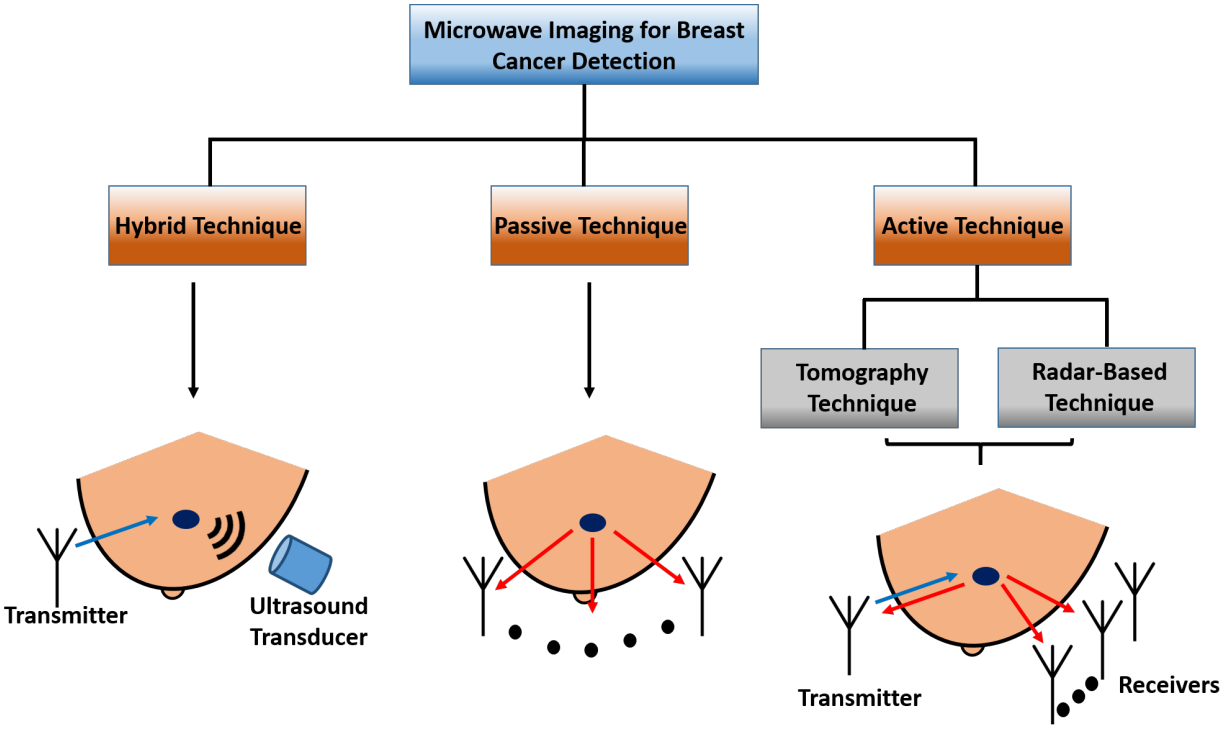

Figure 1.2: Schematic diagram of the classification and approaches of MWI for breast cancer detection.

monopole antennas was utilized in this system to work as a transmitter or receiver in an operation frequency range between 300–1000 MHz. The advantage of using monopole antenna comes from the ability of high radiation in lossy medium and the simplicity in modelling for a 2D imaging problem. The antenna array was arranged in a circular configuration and placed underneath a bed that has a hole into which the patient's breast is inserted. A coupling medium was filled between the breast and the antenna to reduce any noise. The clinical trial was performed on five patients with an exam time up to 30 minutes per patient. The achieved results constructed 2D images of the permittivity and conductivity of the breast tissue.

The Dartmouth College group spent several years improving the algorithm and the hardware of this clinical prototype [21, 43, 44]. In 2013, based on finite element modelling (FEM), a 3D MWT system was introduced for the first time [21]. The challenges in the previous prototype were overcome by improving the algorithm and the hardware of this version. An array of 16 monopole antennas was divided into two groups, controlled

separately by using a motor to precisely position the antennas. The achieved results demonstrate the capability of the proposed system to detect a tumor size down to 1 cm inside the breast of a patient. The system screens each breast within two minutes, with a data processing time of about 20 minutes, which is considered very fast compared to the ten hour processing time that is reported in [45].

A preclinical MWT prototype system to provide 2D breast screening images was reported by Son et al. [46]. The system has 16 monopole antennas that merge inside a tank where liquid is used to reduce the mismatching that occurs at the air-skin interface. The elements are used as a receiver and transmitter over a frequency that extends from 0.5 GHz to 3 GHz. The tumor in this study is represented by a pipe, filled with a liquid that has complex permittivity comparable to a realistic tumor. The system exhibits a high resolution and capability of reconstructing 2D images for a breast phantom that contains single or multiple tumors with diameters of 5 mm and 10 mm.

Aiming to reduce the cost of the system and enhance the image reconstruction time, Pagliari et al. [47] proposed a breast cancer detection prototype based on MWT. The drop in cost is a result of using off-the-shelf components and in-house fabricated antennas, while the fast image reconstruction is a result of using a field-programmable gate array instead of a multicore CPU to execute the imaging algorithm. The breast phantom is a cylindrical plastic dielectric that is filled with a glycerin-water mixture, where the tumor is represented by a smaller-radius cylinder containing different material. The operation frequency of the system ranges from 1.4 to 1.6 GHz, which is considered to be a narrow bandwidth, since the low cost components are compatible with this frequency range. The system executed the algorithm 20 times faster compared to a conventional powerful multicore CPU. Moreover, the system showed a detection accuracy that is comparable to the accuracy that can be accomplished by an expensive vector network analyzer. Another recent attempt to reduce processing time was conducted using an algorithm based on 2-D discrete dipole approximation [48]. The reconstruction time was reduced from 140 seconds to about 6 seconds which also reduces the required memory space.

Jeon et al. [49] developed a clinical trial MWT system that operates in a frequency range between 3 to 6 GHz and utilizes a fast forward reconstruction algorithm. Using the proposed system, 15 patients, aged from 40 to 68 years, were subjected to the screening. The test was a non-blind test involving five patients who were diagnosed previously as having normal breast tissue and ten with tumor presence. The reconstructed images show an abnormality inside the breast of one of the patients, already known to have a tumor inside her left breast. Comparing the resulting breast images with previous mammogram images and biopsy data, five doctors from Seoul National University Hospital identified one false positive case and one false negative case.

1.2.2 Radar-Based Microwave Technique

Radar-based microwave imaging utilizes a scattered signal and provides a map of the scattered signal that results from different breast tissue. Unlike MWT, radar-based MWI does not reconstruct the dielectric properties map of the breast tissue. The radar-based MWI approach can be divided into five techniques: MWI via space-time (MIST); confocal microwave (CM); multi-static adaptive (MSA); time domain data adaptive (TDDA); and tissue sensing adaptive radar (TSAR).

Several research groups have investigated the feasibility of radar-based MWI for breast cancer imaging. Hagness et al. [50] introduced a confocal microwave technique for early-stage breast cancer detection. The achieved results show the capability of the system to detect a tumor size of about 3.2 mm at depth of up to 3.72 cm. The system utilizes the 2D CMI and 3D CMI approach, which shows a different detection accuracy. The limitations in this approach were solved by developing a delay multiply-and-sum signal processing that enhances the resolution and interface rejection. Intensive research was later conducted by this group to develop their radar-based MWI for breast cancer detection [51, 52, 53, 54].

Fear et al. [55] reported a tissue sensing adaptive radar to detect cancerous tumors inside the breast. In this study, a PVC pipe with a spherical piece of wood represented the breast skin and the cancerous tumor, respectively, while the breast tissue was represented by air. This system faced some challenges that are attributed to the significant reflection that results from breast skin. However, the system obtained promising results that prove the feasibility of tissue sensing adaptive radar for breast cancer detection. More recently, they developed a clinical prototype derived from a monostatic radar-based system [56]. Reflection from the skin was solved by passing the data through a circuit to filter any noise. The patients were required to lie face down on a bed, designed with a hole for the breast. The system was designed to horizontally and vertically scan the antenna around the breast during measurements. The reconstructed images were compared to the patients' previously-obtained magnetic resonance (MR) images. The microwave images showed results that were consistent with the MR images down to a tumor size of 5 mm diameter.

A group from the University of Bristol reported a hemi-spherical antenna array for an Ultrawideband (UWB) radar imaging for breast cancer detection. The array of patch antenna consisted of 16 patch antennas positioned tangentially to the surface of a spherical plastic container that held a breast phantom. The antenna was designed to radiate over a frequency range from 4 GHz to 10 GHz and have a reflection coefficient lower than -5 over this frequency range. The system was able to detect a 1cm tumor with a 10mm shift in tumor position in one direction [57]. The system was improved to reduce the size of the

antenna and to take a symmetrical 4x4 curved geometry shape. Under the same frequency range, the operation sequence of the antenna pairs was controlled by electromechanical switches. The developed system successfully detected a 4 mm diameter tumor that was positioned in different locations [58]. More recently, a clinical prototype system for breast cancer detection, based on multi-static UWB radar, was introduced [59]. The system consists of a real aperture antenna array comprised of 31 cavity-backed UWB antennas that are attached to part of a half-spherical container. The experimental exams were conducted using realistic breast phantoms and real patients who had already been diagnosed with breast cancer. The achieved results were promising regardless of the fact that a large tumor was detected as multiple objects rather than as one object.

Porter et al. [60] proposed a microwave breast cancer detection technique that, for the first time, was based on multi-static radar and time-domain measurements. The system has an array that contains 16 antennas, connected to the surface of a hemispherical bowl that has 16 holes to host the elements. The operation of the system involves a switching network to arrange the operation sequence where one antenna is used as a transmitter while each of the remaining 15 antennas acts as a receiver, until each antenna is used as a transmitter. The breast is presented by a realistically shaped phantom filled with fat-like material and with a tumor inserted inside the fat. A tumor of less than 1 cm radius was successfully detected in different locations inside the breast phantom with a localization error in two axes in 2-D images. More recently, a clinical prototype wearable radar-based MWI system was developed. The prototype was based on multistatic time-domain radar, and comprised of 16 wearable antennas attached to a bra. In contrast with conventional MWI prototypes, this system provides much less complexity and footprint, and requires no exam table nor coupling liquid. Healthy patients were subjected to testing over 28 days using the wearable system and the reconstructed images show high consistency over the examination period (28 days) [61].

1.3 Thermography

In photography, light (made up of photons) is used to create an image. Similarly, heat is used in thermography to create a thermal image. The evolution of thermography comes from its ability to capture the thermal distribution along an object without contact. Therefore, the idea of IR thermography has been generated to capture the thermal radiation that is emitted from a targeted object, which leads to form a thermal image of that object [62].

For several years, IR thermography has made significant contributions in different applications. It has been utilized in Non-Destructive Tests (NDT) that are used to detect the

defects in materials and in devices such as photovoltaic cells [63]. Moreover, identification of the thermal properties of material can be conducted using IR thermography. Monitoring in advanced security and health issues heavily relies on IR thermography which provides important results that cannot be achieved by using other methods [64]. IR thermography can also be used to map the electromagnetic field of the microwave to realize the field intensity distribution for antennas [65, 66, 67]. The large number of applications of IR thermography is a consequence of advantages such as: fast measurement time; non-contact testing; and ease of processing data. In addition, the improvement in IR thermographic tools has led to quantitative as well as qualitative results, which gives greater preference to this technique [65].

The approaches of IR can be generally classified into two main types: active and passive [68, 69]. In the passive method, the IR camera captures the thermal distribution of the object with no external influencer. Passive thermography utilizes material that has a distinctive temperature compared to the surrounding environment In contrast, in the active method, since some objects have no difference between their temperature and the surrounding environment, an external excitation source is required to provide thermal contrast to the object under test. This method is utilized to detect the deeper defects in materials. The excitation source is placed in the same or opposite side of the IR camera, depending on a number of factors, such as material type and thickness.

Passive thermography leads to qualitative results that can detect the presence of an abnormal object in the tested material. These results present in the form of different thermal distributions compared to the rest of the material. The active thermography allows qualitative and quantitative diagnosis that can give more information about the size and depth of defects in the material. The specimen in the passive method is produced internally and the IR camera is located in front of the radiation side of the object. The active thermography relies on an external excitation source since no heat is generated from the specimen. Therefore, the heat either reflects from the specimen, where the IR camera and the excitation source are placed at the same side or transmits through it, where the IR camera is placed at the opposite side from the excitation source. It is worth mentioning that the reflection method is preferred for detecting defects that are close to the surface of the object, whereas the transmission method is preferable when a deep inspection is needed.

In 1986, Sega and Norgard [70] were among the first researchers to experiment with using Microwave Thermography (MT) to measure the electromagnetic fields near the apertures of planar and cylindrical structures. This study ignited attention by using microwaves combined with IR thermography as a significant technique for NDT. Levesque et al. later conducted an experiment to detect the artificial defects on glass-epoxy composites [71].

In this experiment, the excitation source was a parabolic and horn antenna to provide microwave heat to the specimen. The thermal distribution on the specimen's surface was detected using an IR camera with a capturing range of 8μm to 12μm.

A study in 1995 performed an experiment to detect defects in non-metallic composite material. Two types of cavities, with power of 600-1700W, were used as excitation sources [72]. The results, which were compared with other techniques such as x-ray and ultrasound, found that MT can be effectively evaluated as a NDT technique.

Utilizing the deep penetration of microwaves that results in a volumetric absorption for heat, Keo at al. demonstrated a detection of corroded steel inside concrete reinforcements [73]. A horn antenna was excited by using a commercial magnetron with 800 W of energy and operating at 2.45 GHz. A specimen of concrete, with an embedded steel bar, was heated with an incident electromagnetic wave for about five minutes. During the radiation, an IR camera recorded the change of heat on the concrete specimen. The recording was processed using a specific algorithm to distinguish the slight difference in temperature. The experiment demonstrated a temperature increase where the steel reinforcement was located. In addition, the results show the ability of MT to detect up to 3.8 cm inside a concrete specimen without causing alteration to the specimen.

An electromagnetic field can be visualized using IR thermography that captures the thermal distribution of the waves on a sensitive-thin film. The incident electromagnetic wave is partially absorbed by an electrical field sensitive film that converts the absorbed electromagnetic power into heat. As a result, a thermal pattern is formed on the sensitive film, and an IR camera then captures that heat distribution as shown in Fig. 1.3. This technique provides a characterization method for the antenna near-field radiation and the propagation mode of the wave guide [62]. Visualization of the electromagnetic wave was started in 1955 by Hasegawa [74] using a sheet of paper that changed color from pink to blue when it absorbed electromagnetic power. This study was followed by further valuable research, the principle of IR imaging of the absorption sheet has not yet utilized. The first study that involves IR thermography was reported by Iizuka and Gregoris [75]. Here, a carbon-rubber sheet is placed on the front of a 10W microwave source with 76.6 GHz frequency. The microwave source illuminates a metal object, hence the image is absorbed by the thin sheet. Metzger [76] obtained the measurements of the fallen electromagnetic field by utilizing an IR camera to capture the equilibrium temperature of the absorption surface. However, since the measurement was obtained in a steady-state regime, the accuracy of the thermal images was 15% when a high power source was used and about 50% in the case of a lower power source. The achieved results are considered as low sensitivity beside the lengthy time period required to obtain the final image (20 minutes). This is

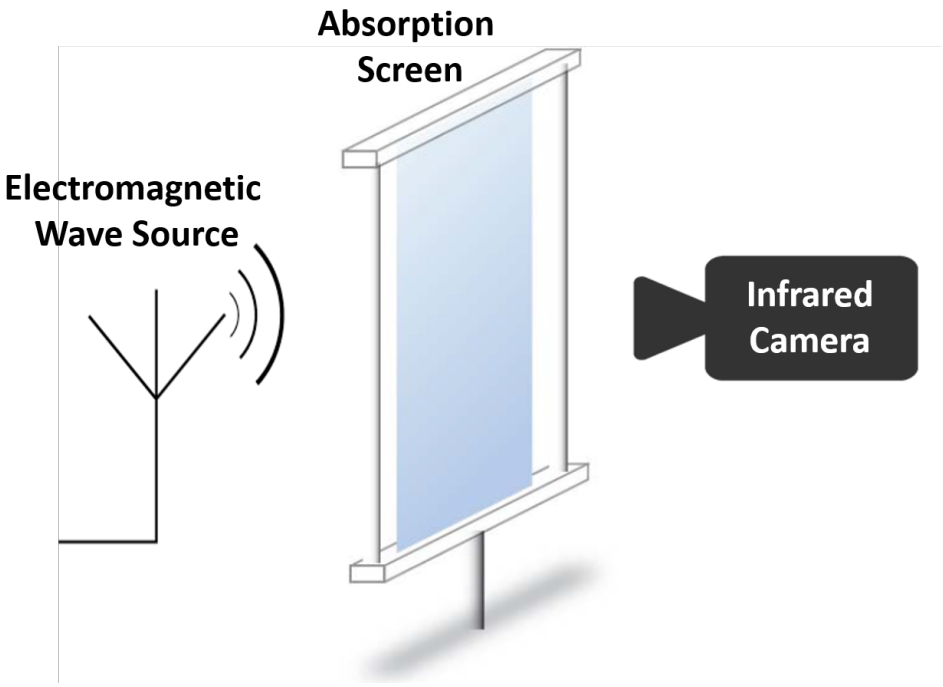

Figure 1.3: The principle of applying thermography for electromagnetic field measurement.

attributed to the waiting time to obtain an image of the equilibrium surface temperature, which takes a long time to reach a steady-state condition, and is affected by convection and radiation of heat transfer [77].

Researchers at the French Aerospace Lab reported a characterization study for the electrical field pattern of a metamaterial resonator [78]. The measurements of the near-field radiation of the metamaterial structure were obtained in a similar way to the previous study by [66], where the thermoemission film was placed close to the structure. A good agreement was achieved between the experiment and the numerical results obtained by the finite-element method. Recently, multiple amplitude ad phase images were captured from a single experiment using frequency modulation [62]. The chirp signal and image processing employed in this study resulted in high resolution thermal images of patch-antenna electromagnetic radiation. Images resulting from numerical simulation (CST) exhibit a high similarity to those obtained by the experiment at low frequency modulation. It is worth mentioning that the simulation results show a square electrical field on the pattern on the absorption screen, hence the heating on the absorption screen (in the experiment)

is a result of the tangential component of the electrical field.

1.4 Metasurface

A metasurface can be defined as a two-dimensional (planar) synthetic material consisting of dielectrics and/or metals, with a surface that contains a periodic pattern of electrically small resonators. Metasurfaces have been widely investigated as a result of the exceptional interaction with electromagnetic waves that introduce new features that are not naturally available in the material [79, 80, 81]. Moreover, compared to metamaterial (the 3-D version of a metasurface), metasurfaces have a smaller physical space, lighter weight, lower losses, and easier fabrication [82, 83]. The resonators (scatters) and the thickness of the metasurface are considered as electrically small compared to the wavelength of operation. The periodicity and the space between the resonators can be engineered to control the reflection, absorption, and transmission to the incident wave.

The critical factor comes from the scalability of the metasurface unit cell, which allows its use within the desired frequency spectrum. Engineering the geometry and the shape of the unit cell affects the surface refractive, hence different functions can be obtained. In addition, the impedance of the unit cell can be manipulated to control the phase of the surface waves [84]. Based on these capabilities, a broad domain of applications was introduced, including microwave radiation absorption [85], antenna capability enhancement [86, 87], energy harvesting [88, 89], superlenses [90, 91], fluid controlling [92],and cloaking [93, 94].

Based on its definition as a 2-D material, a metasurface can be divided into two categories: metascreen and metafilm. A metascreen is composed of separated apertures, arranged in a periodic pattern that have a "fishnet" topology [95]. The metafilm consists of a surface that has an array of separated periodic elements that have "cermet" topology. The electrically small elements can be characterized by their distribution density and the electrical and magnetic polarization [89]. A metafilm can be used as an antenna, where it can be utilized as a radiator or as a receiver in several applications. The versatility of the metafilm encourages the interest of communication field researchers to consider such a structure in communication device development.

1.5 Convolutional Neural Network (CNN)

Over the last decade, machine learning has received intensive improvement towards enhancing its performance and capability. This development is pushed by the breakthrough occurring in the neural network, which contains different techniques and algorithms to raise the ability of computers to recognize a specific pattern (visual, audible, written) among huge data [96]. Several applications have started to evolve machine learning, ranging from speech recognition [97, 98] to biomedical analysis [99, 100] and natural language processing [101]. The popularity of machine learning in the field of computer vision started to develop when neural networks provided an outstanding performance in image analyses compared to other machine learning techniques. This was noted during the ImageNet competition that was held in 2012 and won by Alex Krizhevsky through his neural network architecture "AlexNet" [102].

Machine learning is of high importance in medical imaging as a result of its outstanding capability in image classification, feature recognition, and image analysis. Mingxia et al. [103] employed a deep learning CNN on MRI brain images to recognize Alzheimer's disease, which relate to anatomical landmarks in the brain. Moreover, utilizing an end-to-end learning method, Zhou et al. [104] harnessed a CNN for an automatic abdominal organ localization and segmentation of 3D computed tomography scan (CT) images. Jen et al. [105] achieved a significant performance in applying a CNN to MRI result images of the lumbar spine for segmentation of spine vertebrae and spinal stenosis grading.

Recent MWI studies have involved different machine learning methods to develop a higher detection capability. Utilizing backscatter microwave signals, some studies implemented machine learning on numerical targets to classify and characterize tumors [106, 107]. Rana et al. [108] reported the first clinical data-based study that incorporates MWI and machine learning to differentiate between healthy and malignant breasts. Therefore, involving machine learning in the technique presented in this work is anticipated to enhance the capability of detecting the presence of a cancerous tumor inside the breast. In addition to qualitative results, machine learning may provide some valuable quantitative features of the tumor, such as size, location, and depth inside the breast.

The fundamental of machine learning is based on developing techniques that allow computers to deal with problems by learning from training [96]. This can be achieved by building mathematical models that are used to train the computer to provide a valuable output when supplied by input data. A machine learning model gains "experience" when subjected to training using the training data, during which the algorithm should be optimized to enhance the prediction accuracy of the training data. The main objective is to

train the model to obtain enough expertise in order to provide an accurate decision for the totally new "unseen data". Multiple training and adjusting sessions are required before the model is provided by the unseen data "test set". The model is then evaluated based on the accuracy of the results, namely "the output data", that are related to the supplied test set, namely "the input data".

1.6 Related Theory

1.6.1 Wave propagation in lossy material

When a uniform plane wave with a normal incident hits a lossy dielectric slab as illustrated in Fig. 1.4, the wave will be partially reflected, absorbed, and transmitted. The reflection coefficient at the boundary ($z = -d$) of the interface can be defined as:

$$\Gamma = \frac{\eta_2 - \eta_1}{\eta_2 + \eta_1} \tag{1.1}$$

where η_1 and η_2 are the intrinsic impedance of medium 1 and medium 2, respectively. The total input reflection at $z = -d$ is given by:

$$\Gamma(z = -d) = \frac{\Gamma_{12} + \Gamma_{23} e^{-\alpha_2 d} e^{-j2\beta_2 d}}{1 + \Gamma_{12}\Gamma_{23} e^{-\alpha_2 d} e^{-j2\beta_2 d}} \tag{1.2}$$

where α_2 and β_2 are the attenuation and the phase constants of the incident wave in medium 2, respectively. The transmission coefficient is written as

$$T = \frac{2\eta_2}{\eta_2 + \eta_1} \tag{1.3}$$

η_2 of medium two is the ratio between the incident electrical field E_i and the magnetic field H_i, hence it can be defined as:

$$\eta = \frac{E_i}{H_i} \tag{1.4}$$

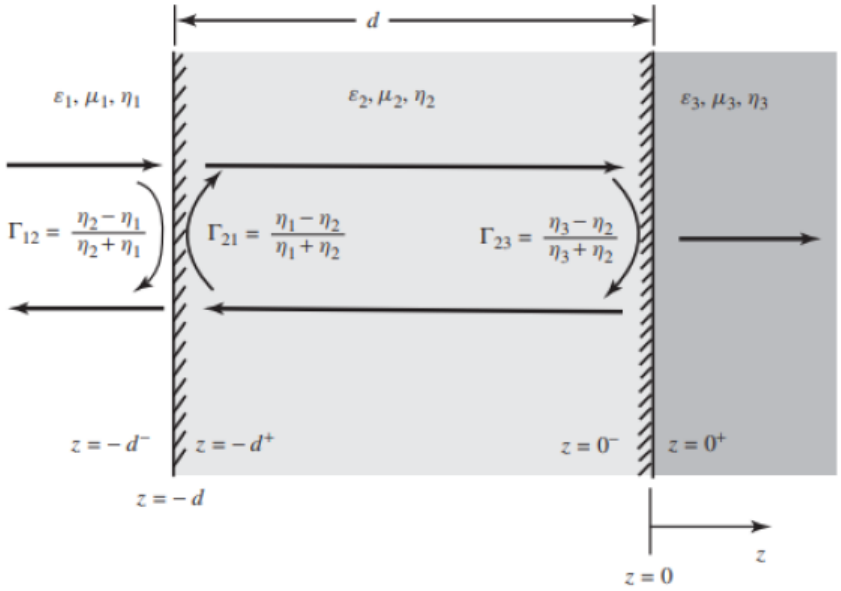

Figure 1.4: Reflection and transmission coefficients for wave propagation in dielectric slab [109]

$$\eta = \frac{E_0}{H_i} e^{-\alpha z} e^{-j(\beta z \omega t)} \tag{1.5}$$

$$\eta = \frac{E_0}{H_i} e^{-\alpha z} e^{-j\beta z} (t = 0) \tag{1.6}$$

where ω is the angular frequency. Similarly, η_1 of the air can be obtained. It can be observed that η_1 and η_2 are a function of the α and β which are related to the corresponding constitutive parameters of the medium (i.e. the permitivity ϵ, the permeability μ, and the conductivity σ), and can be written as:

$$\alpha_2 = \omega \sqrt{\frac{\mu_2 \epsilon_2}{2} \left[\sqrt{1 + \left[\frac{\sigma_2}{\omega \epsilon_2} \right]^2} - 1 \right]} \tag{1.7}$$

$$\beta_2 = \omega \sqrt{\frac{\mu_2 \epsilon_2}{2} \left[\sqrt{1 + \left[\frac{\sigma_2}{\omega \epsilon_2} \right]^2} + 1 \right]} \tag{1.8}$$

1.6.2 Skin Depth

Human body tissue is considered as a lossy material that can actually be classified as an imperfect dielectric or imperfect conductor. Contrary to the lossless medium, the biological tissue conductivity is not equal to zero. In addition, previous studies report that the dielectric properties of body tissue change with changes in frequency. The wave propagation in human tissue will be considered as a propagation in a lossy medium. Starting with the wave equation:

$$\Delta^2 E - \gamma^2 E = 0 \tag{1.9}$$

where

$$\gamma^2 = j\omega\mu \left(\sigma + j\omega\epsilon \right) \tag{1.10}$$

and it can be written as:

$$\gamma = \alpha + j\beta \tag{1.11}$$

where γ is a propagation constant of the medium and σ is a medium conductivity. Since $\alpha \neq 0$ in lossy dielectric, as shown in Eq. 1.7 , the penetration depth of the medium is considered as decreases in the wave amplitude, which is measured in nepers per meter (Np/m) or decibels per meter (Db/m). A reduction of 1 neper equals a decrease to e^{-1} of the main value of the wave, as illustrated in Fig. 1.5 [109], in the case of the following

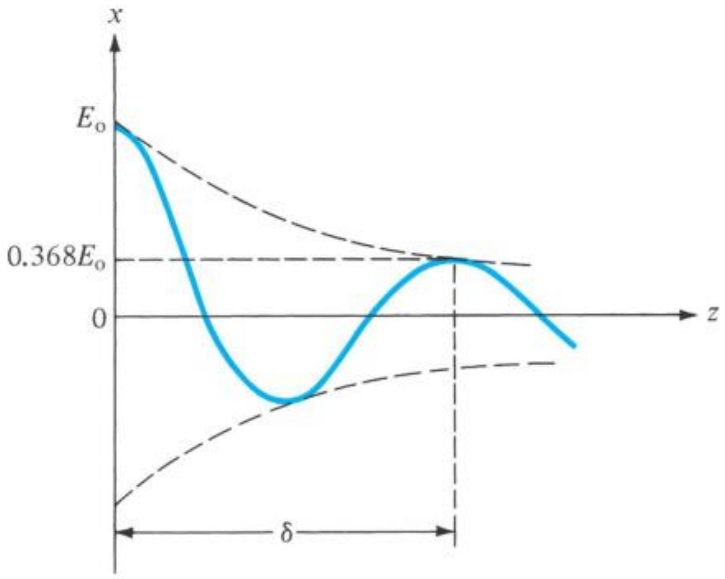

Figure 1.5: Illustration of skin depth [109]

plane wave:

$$E = E_o e^{-\alpha\delta} e^{-j\beta\delta} ax \tag{1.12}$$

where δ is the penetration depth. When the wave starts attenuating inside the medium and decreases by e^{-1}, the wave equation can be modified:

$$E = E_o e^{-1} e^{-j\beta\delta} ax \tag{1.13}$$

Therefore:

$$E_o e^{-\alpha\delta} = E_o e^{-1} \tag{1.14}$$

$$\delta = \frac{1}{\alpha} \tag{1.15}$$

Substitute (3.7) in (3.15):

$$\delta = \frac{1}{\alpha} = \frac{1}{\omega\sqrt{\frac{\mu\epsilon}{2}\left[\sqrt{1+\left[\frac{\sigma}{\omega\epsilon}\right]^2}-1\right]}} \tag{1.16}$$

Based on this theory, it can be concluded that, for each material (lossy dielectric) the transmission coefficient is different since the constitutive parameters of each material (ϵ, μ, and σ) are different. Therefore, the electrical field of the transmitted wave differed depending on the material types. In other words, Fig. 1.6 shows that introducing a material with different electrical properties inside another material (Medium 2), as shown in Fig. 1.6 (b), can affect the propagation of the wave, hence the recorded electrical field of the transmitted wave is different compared to that shown in Fig. 1.6 (a).

This principle can be utilized and harnessed to be beneficial for biomedical imaging applications. Since the dielectric constant and the conductivity of the biological tissue differ based on the water content of the tissue. The presence of a different tissue changes the propagation (reflection, absorption, and transmission) of the wave through the object under test, hence the transmitted electromagnetic power changes.

1.6.3 Absorption on the thin film

The fallen electromagnetic wave on an absorption sheet exhibits all three wave states: reflection, absorption, and transmission. To study these wave behaviors, an equivalent circuit for the system can be illustrated using the transmission line technique, as in Fig. 1.7 and Fig. 1.8, as reported in [62, 110].

The medium (air) through which waves transmit is considered as a transmission line with characteristic impedance Z_0. The impedance of the absorption sheet can be considered as sheet resistance Z_s that is inversely in proportion with the conductivity of the sheet (σ) and the sheet thickness (d), hence [111]:

$$Z_S = \frac{1}{\sigma d} \tag{1.17}$$

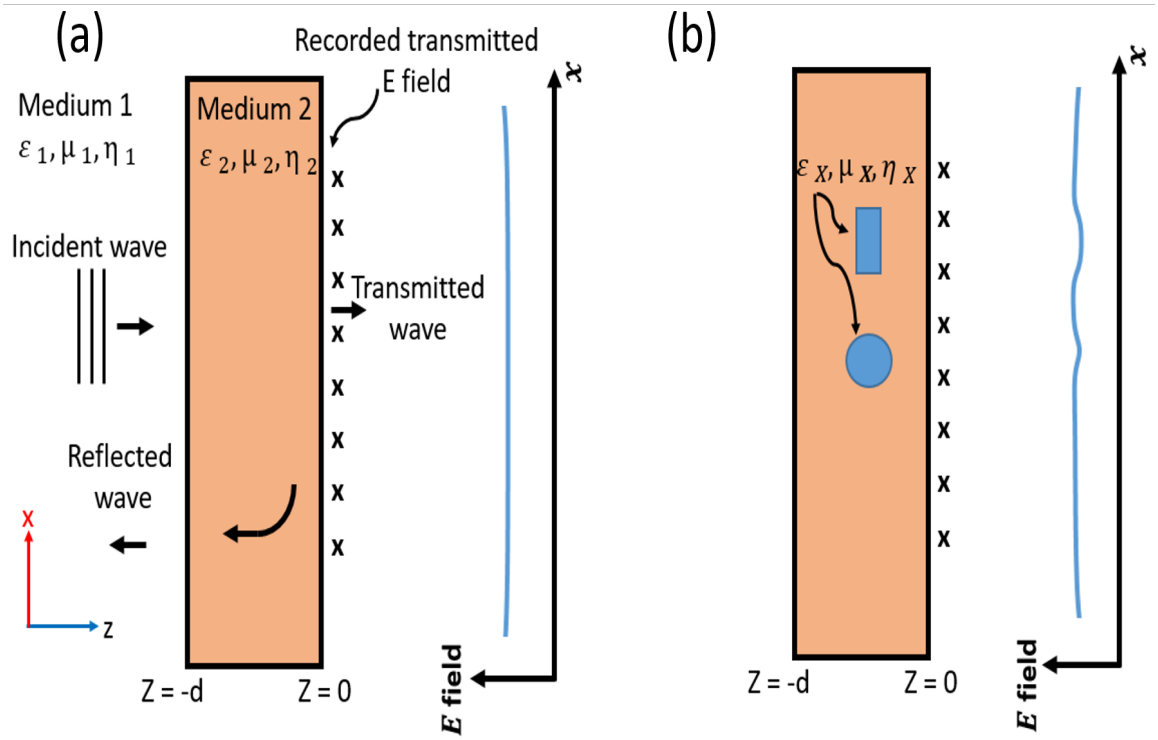

Figure 1.6: A schematic diagram illustrates the wave propagation and transmission through lossy (a) homogeneous medium (Medium 2) and (b) in-homogeneous medium that includes materials with different properties. The curves show the recorded transmission electric field measured at very near field.

This transmission line equivalent circuit is utilized to calculate the reflection, absorption, and transmission through the absorption sheet. The load impedance Z_L of the above circuit can be found as:

$$Z_L = Z_S || Z_0$$

$$Z_L = \frac{Z_S Z_0}{Z_S + Z_0} \tag{1.18}$$

The reflection coefficient Γ is then defined as [62, 110]:

$$\Gamma = \frac{Z_L - Z_0}{Z_L + Z_0} \tag{1.19}$$

by substituting 1.18 in 1.19 :

$$\Gamma = \frac{-Z_0 \sigma d}{2 + Z_0 \sigma d} \tag{1.20}$$

From 1.20, the reflection from the sheet can be optimized by controlling the sheet conductivity and thickness.

Consider:

$$\xi = \frac{Z_0}{2Z_S}$$

Hence:

$$\Gamma^2 = \frac{\xi^2}{(1+\xi)^2} \tag{1.21}$$

The transmission coefficient is defined as:

$$T = \frac{2Z_L}{Z_L + Z_0} \tag{1.22}$$

Using the value of ξ, the transmission coefficient can be written as:

$$T = \frac{1}{1+\xi} \tag{1.23}$$

Hence:

$$T^2 = \frac{1}{(1+\xi)^2} \tag{1.24}$$

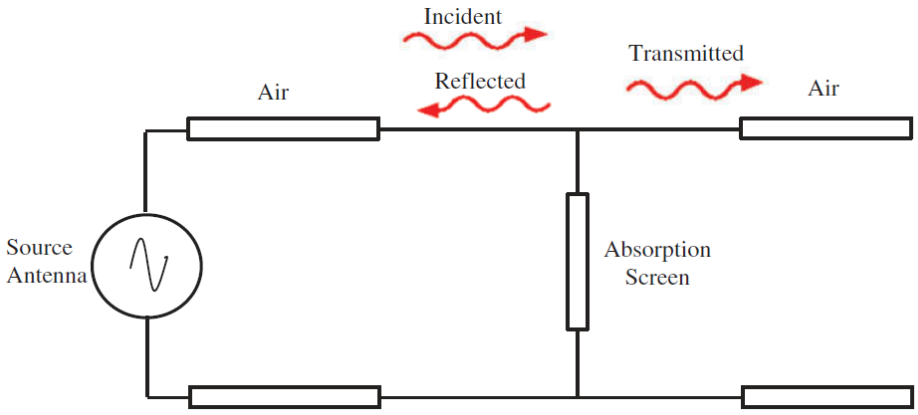

Figure 1.7: Equivalent transmission line circuit of the absorption film [62].

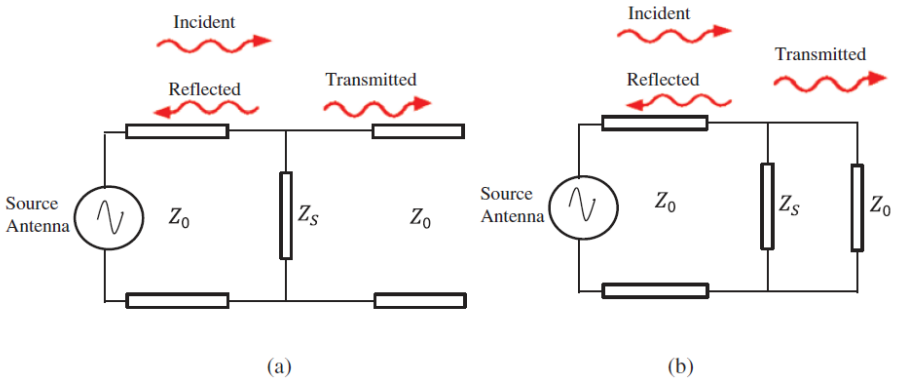

Figure 1.8: Equivalent transmission line circuits where (a) absorption sheet is considered as sheet resistance Zs, and (b) including transmission characteristic impedance Z_0 [62].

After finding the reflection and the transmission coefficient, the absorption coefficient (α) can be calculated. The total incident power on the sheet is the sum of reflected, absorbed, and transmitted power through the sheet, therefore [62]:

$$P_{tot} = P_{ref} + P_{trs} + P_{abs}$$

$$1 = \frac{P_{ref}}{P_{tot}} + \frac{P_{trs}}{P_{tot}} + \frac{P_{abs}}{P_{tot}}$$

$$1 = \Gamma^2 + T^2 + \alpha^2$$
$$\alpha^2 = 1 - \Gamma^2 - T^2$$

$$\alpha^2 = \frac{2\xi}{(1+\xi)^2} \tag{1.25}$$

It can be observed that the maximum value of α is 0.5, happens when $\xi = 1$ [112]. The power fractions of the transmitted, reflected, and absorbed power are shown in Fig. 1.9 as a function of the surface resistance of the absorption sheet.

The power absorbed from the incident electromagnetic wave per square meter in a thin film (sheet) is described by [113]:

$$P_{abs} = \frac{1}{2}\int_0^d \left[(\sigma^{'} + \omega\epsilon^{"})(E^2) + \omega\mu^{"}(H^2)\right] dn \tag{1.26}$$

Here, n is the vector normal to the surface of the thin sheet, $\sigma^{'}$ is the real part of the conductivity of the material, $\epsilon^{"}$ and $\mu^{"}$ are the imaginary part of the complex permittivity and complex permeability of the material, respectively.

The thin film used in this project is a polycarbonate film where the values of $\epsilon^{"}$ and $\mu^{"}$ are much smaller than the value of $\sigma^{'}$, hence the absorbed power is defined as:

$$P_{abs} = \frac{\sigma^{'}}{2}\int_0^d \left[E^2\right] dn \tag{1.27}$$

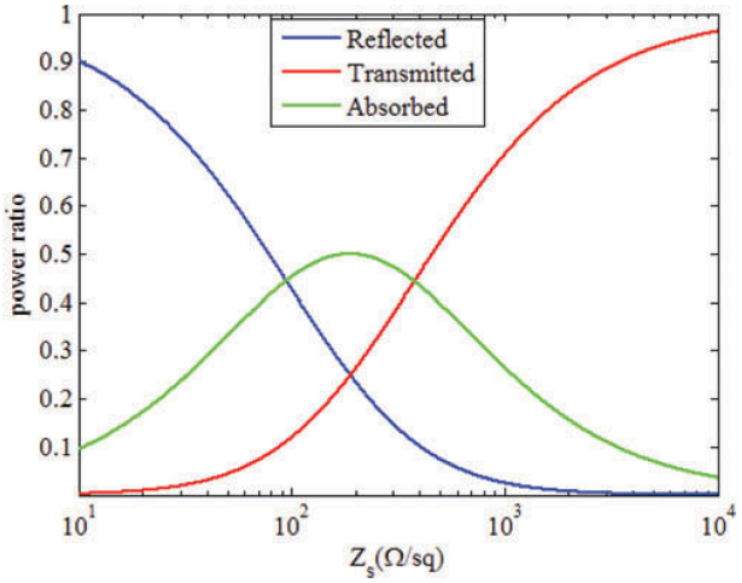

Figure 1.9: Variation of reflected, transmitted, and absorbed powers with sheet surface resistance [62].

Therefore [114]:

$$P_{abs} = \frac{\sigma' dE^2}{2} \tag{1.28}$$

Increasing the sheet temperature due to the electromagnetic power absorption will be discussed in detail in Chapter 2.

1.7 Problem statement

1.7.1 Research Motivation

Although breast cancer causes a high number of deaths worldwide every year, the current imaging techniques are still incapable of precisely detecting a malignant tumor in the early stages. In addition to its harmful ionizing radiation, the x-ray mammography detection rate for cancerous tissue in dense breasts could become as low as 55% [7]. It is worth mentioning that breast density is related to increased probability of developing breast

cancer [115]. Therefore, women at high risk of breast cancer are unable to take advantage of the most common breast screening technique, namely mammography [7]. In contrast, the benefits of the high resolution and accuracy of MRI are still restricted by the high cost that prevents this technique from being a common modality for breast cancer imaging.

In MWI imaging, in addition to fact that the microwave technique is still not clinically available, the mismatching at the air-skin interface results in a significant reflection that affects image quality and accuracy. Additionally, improving the accuracy of MWI requires collecting more signals (information), which can be achieved by reducing the antenna footprint, hence increasing the number of receivers in the system. However, while a smaller antenna size is compatible with a higher frequency that enhances the resolution in general, higher frequencies limit the penetration of the microwave inside the breast. Moreover, increasing the number of antennas causes mutual coupling between adjacent elements, thus reducing the quality of the image [116].

Toward overcoming the MWI challenges and achieving less system complexity, recent studies concentrated on MWD instead of imaging [117, 118]. Recent MWD systems required prior information about the presence of the tumor inside the breast while, in some studies, the experimental part was based on homogeneous breast phantoms [119, 120, 121]. Moreover, in the case of non-identical (asymmetrical) breasts, a slight difference in breast tissue distribution in one of the breasts may affect the total breast permittivity, which leads to different sensing results. Therefore, these aspects reduce the practicality of the MWD system in real life applications.

From this investigative overview, an improvement in the detection and characterization of cancerous tumors is essential in order to decrease the number of deaths caused by breast cancer. Therefore, an alternative screening technique that has the capability of diagnosing early stage tumors, as well as determining location and size, can encourage the further development of breast imaging technology, enabling more lives to be saved. In addition, non-body harmful components and affordable access costs should be considered in designing such a technique.

1.7.2 Research Objectives

The main objective of this study is to develop a microwave detection technique that increases the ability to diagnose a cancerous tumor in dense breasts in the early stages. Utilizing this MWD system, the objectives that can be achieved are as follows:

1. Develop a non-ionizing and non-invasive technique that operates in a microwave regime for breast cancer detection.

2. Improve the accuracy of early stage diagnosis of cancerous tissue in breasts that have dense tissue.

3. Determine the location and size of tumors, and detect tumors that are located deeper inside the breast.

4. Introduce an affordable and comfortable imaging modality for breast cancer detection.

5. Introduce a new microwave technique to overcome the recent challenges that face MWI and build a less complex microwave system.

1.8 Dissertation Outline

The remainder of this dissertation is organized as follows:

Chapter 2 of the thesis proposes a novel breast cancer detection technique that comprises a combination of a microwave source for radiation, an IR system for heat detection and machine learning for imaging classification. The study conducted a numerical, experimental investigation, and involved machine learning to investigate the capability of the proposed modality in detecting tumor presence inside an extremely dense breast and provide quantitative data about the tumor.

Chapter 3 introduces a new concept using a metasurface for breast cancer detection. This concept utilizes a metasurface film as a receiving sheet that captures a transmitted electromagnetic wave through the breast. The theory behind this principle and the design methodology of the metasurface film is discussed in detail. The feasibility of this modality was intensively investigated through the simulation study, the experimental trial and the convolution neural network training.

Chapter 4 presents a flexible breast cancer detection system that is built completely by using a metasurface for radiation (transmitter) and for signal detection (receiver). The chapter explains the design processes, optimization steps, and the material features that are implemented to achieve flexible metasurface films that work at 50 Ω impedance. The comprehensive numerical study determines the potential of this system to detect a small cancerous tumor while defining the existing location and the size.

Chapter 5 summarizes the main contributions, the already accomplished work of the thesis, and the future work that will improve the proposed modalities.

Chapter 2

A Microwave-Thermography Hybrid Technique for Breast Cancer Detection

2.1 Introduction

This chapter presents a hybrid breast cancer detection modality that consists of microwaves as a radiation source, an IR thermography method as a heat-imaging recorder, and supported by a CNN as a machine learning method. This hybrid technique is based on the difference in the transmitted electromagnetic power between healthy and tumorous breasts. The variation in transmitted power results from the variation in electrical properties between healthy and cancerous tissue, which influences the wave propagation inside the breast differently. Under microwave radiation, the power of the transmitted waves leads to a heat distribution pattern on a sensitive screen placed under the breast. This technique utilizes the change in the heat pattern to indicate the presence of abnormality inside the breast. Involving a CNN elevates the proposed technique's detection capability and extracts quantitative data that characterize the tumor's location and size.

2.2 Theory and Methodology

When an electromagnetic field impacts a lossy inhomogeneous medium, part of the wave energy is scattered in all directions and is absorbed by the medium. This phenomenon

of scattering and absorption is entirely dependent on the medium's dielectric properties (i.e., composition). Analytical expressions for the reflected and transmitted fields can be obtained for simple geometries made of infinite homogeneous layered media. However, for media that is finite and complex in terms of geometry and composition, as shown in Fig. 2.1, the scattered field will be equally complex but expected to be uniquely representing the medium through which the propagation takes place. Furthermore, a profile of the transmitted energy (which is essentially a scattered field) taken on a flat surface, which is placed on the opposite side of the source, is expected to provide a unique signature for the medium under test. If the medium composition changes, it is expected that a different signature will result. This is the basic principle behind the method introduced in this work, where the breast is considered as the medium through which the electromagnetic field propagates.

Since the dielectric constant and the conductivity of a tumor (whether benign or cancerous) differ from that of healthy tissue, the presence of a tumor can change the breast signature, which is represented by the profile on the flat surface. This transmitted electrical field can be recorded and compared for both breasts to detect the presence of an anomaly or a tumor inside the breast.

In order to implement this principle for breast cancer screening, the breast under test is placed between the electromagnetic field source and an absorption screen, as illustrated in Fig. 2.2. A horn antenna is used as the source of microwave radiation that is incident on the breast. The absorption sheet absorbs the transmitted electromagnetic wave power, which results in increasing the sheet temperature due to the Joule effect. This temperature rise can be captured using an IR camera that has sufficient resolution to detect minor changes in the temperature profile on the screen.

The relation between the absorption of the transmitted wave power and the increase in the sheet temperature ΔT can be given by [122]:

$$P_{abs} = \Delta T \sqrt{4h^2 + (\rho C d w)^2} \tag{2.1}$$

where h is the heat transfer coefficient between the screen and the environment. The film characteristics are the density ρ, thermal conductivity C, and the thickness d, and w is the angular frequency of the incident electromagnetic field. In addition, the power absorbed by the screen can be linked to the electric field E of the electromagnetic wave by substituting 1.17 in 1.28 as:

$$P_{abs} = \frac{E^2}{2Z_s} \tag{2.2}$$

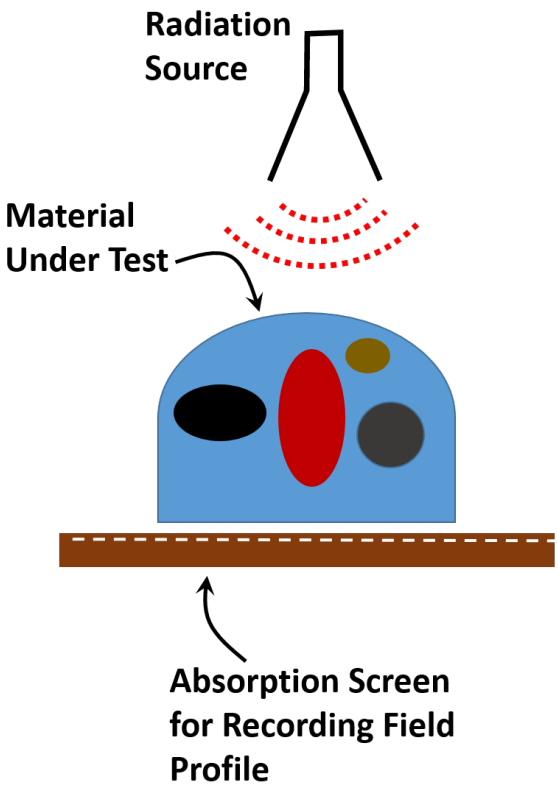

Figure 2.1: Schematic diagram showing the concept of the hybrid technique presented in this work. The object under test OUT is an inhomogeneous object that resembling the human female breast. A thin absorbing screen for recording the field profile is placed immediately underneath the OUT.

where Z_s is the surface impedance of the screen. Accordingly, the change in the film temperature is directly related to the strength of the absorbed electromagnetic field:

$$E = k\sqrt{\Delta T} \tag{2.3}$$

where k is a constant. Therefore, the captured pattern of the temperature on the screen is a function of the square of the absorbed electrical field, which is directly proportional to the power absorbed. Consequently, using this technique, the variation in the internal contents between the two breasts of a single woman can be detected based on the contrast of the heat pattern on the two screens.

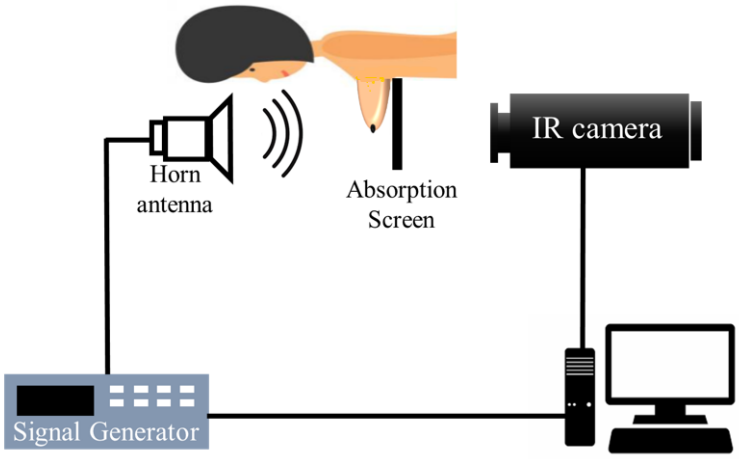

Figure 2.2: Schematic diagram of the microwave thermography hybrid technique (experimental setup).

2.3 Simulation validation

2.3.1 Safety limit

Although a non-ionizing low-power electromagnetic field is considered to have low or no health risks, identifying the safety limit of interaction between the electromagnetic radiation and the human tissue (at the frequency and power of interest) is an essential step in ensuring the suitability for medical applications. The interaction between the biological tissue and the low-power microwave is evaluated by measuring the specific absorption rate (SAR). Zastrow et al. [123] calculated the breast tissue absorption for microwave radiation over multiple frequencies ranging from 1 to 11 GHz. The study stated that, at 2 GHz, a microwave with 1 mW radiation power results in a 9.39 and 9.50 mW/kg peak 1-g SAR in heterogeneous and extremely dense breast tissue, respectively. The relation can be described linearly, thus the achieved results can be scaled by a certain factor to meet the desired microwave power and frequency. For illustration, to evaluate the SAR for breast tissue that results from an electromagnetic wave with 50 mW of radiation power at 2 GHz, the reported results are scaled by 50. Consequently, the peak 1-g SAR is 475 mW/kg for an extremely dense breast. Adopting this approach, the targeted frequency and power of the electromagnetic radiation in this proposed technique is maintained in the range of the exposure limit that is suggested by IEEE, which is 2 W/kg, and also within the safe exposure zone that stated by the International Commission on NonIonizing Radiation

Protection (50 W/m^2 for the occupational limits). [124, 125].

2.3.2 Designing the breast models

Designing a breast model for a simulation study requires considerable knowledge of breast tissue contents and densities. A breast is composed of a mixture of fibroglandular and fatty tissue while the density is defined by the percentage of fibroglandular tissue in the breast [126]. The American College of Radiology classifies the breast into four categories based on the internal tissue density: Category A, almost entirely fatty (less than 25% fibroglandular tissue); Category B, fibroglandular scattered areas (25% to 50% fibroglandular tissue); Category C, heterogeneously dense (50% to 75% fibroglandular tissue); and Category D, extremely dense (more than 75%). The first two classes are considered as non-dense, while the remaining two are considered to be dense breasts. It is worth mentioning that approximately 50% of women have dense breasts, and that breast density is related to a higher risk of developing breast cancer [127]. Unfortunately, X-ray mammography faces challenges when screening heterogeneously and extremely dense breasts since dense tissue and a cancerous tumor have the same appearance on a mammogram. Therefore, women at high risk of breast cancer are unable to take advantage of the most common breast screening technique [128]. Thus, our study will focus on the performance of the new microwave thermography hybrid technique in detecting early-stage cancerous tumors in extremely dense breasts.

In this study, the breasts are modeled by building different types of biological breast tissue (skin, fat, and fibroglandular tissue) while defining the dispersive electrical properties for each tissue. Dense breast categories were modeled utilizing human body tissue in full wave numerical simulation software (CST Microwave Studio) [129], taking into account the differences in breast tissue contents and layers to represent a realistic biological breast. The breast models were designed as hemispherical shapes, with a 50 mm radius, and were composed of stacked layers of 2 and 65 mm thickness for the skin and the internal content, respectively, as shown in Fig. 2.3.2 (a). The breast model tissue was assigned (by CST) realistic dielectric properties over a frequency of interest based on the database of an Internet resource for the calculation of the dielectric properties of body tissue (IFAC-CNR) [130], which is based on the dielectric properties of body tissues developed by Gabriel et al. [131, 132, 133, 134]. It is worth mentioning that these properties change with frequency without any interference from the user. The relative permittivity and electrical conductivity of the internal tissue at 2.5 GHz are assigned (as reported in IFAC-CNR) to be 57 and 2 S/m, respectively, for the fibroglandular tissue, while breast fat is given electrical property values of 5.1 and 0.14 S/m. For a low contrast scenario, malignant

breast tissue contrasts with normal tissue (fibroglandular) of approximately 2:1 in electric conductivity and dielectric constant, as documented in previous studies [135], which is a much lower level than that reported in [136]. Therefore, the tumor dielectric properties are suggested to be 100 and 10 S/m for the relative permittivity and conductivity, respectively. It worth mentioning that several studies reported that cancerous breast tissue have two or more times greater electrical properties than that of the host tissue [15, 16, 137, 138]. Although the assigned relative permittivity of the tumor is relatively high, it has a double value (2:1) of the relative permittivity of the fibroglandular tissue at 2.5 GHz. Similar to the process used in mammography, the breast surface is flattened to achieve the maximum possible uniform microwave illumination.

2.3.3 Tumor detection

The breast cancer detection modality introduced in this study depends on two fundamentals: i) Female breasts are considered to have symmetrical shape and content; and ii) a tumor is extremely unlikely to develop in both breasts simultaneously [139, 140]. Here, the detection mechanism is conducted by employing the same microwave radiation source for both breasts. The captured heat expressions or power signature on the absorption screen are then studied for the final confirmation of the presence of any anomaly between the breasts, which will highly likely imply the presence of a tumor in one of the breasts. Since relying only on human diagnosis can result in human-based errors in determining a sufficient difference between the two breasts' signatures, this study will employ artificial intelligence to significantly enhance the detection reliability.

The envisioned experimental setup is shown in Fig. 2.2. In the numerical simulation, the horn antenna is replaced by a plane wave and a polycarbonate sheet is used as an absorption screen, as illustrated in Fig. 2.3.2(a). The first step involves a simulation run to detect a tumor inside heterogeneously and extremely dense breasts. Thus, two similar breast models are designed for each class (i.e., heterogeneously and extremely dense breasts). A 5 mm radius tumor that has a dielectric constant higher than the fibroglandular tissue is embedded inside one of each breast class models, as shown in Fig. 2.3.2(a), (b), (e), and (f).

A plane wave of electric field intensity of 1 V/m and a frequency of 2.5 GHz was used to illuminate the breast. The electrical field pattern on the absorption screen is shown in Fig. 2.3.2(c) and (j) and Fig. 2.3.2(d) and (h) for breasts with and without a tumor, respectively. Although the tumor radius is 5 mm and is located at a depth of about 15 mm from the screen, it has a significant impact on the final transmitted wave. The

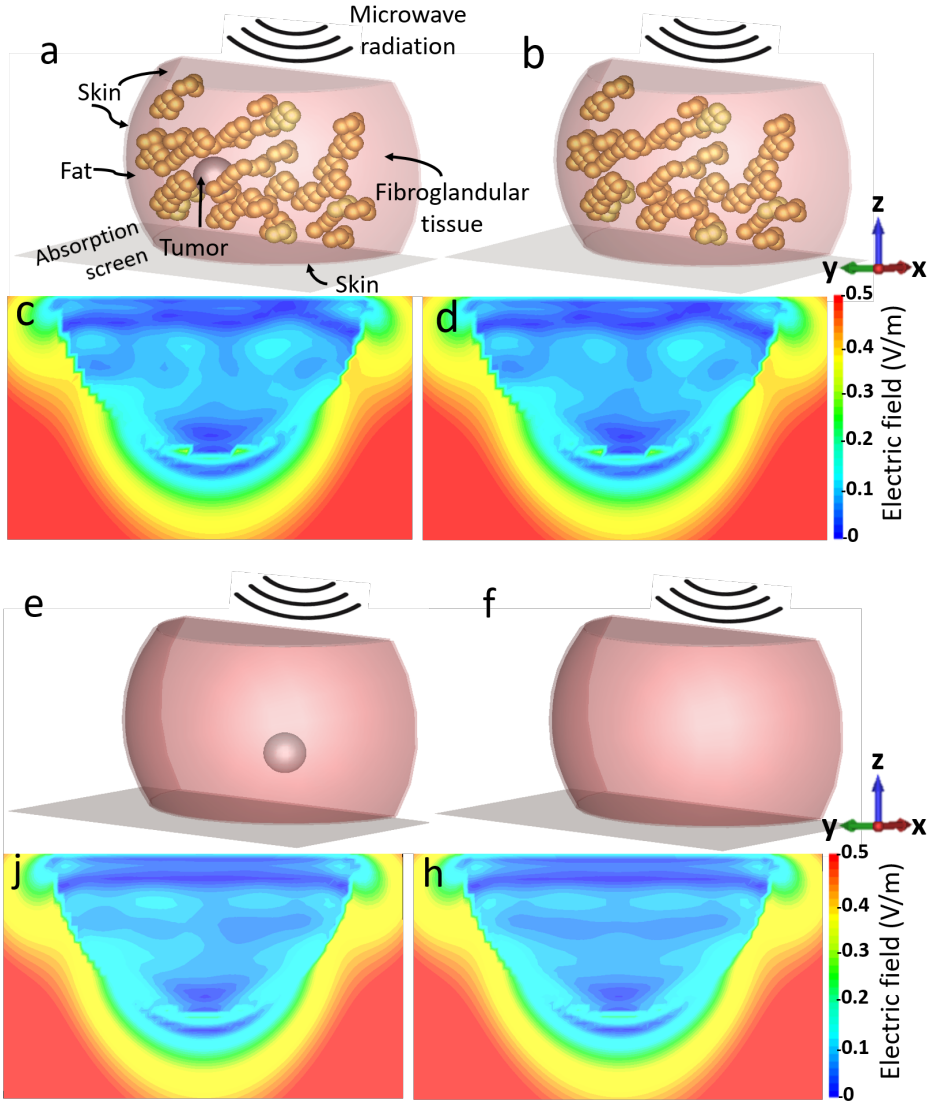

Figure 2.3: Heterogeneously dense breast models (a) with a tumor and (b) without a tumor. The electric field pattern on the absorption screen for heterogeneously dense breasts (c) with a tumor and (d) without a tumor. Extremely dense breast models (e) with a tumor and (f) without a tumor. The electric field pattern on the absorption screen for extremely dense breasts (j) with a tumor and (h) without a tumor.

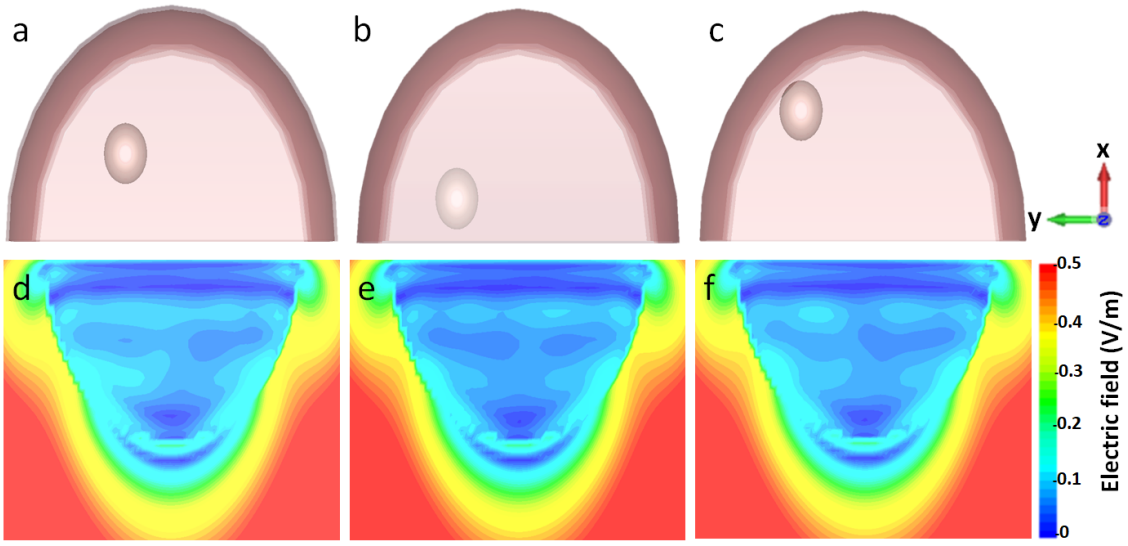

Figure 2.4: The change in the electric field pattern on the absorption screen according to the position of the tumor inside the breast. Tumor located at (a) x=0, y=10, z=15, (b) x=-10, y=15, z=15, and (c) x=10, y=15, z=15, and their electric field pattern on the absorption screen at (d), (e), and (f), respectively (all tumors are the same size).

pattern of the electric field on the screen results from the absorption of the transmitted electromagnetic wave power that is a function of the electric field, as defined in Eq. (3). Therefore, the pattern on the screen is proportional to the electric field that is tangential to the screen.

In order to evaluate the capability of the hybrid technique to differentiate between several tumor locations inside the breast, the tumor position was changed in two dimensions (x and y) inside identical breast models, as shown in Fig. 2.4 (a)-(c). The tumors were kept at the same distance from the screen (at z= 15 mm), where the z-axis is normal to the screen, as shown in Fig. 2.4, and the tumor sizes are the same (5 mm radii), in order to achieve equal comparison for the tumor location. As a result, the location of a tumor affects the propagation of the wave through the breasts, thus a unique signature appears on the screen for each tumor location, as shown in Fig. 2.4 (d)-(f). Next, the tumor depth (distance from the screen) inside the breast was varied, as seen in Fig. 2.5 (a)-(c). The impact of the tumor depth on the transmitted electrical field footprint is shown in Fig. 2.5 (d)-(f). A slight change of approximately 5 mm in the tumor depth can significantly affect the field distribution on the screen. This is noticeable when comparing Fig. 2.5 (d)-(f).

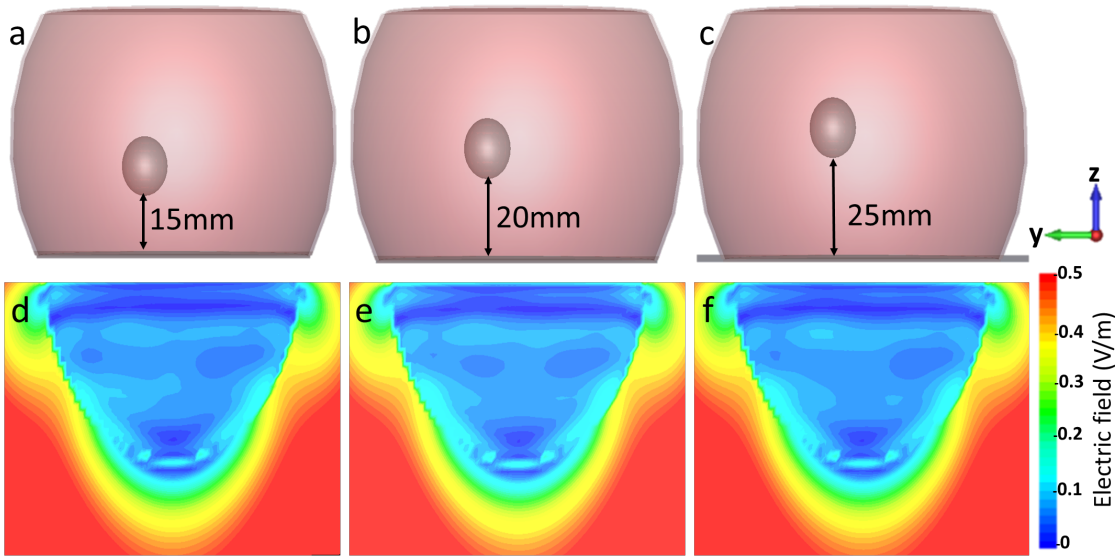

Figure 2.5: The effect of tumor depth (distance from the screen) on the electric field distribution on the screen.

Various artificial spherical tumors, with radii of 3 mm, 4 mm, and 5 mm, were implanted inside the breast models, resulting in different field distributions on the screen. Fig. 2.6 clearly shows the difference between the resulting images. At a depth of 20 mm inside the breast, 5 mm and 4 mm radii tumors were easily detected, as shown in Fig. 2.6 (c) and (d) compared to the reference Fig. 2.6 (a), whereas a 3 mm radius tumor produced a slightly noticeable expression on the screen as shown in Fig. 2.6 (b). The smaller and deeper the tumor location inside the breast, the more challenging it is to detect. However, this hybrid modality can be implemented vertically (with the radiation source on the top of the breast while the screen is placed underneath the breast) and/or horizontally (the radiation source on the left side of the breast and the screen on the right side), while switching the position of the radiation source and the IR camera.

2.4 Machine Learning

Since there is a variation in breast tissue densities, the interpretation of breast images is always subject to the skills of radiologists or, in general, the skills of the observer. As an example, the judgment rate of radiologists in interpreting mammograms has up to a 75% interobserver variation [141], hence about 25% of breast cancer cases are mis-detected

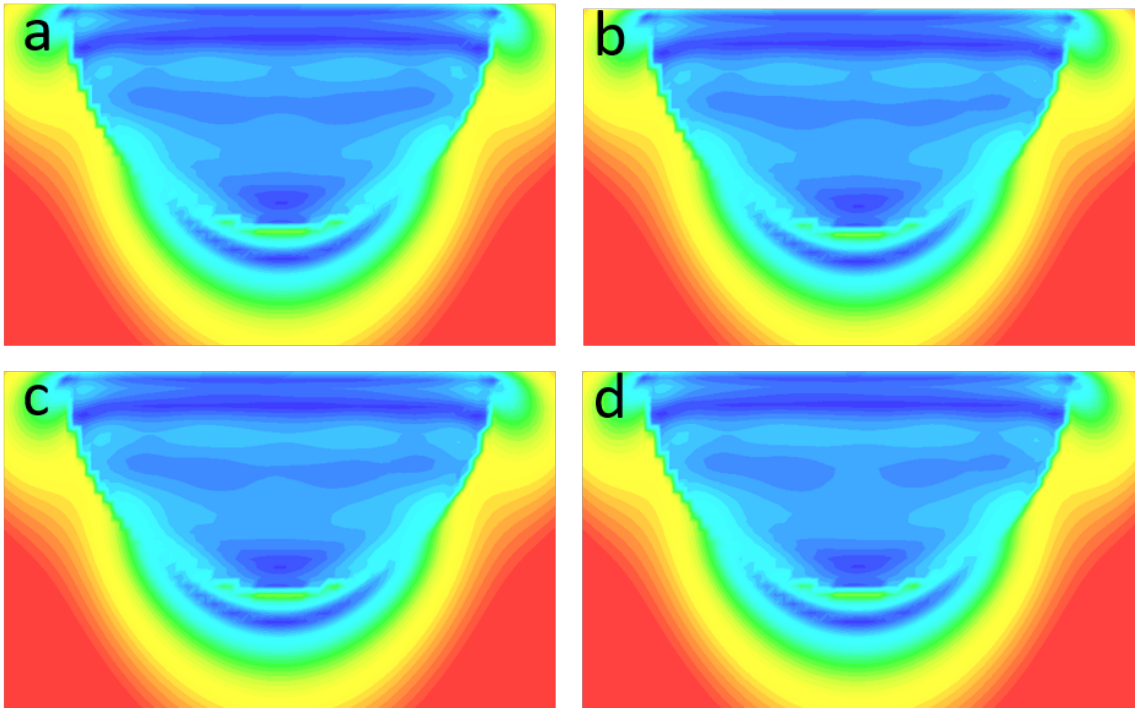

Figure 2.6: The electric field signature of the breast (a) without tumor (reference), (b) with a 3 mm radius tumor, (c) with a 4 mm radius tumor, and (d) with a 5 mm radius tumor.

or declared as a false negative. Computer-aided detection has been employed to improve human-based errors in order to reduce false negative and false positive misinterpretation. Although in the present study an image represents the absorbed/transmitted electric field rather than that of the internal breast tissue, utilizing artificial intelligence, namely machine learning, may significantly enhance the interpretation accuracy of the recorded results.

Machine learning is of high importance in medical imaging as a result of its outstanding capability in image classification [103], feature recognition, and image analysis. [104, 105]. Recent MWI studies have involved different machine learning methods to develop a higher detection capability. Utilizing backscatter microwave signals, some studies implemented machine learning on numerical targets to classify and characterize tumors [106, 107]. Rana et al. [108] reported the first clinical data-based study that incorporates MWI and machine learning to differentiate between healthy and malignant breasts. Therefore, involving machine learning in the technique presented in this work is anticipated to enhance the ca-

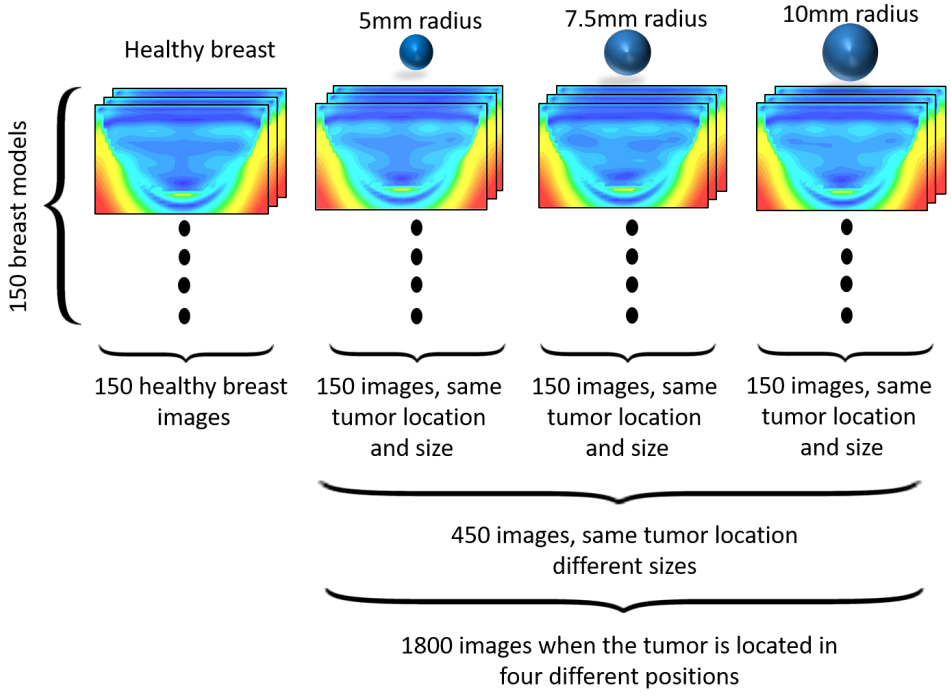

Figure 2.7: Schematic diagram for generating a dataset for CNN where 150 images of healthy breasts and 150 images of non-healthy breasts were generated from 150 different breast models. Varying the tumor size (three sizes) for the same location resulted in 450 images, and changing the tumor location (four locations) increased the number of images to 1800.

pability of detecting the presence of a cancerous tumor inside the breast. In addition to qualitative results, machine learning may provide some valuable quantitative features of the tumor, such as size, location, and depth inside the breast.

In the proposed modality, distinguishing between healthy and unhealthy breasts by comparing the electric field patterns is not difficult to accomplish using the naked eye. The challenge occurs when the breasts are symmetrical but not identical, which can occur when there is a slight difference in the internal breast contents [142]. Consequently, in addition to achieving improved detection performance, the main purpose of involving machine learning is to enhance the detection capability in two aspects that are usually not covered by other breast cancer detection techniques: i) Detecting the presence of a tumor when the two breasts are asymmetric; and ii) Characterizing the tumor features (quantitative data) in terms of size and location. I emphasize that asymmetry may not only be caused by the

internal composition of the breast, but may also be caused by asymmetric compression of the breasts during testing/examination.

2.4.1 CNN architecture

CNN architecture in this work comprises three convolution modules and a fully connected layer, as illustrated in Fig. 2.8. The convolution module contains three main layers (convolution layer, ReLU layer, and pooling layer) and two secondary layers (batch normalization layer and dropout layer). The first convolution module starts with a convolution layer that has a 3x3 filter size and contains 32 filters to extract the features from the input data (image). This is followed by a rectified linear unit (ReLU) layer, which is a mathematical activation function that provides nonlinearity to the system. The batch normalization layer is subsequently applied, with batch size = 32 to manage the data size that flows through the system. The extracted data (features) is then passed to the pooling layer with a pool size of 2x2 to reduce the extracted feature map's dimensions while maintaining the essential features, hence significantly minimizing the processing time. The last layer in the convolution module is the dropout layer that is used to enhance accuracy by reducing overfitting.

The sequence of layer order is repeated in the second and third convolution modules with slight changes. In the second module, the convolution layer has 64 filters instead of 32. Moreover, the first three layers (convolution, ReLU, and batch normalization layers) are repeated twice before the pooling layer is applied. The third convolution module has similar changes to the second module, but the filter numbers are increased to 128 filters, and the first three layers are repeated three times. The CNN architecture ends with a fully connected layer that has a Softmax activation function to execute the classification, depending on the obtained features in the convolution modules.

2.4.2 Dataset acquisition and results

150 dense breast models composed of different tissue types were designed and tested using CST in order to generate the required dataset (electric field images) for machine learning. The designed breasts have internal contents of 75-85% fibroglandular tissue and 15-25% breast fat tissue. In order to achieve complete asymmetry among the breast models, a different unique internal structure (fat and fibroglandular tissue) for each breast was designed. The first set of numerical simulations of the designed breasts was conducted without introducing a tumor inside the breast tissue in order to obtain 150 electric field

patterns of similar but not identical healthy breasts. A tumor was subsequently implanted within each breast tissue (as a second dataset), with a specified location and size, as an attempt towards providing an image dataset of the malignant breasts. The tumor was positioned in four locations (-5, 10, 20), (10, 10, 25), (-15, 5, 10), (25, 0, 0), in x, y, and z, respectively. Additionally, for each tumor location inside the breast models, the size of the tumor was varied to have three different sizes with radii of 5, 7.5 and 10 mm. As a result of changing the tumor location and size, the resultant dataset of unhealthy breasts contained 150 images for each tumor location with a specified size and 450 images for each tumor location, regardless of the tumor size. The total number increased to 1800 images when the tumor location varied between four different locations (150 x three sizes x four locations = 1800 images), as illustrated in Fig. 2.7 .

To first train the CNN to distinguish between healthy and tumorous cases, and recognize the absence of a tumor (in the context that breasts have up to 25% internal-tissue variation), 150 images of healthy breasts were grouped as an individual set and labeled as "healthy breast" for comparison with another 150 images of tumorous breasts that were labeled as the "unhealthy breast" set. Secondly, extracting tumor quantitative information from tumorous-breast images requires arranging the dataset in such a way that trains the CNN classifier in order to determine the tumor location and size. Therefore, four tumorous breast-image groups that contained 1800 images (450 images for each set) were labeled, based on the tumor location, as "Location 1", "Location 2", "Location 3", and "Location 4" and assigned to be the dataset to train the CNN for determining the tumor 3D location inside the breast. Similarly, the same 1800 images were regrouped to form 12 sets (150 images for each set) that represent the tumor size and location, then allocated to train the system to simultaneously specify the tumor location and size. It is worth mentioning that each image resulted from a different internal breast tissue in an attempt to increase the challenge level of detection capability despite the asymmetry of the breasts. Moreover, since the tumor locations (in breast models) were significantly varied over the breast volume, four tumor locations were considered sufficient to show the capability and to prove the feasibility of the proposed modality.

The datasets uploaded as the CNN input for processing through multiple stages started with data preprocessing, classification and training, and ended with testing. Fig. 2.8 illustrates the CNN system structure, including the input arrangement of the database and the output classification for each input set. In order to identify the optimal way to enhance the system accuracy, the datasets were randomly divided into training and evaluation (testing) of the images using different percentages: i) 75% training and 25% testing images; ii) 80% training and 20% testing images; and iii) 90% training and 10% testing images. The system utilizes the training images to determine the relation between the input and

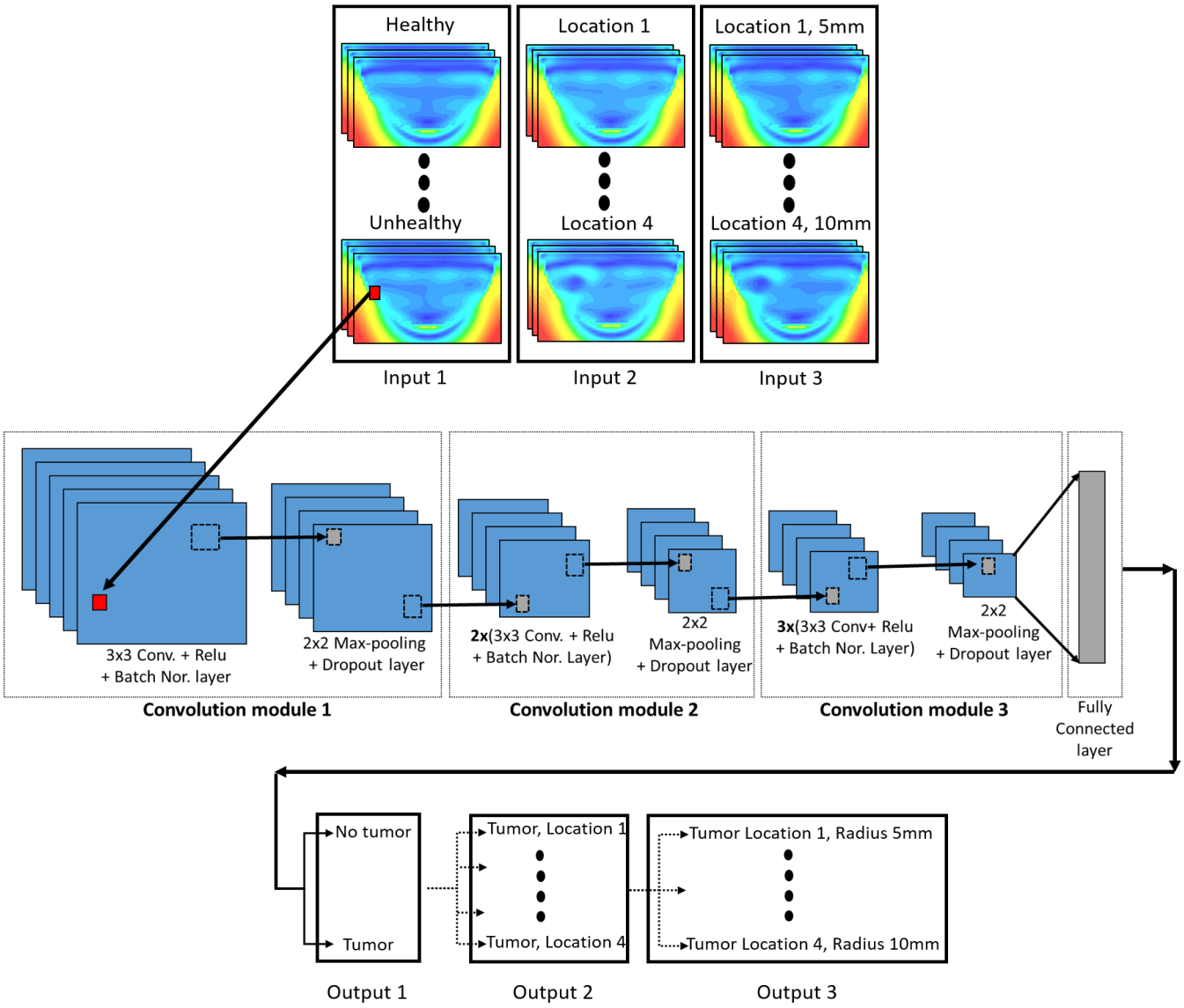

Figure 2.8: An illustration of the machine learning system for breast cancer detection and characterization. The dataset input stages of the system shown on the right are: Input 1, dedicated for detecting tumor presence; Input 2, dedicated for tumor location detection; and Input 3, dedicated for tumor location and size detection. The middle of the figure represents the CNN architecture. Every dotted square represents a single convolution module that includes two blocks. The first block contains a convolution layer, ReLU layer and a batch normalization layer. The second block comprises a max-pooling and a dropout layer. On the left of the figure is the expected classification for each input stage.

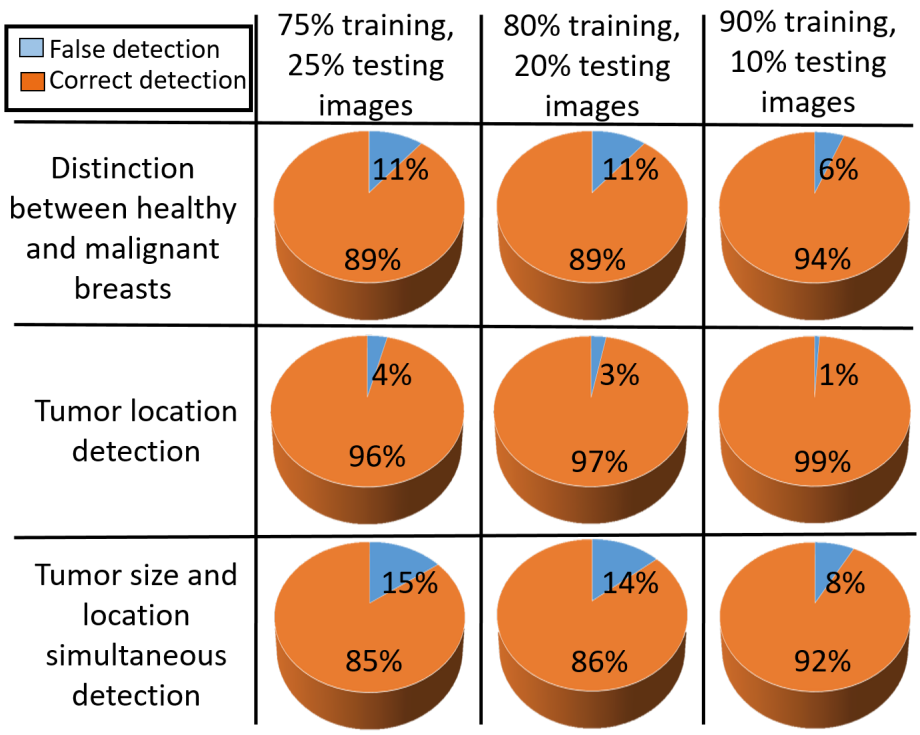

Figure 2.9: CNN results for the three splittings of the training and test images.

the output, while the testing images assist in evaluating the system classification accuracy. The best results were achieved when the dataset was split into 90% and 10% for training and testing, respectively. Although the dataset is relatively small, the performance findings show that it is sufficient to train the system and accomplish significant accuracy in breast cancer detection. In differentiating between healthy and malignant types among asymmetric breasts, the system demonstrated an accuracy of approximately 94% in deciding which breast has cancerous tissue and which has healthy tissue, despite the difference of breast tissue composition even in the same breast class (Fig. 2.9). In addition, the tumor location (regardless of size) was obtained with a detection accuracy of approximately 99%, whereas the simultaneous detection of the tumor location and size shows 92% accuracy, as seen in Fig. 2.9. It should be emphasized that the detection accuracy can be significantly improved by increasing the dataset for each class and improving the CNN algorithm, which will be developed in a separate future study.

2.5 Experimental Validation

2.5.1 Lock-in thermography

The lock-in thermography (LIT) technique was used here to detect the heat pattern on an absorption screen [143]. LIT is a non-destructive detection technique that can be implemented to detect material and electronic device defects [144, 145, 146]. The technique is based on periodically illuminating the object under investigation by a modulated microwave signal. The high frequency microwave signal that is generated by the signal generator is modulated by a low frequency signal. This low frequency signal is synchronized to an infrared camera using a computer as a reference signal for post processing. A series of LIT images (movie) are then captured by an infrared camera to reconstruct the thermal wave periodicity and compare it with the amplitude and phase of the reference signal (the modulating low frequency signal). The recorded images (video), which are taken at a certain frame rate, are then processed using a lock-in correlation method to extract the amplitude and the phase images of each pixel temperature on the absorption screen, as shown in Fig. 2.10. The lock-in technique is able to eliminate the background noise from the thermal pattern on the screen, hence a very minor change of the screen pixel temperature, down to few milli-Kelvin, can be detected [147].

The processing of the lock-in correlation method can be mathematically explained as a multiplication of the recorded thermal signal $F(t)$ by a correlation function $K(t)$, which results in an output signal S after averaging over a specific time [148]:

$$\begin{aligned} S &= \frac{1}{t_{\text{int}}} \int_0^{t_{\text{int}}} F(t)K(t)dt \\ K(t) &= \begin{cases} +1 first\ half\ period \\ -1 second\ half\ period \end{cases} \end{aligned} \tag{2.4}$$

Utilizing the digital lock-in correlation, the measured signal $F(t)$ is digitized as a series of thermal images F_k. Similarly, the correlation factor $K(t)$ is changed to a set of numbers, K_k. Therefore, the digital lock-in correlation technique averages the recorded values and the weighting factors over the total lock-in periods (N) and the number of samples in each period (n). These can be written as:

$$S = \frac{1}{nN} \sum_{i=1}^{N} \sum_{j=1}^{n} K_j F_{i,j} \tag{2.5}$$

where the weighting factor K_j involves two-channel correlations utilizing two functions that approximate the sine and cosine components. Channel one calculates the in-phase signal related to the sine function (the reference signal), which is the signal that is used to modulate the signal generator output, whereas Channel two calculates the in-phase signal related to the cosine function.

$$K_j^0 = 2\sin\left(\frac{2\pi(j-1)}{n}\right) \tag{2.6}$$

$$K_j^{-90^\circ} = -2\cos\left(\frac{2\pi(j-1)}{n}\right) \tag{2.7}$$

Substituting these equations into Eq. (2.5) results in:

$$S^{0^\circ} = \frac{1}{nN}\sum_{i=1}^{N}\sum_{j=1}^{n} F_{i,j}\cdot K_j^{0^\circ} \tag{2.8}$$

$$S^{-90^\circ} = \frac{1}{nN}\sum_{i=1}^{N}\sum_{j=1}^{n} F_{i,j}\cdot K_j^{-90^\circ} \tag{2.9}$$

S^{0° is the thermal wave components of the sine function, where S^{-90° is the phase shifted (by -90^o) regarding S^{0°. Consequently, the thermal signal's amplitude A and phase ϕ can be retrieved by the following equations:

$$A = \sqrt{(S^0)^2 + (S^{-90^\circ})^2} \tag{2.10}$$

$$\Phi = \arctan\left(\frac{S^{-90^\circ}}{S^{0^\circ}}\right) \tag{2.11}$$

2.5.2 Breast phantom fabrication

A realistic breast phantom (i.e., a phantom with similar dielectric properties of breast tissue at the frequency of operation) is required to overcome the simplicity in the existing breast phantoms that were used in the recent experimental validation studies for breast cancer detection [149]. Therefore, in an effort to mimic real breast tissue, I fabricated a

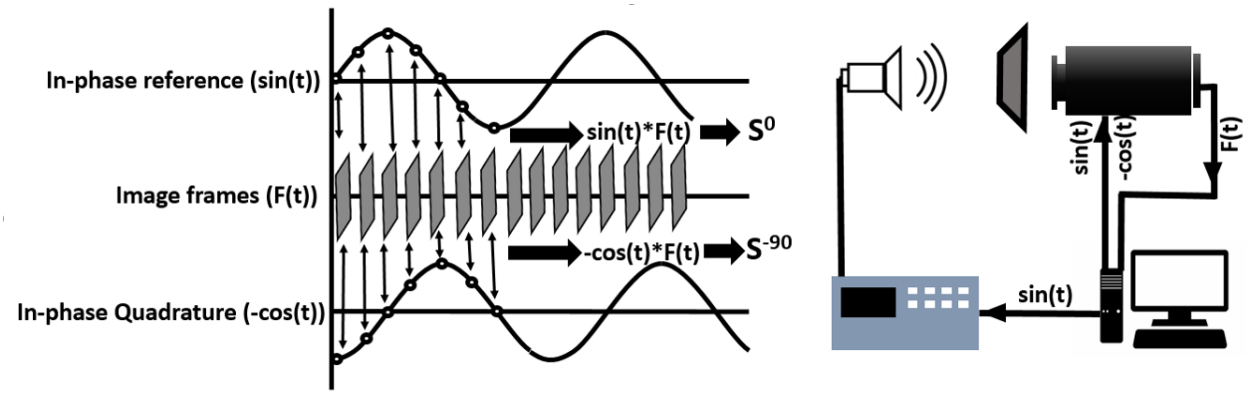

Figure 2.10: Schematic of the lock-in thermography system principle. The left part of the figure shows the process of the lock-in correlation system (sin and -cos) and the frame rate period of the IR camera. The right side of the figure describes the signals' flow of the system on the experiment setup.

breast phantom based on the oil-in-gelatin method that can approximate biological tissue's electrical properties, as described in [150]. The phantom is composed of an oil solution (50% safflower oil and 50% kerosene) and aqueous calfskin gelatin mixed with specific percentages and processed to produce a tissue-mimicking phantom. By varying the oil solution percentage (volume percent) in the mixture, the electrical properties of the phantom are varied, which allows for customizing of the targeted breast tissue, thereby constructing the breast category of interest. Utilizing this approach to build breast phantoms for the experiments, the electrical properties of real breast tissue can be achieved over a frequency spectrum from 0.5 to 20 GHz.

Accordingly, in order to build dense phantoms to conduct the experiments, 10% of the oil solution is introduced into the gelatin solution to simulate the fibroglandular tissue, hence an extremely dense breast phantom is achieved. Similar breast phantoms were prepared to represent normal and malignant breasts by implanting spherical glass marbles in some phantoms to simulate the presence of a tumor, as shown in Fig. 2.11 (e). Moreover, the size and location of the tumors were varied in each phantom in order to provide a variety of phantoms for more efficient experimental validation. The suspension of the tumor in a specific location inside the phantom was conducted by using an absorbable chromic catgut suture to hold the tumor to the container lid until the solidification of the mixture. The chromic catgut suture is partially absorbed in the phantom to minimize the effect of its presence without losing the advantage of positioning the tumor, as seen in Fig. 2.11 (e). I emphasize that the glass marble does not mimic real tumor properties since the

tumor has a higher permittivity and conductivity. However, the purpose is to introduce an object with different electrical properties compared to the breast tissue. The presence of a different material (even with lower dielectric properties) can impact the propagation of the transmitted wave that reaches the sensitive screen.

2.5.3 Experiment setup and results

The experimental setup involved building a microwave thermography hybrid system, as illustrated in Fig. 2.2. The microwave signal was generated by an RF signal generator with a frequency of 700 MHz and -12 dBm power. This signal was modulated by an 0.1 Hz signal, then amplified by a power amplifier and fed to a horn antenna with an input power of about 20 dBm to maintain the safety aspects previously mentioned. The horn antenna, placed at a 2.5 cm standoff distance from the breast phantom, illuminated the breast phantoms that are backed by a sensitive polycarbonated thin film (0.7 μm thickness and 500 Ω/sq surface resistance). The power of the transmitted electromagnetic wave that falls on the sensitive screen was partially absorbed and generated Joule heating [151], as explained in above in 2.2. The temperature change on the screen was then recorded in a movie by an infrared camera, then visualized using the LIT technique. It should be noted that, during the experiment, the microwave signal source (the signal generator) and the temperature recorder (the IR camera) were synchronized by the computer using a low frequency (0.1 Hz) modulating signal. The low frequency signal was considered to be a reference to the recorded film temperature rise signal.

In order to conduct the experiment horizontally (the horn antenna from the left side of the phantom and the IR camera from the right side) to allow easier phantom radiation and IR recording, the breast phantom was placed on a holding stand properly positioned in front of the horn antenna while being backed by the sensitive film, as shown in Fig. 2.11 (a)-(c). Moreover, the experiment was conducted inside an anechoic chamber to prevent any interaction with the surrounding area that could affect the electric field distribution on the screen, and to prevent external radiation sources from affecting the measurements.

During the experiment, the slight temperature rise on the sensitive film captured by the IR camera was subjected to post processing in order to extract the heat pattern on the film. This was performed based on Eqs. (2.10) and (2.11), utilizing LabView to visualize the amplitude and phase images of the heat distribution. Post processing can be used for several frequency harmonics, depending on the provided reference (synchronizing) frequency to deliver the clearest possible images. Selecting the proper frequency depends on the sensitive film properties and IR camera detection capability. As a result of the lock-in technique, the resulting amplitude images of the experimentally screened phantoms were

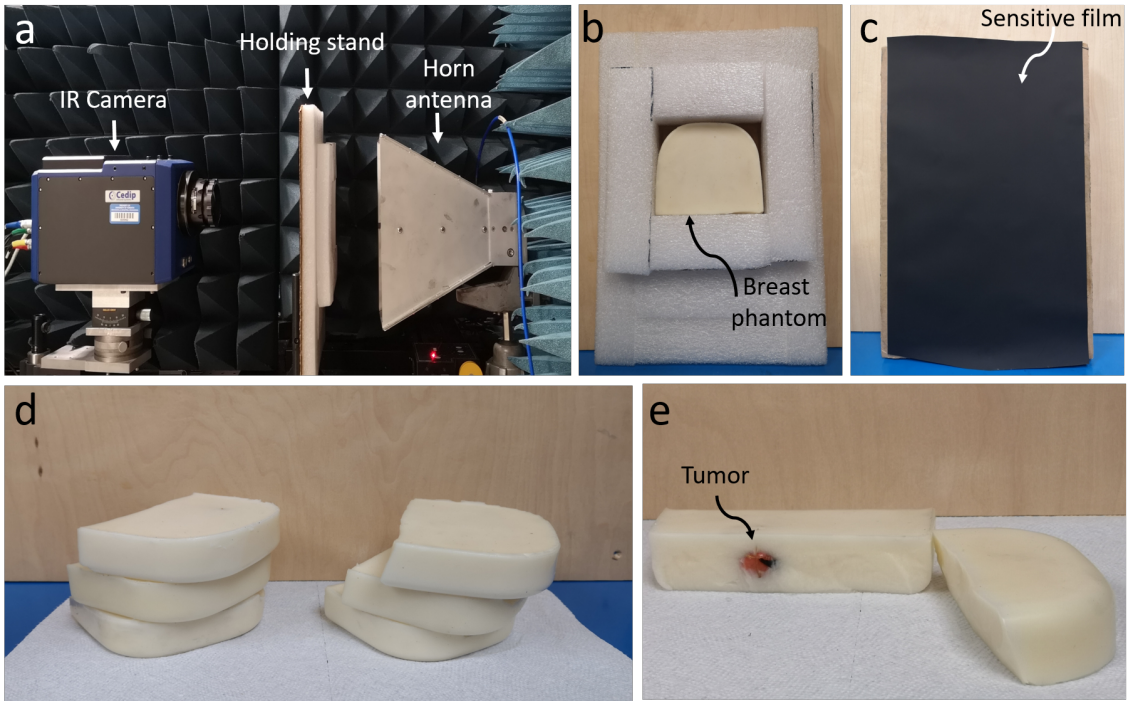

Figure 2.11: Microwave-thermography hybrid technique experiment. (a) The setup used in the experiment. During the experiment, the horn antenna is closer to the phantom's holding stand. The distance here is only for illustration. (b) Front view of the holding stand. (c) Back view of the holding stand. (d) The fabricated breast phantoms. (e) Cross-section of the tumorous breast phantom.

compared to detect tumor presence. The phase images are not of interest in this study since they provide less detection capability with this specific experimental setup.

The experimental validation of detecting tumor presence inside a breast was performed by screening two identical breast phantoms, one of which contained a spherical glass marble (tumor) of 5 mm radius at a depth of 15 mm from the breast bottom (the side touched the screen), located at (x=20, y=10, z=15). Fig. 2.12 (a) and (b) show the contrast between the electric field patterns of the normal and malignant breasts.

Obtaining quantitative experimental data requires alternating the tumor location and/or size inside similar breast phantoms. Therefore, two phantom sets with different size of tumor were first selected to have radii of 5 mm and 7.5 mm while the tumor location was fixed at (x=20, y=10, z=15). This test was intended to investigate the effect of tumor size

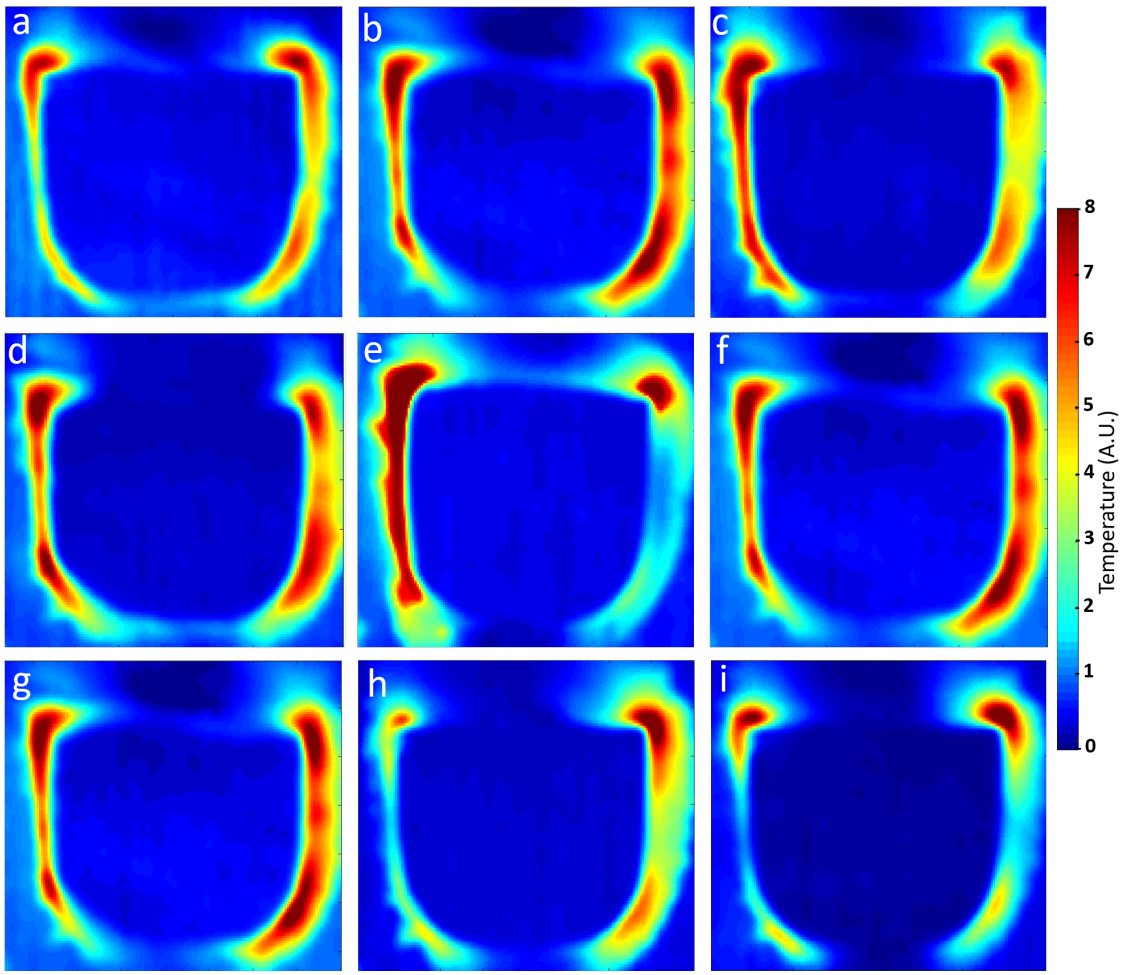

Figure 2.12: Heat pattern on the sensitive screen for (a) healthy breast, (b) tumorous breast with a 5 mm radius tumor, and (c) tumorous breast with a 7.5 mm radius tumor. The second row shows the heat patterns of a 5 mm radius tumor located at (d) x=5, y=5, z=15, (e) x=0, y=0, z=15, and (f) x=20, y=10, z=15. The third row presents the heat pattern of a 5 mm radius tumor under different radiation frequencies of (g) 0.7 GHz, (h) 1 GHz, and (i) 1.5 GHz.

on the field profile recorded on the screen. Fig. 2.12 (b) and (c) illustrate the difference in the heat distribution on the sensitive film as a consequence of a slight variation in tumor size. Secondly, in another set of phantoms, a 5 mm radius tumor was positioned at three locations of (20,10,15), (5, 5,15) and (0,0,15), in x, y, and z, respectively, hence one tumor location for each phantom. Similarly, by observing the heat expressions of the second set of experiments in Fig. 2.12 (d)-(f), it can be concluded that a change of tumor location and size can supply a different heat pattern that can be processed using machine learning to quantitatively extract the tumor features. However, in this study, due to the time and cost of the tissue-mimicking breast phantoms, machine learning was conducted based on realistic numerical phantoms. The machine learning system is trained using realistic numerical breast models that were built using realistic electrical properties of human breast tissue over a range of frequencies. Therefore, it is expected that, if there is a sufficient clinical dataset that acquired using this proposed technique, the developed machine learning system can be used as a machine learning module that can be implemented directly for the detecting and classification of the clinical data (not experimental data) that is obtained from clinical trials. It is worth mentioning that the fabricated tissue-mimicking breast phantoms that are utilized experimentally mimic real human breast properties but do not contain all types of breast tissue, which is the case with numerical breasts. It should be noted that all phantoms sets were subjected to radiation under the exact same conditions and radiation power during the entire experiment process. (Higher accuracy can be obtained by simultaneously radiating two breasts. However, such a setup was not available). The radiation modulation frequency generated by the signal generator was selected based on trial and error to find the higher image resolution, as can be seen in Fig. 2.12 (g)-(i).

2.6 Conclusion

This work presents a new breast cancer detection modality based on combining the tissue-penetrating capability of microwaves and thermography. The fundamental concept proposed here is established on using only the transmitted wave power to extract valuable detection-related data, thus the presence of a tumor in the breast is discerned by observing the thermal impression of an electromagnetic field. Therefore, our technique is strictly a detection rather than an imaging modality. This approach of visualizing an impression/projection of the transmitted/scattered energy strongly resembles mammography. However, in mammography, dense breast tissue blocks x-rays from reaching the film, whereas in the detection technique presented here, the source of radiation has low microwave frequency, which allows for deep penetration and illumination of the entire breast

tissue. When the entire breast is illuminated with the radiation source energy, all types of tissue become secondary radiators/scatterers.

Numerical investigation demonstrates the capability of detecting the presence of an anomaly as small as 4 mm in radius inside the breast. The role of machine learning enhances the performance of the proposed modality by improving the detection and characterization capability. Although breast asymmetry could increase the false positive rate, the use of machine learning further significantly enhances the detection reliability. The breast asymmetries in this study were in the tissue content distribution, not in the size/shape of the breasts, thus the change in the breast size/shape may result in incorrect detection results. Experimentally, lock-in thermography optimizes the contrast and allows the possibility of detecting a slight heat variation across a sensitive screen. Therefore, a small change in breast content can be successfully detected despite low radiation power. A 5 mm radius artificial tumor was detected experimentally, and changes in the size and location were observed by recording the heat on a sensitive screen.

Chapter 3

A Breast Cancer Detection System using Metasurfaces with Convolution Neural Network

3.1 Introduction

This chapter introduce a microwave-based system for detecting breast tumors. The fundamental concept is to record the transmitted electromagnetic energy through the breast, which scatters the radiation differently according to the variation in the electrical properties of the breast tissue. The energy captured by the metasurface forms an impression image of the breast under test. This impression is used as the detection tool to determine the presence of a tumor inside the breast. CNN is applied to enhance the detection's accuracy and to provide a quantitative data about tumors when present. Based on experimentation with breast phantoms for the purpose of demonstrating the feasibility of the method, numerical and experimental results demonstrated the possibility of finding a tumor with a 10 mm diameter, while determining the size and the location with an accuracy of over 91% and over 74%, respectively.

3.2 Theory

When electromagnetic energy encounters a lossy inhomogeneous medium, the energy is partially reflected and some of it propagates (transmits) through the medium. The signal

propagation phenomena is governed by the electrical properties of the medium's contents. In the case of a homogeneous medium extending infinitely in two orthogonal directions, the reflection and transmission can be analyzed and characterized analytically; however, if the medium is finite and inhomogeneous, as shown in Fig. 3.1, the transmitted energy cannot be represented using analytical expressions. Nevertheless, what is important here is the fact that the transmitted energy through such a medium is expected to provide a representation of the medium's contents, or an electromagnetic signature, or an electromagnetic impression. The transmitted energy can be recorded by a uniform sheet that is positioned underneath the OUT, which is placed on the opposite side of radiation source, thereby, a unique image or an impression of the medium can be obtained. Moreover, if the content of the medium is slightly perturbed, a different impression would be expected. It should be emphasized that the interest here is in obtaining a unique impression rather than an image of the internal tissues' composition. Additionally, It should be emphasized that the impression need not be visually giving direct resemblance of the medium internal composition in the sense that the naked eye would be able to determine the particular contents of the breast. What is important is that the signature be a unique expression of the breast content.

In chapter 2, a concept was developed where the electromagnetic-induced impression is captured (or recorded) by a temperature-sensitive absorption sheet [152]. In this chapter, instead of a temperature-sensitive sheet, the electromagnetic signature is captured by a metasurface, which is a surface composed of an ensemble of electrically-small printed resonators. Additionally, the metasurface eliminates the need for an infrared camera that was essential in our previous work.

By placing the metasurface in the close proximity of the OUT, the unit cells of the metasurface will be able to capture the field information carried by the transmitted signal. The metasurface in essence plays the role of the x-ray film when using x-rays to interrogate the human body or parts thereof. More specifically, this concept can be applied to create a breast cancer detection modality by placing the breast between an electromagnetic radiation source and a metasurface film as shown in Fig. 3.2. A horn antenna can be used as the microwave source to illuminate the breast with low-energy microwave radiation over a very narrow frequency band. The unit cells of the metasurface play the role of electrically-small antennas. The variation of the permittivity and the conductivity between healthy and cancerous tissues can affect the electromagnetic energy propagating through the breast, and more importantly, the energy that scatters off the breast tissues. Therefore, the energy footprint on the uniform surface can be affected by the presence of a tumor within the breast. The received electromagnetic power can be processed to form an image (i.e., an impression) that can be processed to reveal the presence or absence of

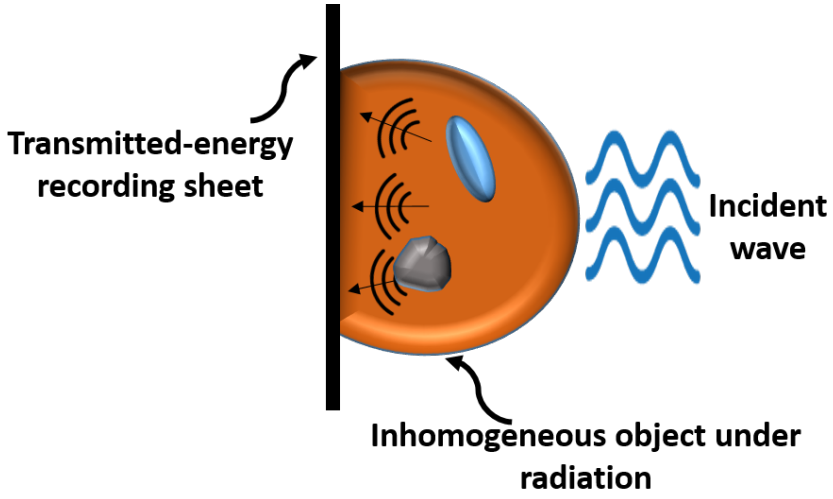

Figure 3.1: Illustration of the principle of the the metasurface detection modality. The inhomogeneous object represents the female breast and the metasurface is represented by the transmitted-energy recording sheet.

an anomaly in the breast. Comparing the impressions of the transmitted energy for the two breasts of a female subject, not simply by the naked eye, but with the aid of artificial intelligence, provides a valuable tool to detect breast tissue anomalies.

Unlike x-rays, the method introduced here uses microwaves. However, there is a strong similarity to how x-rays are used to provide an impression of an object. This similarity is not related to the physics of propagation of x-rays or microwaves, but rather to the setup needed to obtain an impression that reveals the inner composition of OUT. It should be noticed that in x-rays modalities, the film on which the x-rays impression is captured is placed very close to the OUT. In fact, in most cases, the x-ray film is placed as close as possible and even touching the OUT. The reason is related to confining the x-rays to the OUT because of potential harm (ionization) to other parts of the human subject. In our system, however, the primary reason for placing the metasurface very close to the OUT is to capture a signature that is uniquely (as much as possible) related to the OUT and not influenced by the surrounding media. Therefore, in our microwaves-based method, the metasurface is placed as close as possible to the OUT while illuminating the OUT with energy in the lower microwaves end of the spectrum. This brings into question the most suitable microwave frequency to be used in our system. Due to the complex nature of imaging (or obtaining an impression) for breast tissues, the optimal frequency will most likely be determined empirically. However, at this stage, the frequency chosen should be

such that it is sufficiently low to fully penetrate and illuminate the entire breast tissues, while not high enough to prevent ray-like multiple scattering that does not lead to a sufficient image resolution that resembles the constituents of the breast.

3.3 Numerical Experiments

Without any loss of generality, the metasurface used in this work consists of a 10 x 10 unit cells. While the literature is replete with a variety of unit cell topologies, the one chosen in this work is the ELC resonator that consists of two back-to-back split ring resonators with a ring in the middle [153]. The ELC cell is hosted on top of 3.175 mm thick Rogers TMM10i dielectric substrate with a dielectric constant of ϵ_r= 9.8, and a loss tangent of tan δ = 0.002 as seen in Fig. 3.3(a). The substrate was chosen to minimize the dielectric loss of the absorbed electromagnetic power in the unit cell, hence maximum energy absorption of the unit cell occurs in the resistive load of the unit cell [88]. The substrate is backed by a metallic plane to serve as a shield to prevent interference with any objects beneath the surface. The ELC was designed and optimized to resonate at 1.9 GHz, resulting in the following dimensions of the ELC: L = 10 mm, W1 = 1.4 mm, W2 = 0.6 mm, g = 0.5 mm, s1 = 0.5 mm, s2 = 1 mm, t = 3.175 mm, and copper thickness of t = 35 μm as illustrated in Fig. 3.3(a). It should be emphasized that this particular frequency was not the result of empirical based optimization, but only to fit within the considerations mentioned above. The inherent narrow-bandedness of electrically-small resonators, such as the ELC unit cell employed here, highlights the importance of illuminating the field with a narrow-band signal as mentioned above.

The electromagnetic full-wave simulator CST Microwave Studio was used in the design and optimization of the unit cell [154]. The ELC cell was characterized by placing it inside a waveguide with two excitation ports and a perfect electric conductor boundary condition in the xz plane, a perfect magnetic conductor boundary condition in the yz plane, and an open boundary condition normal to the z-direction (refer to Fig. 3.3 for the coordinate system used in modeling). Applying these boundary conditions force the electrical and magnetic fields to be parallel to the ELC surface to generate an incident TEM mode. In order to maximize power absorption and delivery in the ELC cell, two critical parameters were carefully considered: the position of via and the value of the resistive load. The optimal via position maximizes the current flow from the surface of the unit cell towards the load (as illustrated in Fig. 3.3 (b)), whereas the optimal resistive load allows maximum power transfer to the load. The optimal resistance value of 100 Ohm was found to be the same value as the impedance of the ELC seen from the load. Therefore, each unit cell

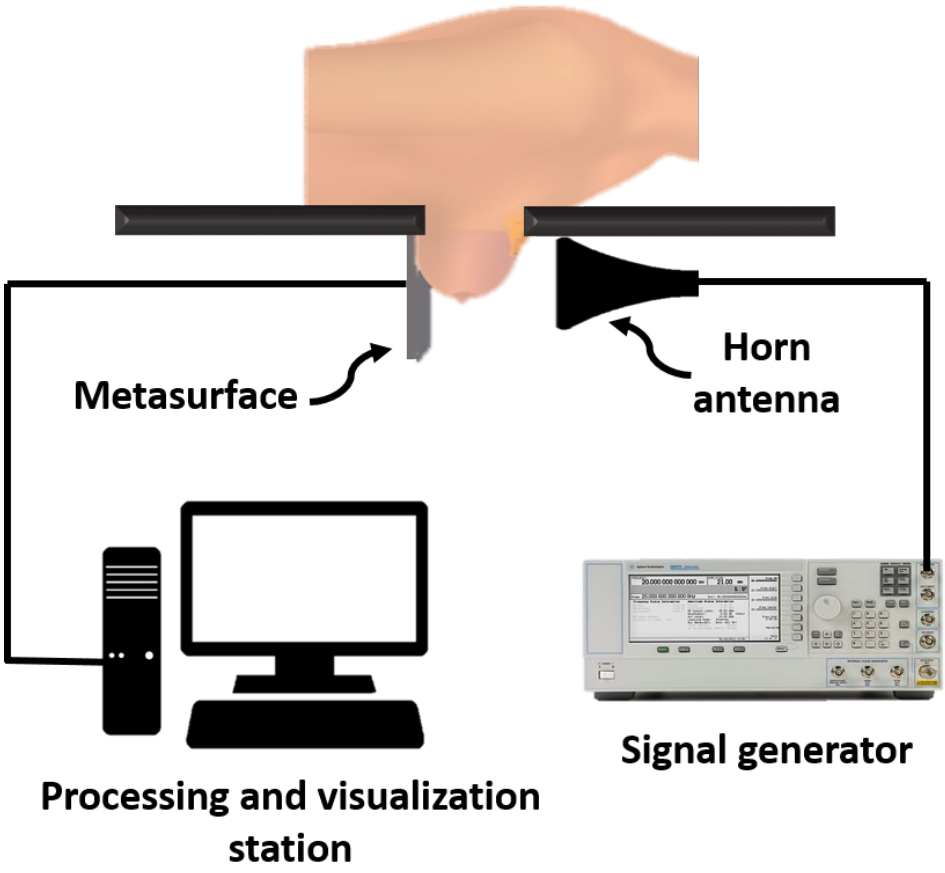

Figure 3.2: Schematic diagram of the setup of the proposed breast cancer modality.

was terminated by 100 Ohm. This resulted in maximum power dissipation across the terminated load at 1.9 GHz as shown in Fig. 3.3(c).

Under a plane wave radiation, a uniform distribution of the surface current was observed on the surface of the metasurface at the resonance frequency as shown in Fig. 3.4(a). However, as a result of the change of the input impedance of the ELC at the upper and lower edges (in y-direction) of the metasurface, the surface current and the power in the resistive loads of the ELC cells on those edges are expected to be different from the rest of the unit cells. The difference in the surface currents on the edges in the x-direction was not observed to be as severe due to the specific polarization of the excitation field [155].

In order to design a realistic numerical breast model, simulation analysis for breast

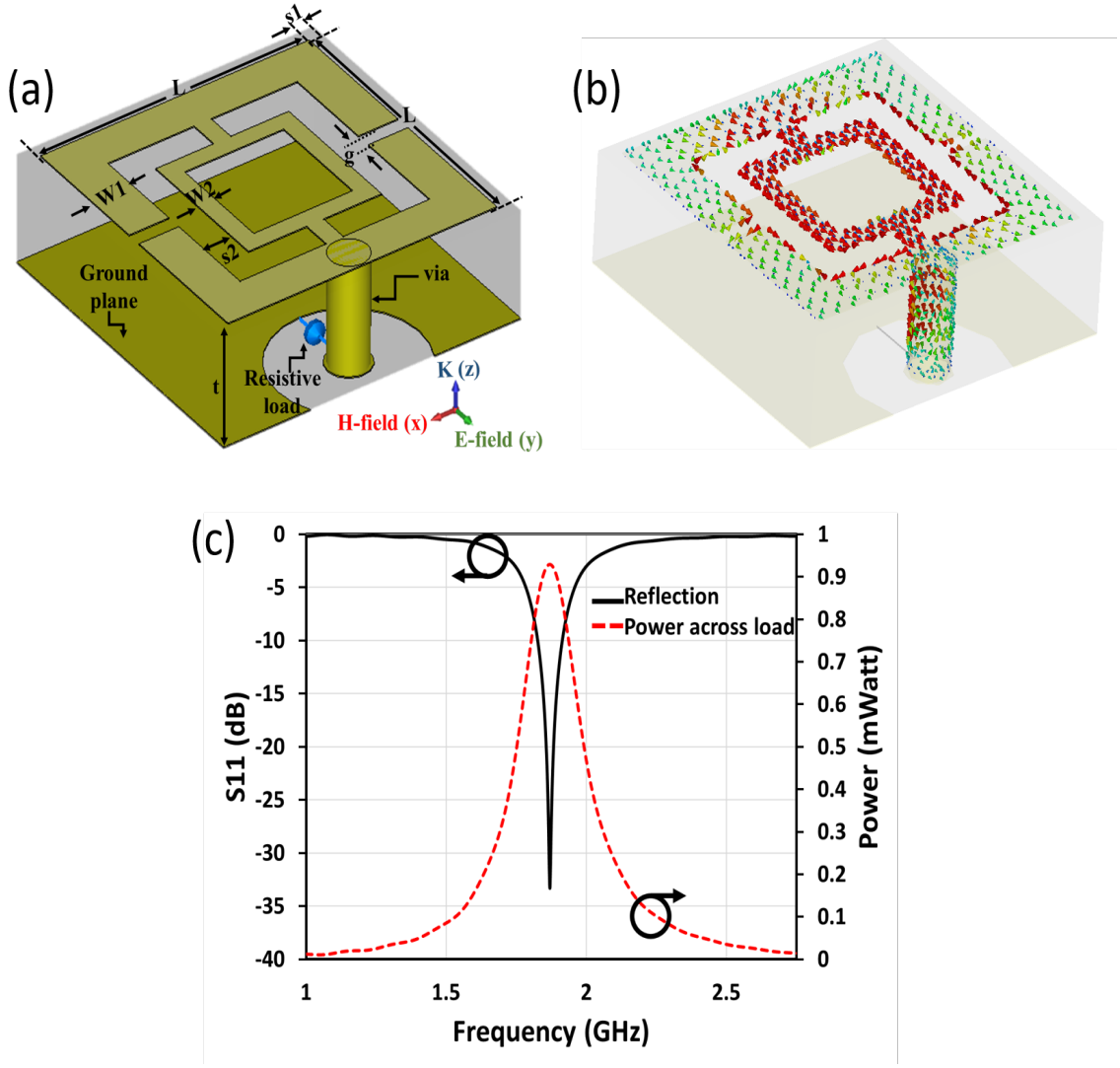

Figure 3.3: (a) Schematic showing the designed ELC unit cell. (b) Schematic of the current surface flow on the ELC surface and through the via toward the terminated resistive load. (c) Simulation results of the unit cell showing the reflection coefficient S_{11} and the power dissipated in the resisitive load at the resonance frequency of 1.9 GHz.

cancer studies needs extensive understanding of the contents of breast tissue. The breast consists of a combination of fibroglandular and fatty tissue, where the proportion of fibroglandular tissue dictates breast density [126]. The American College of Radiology

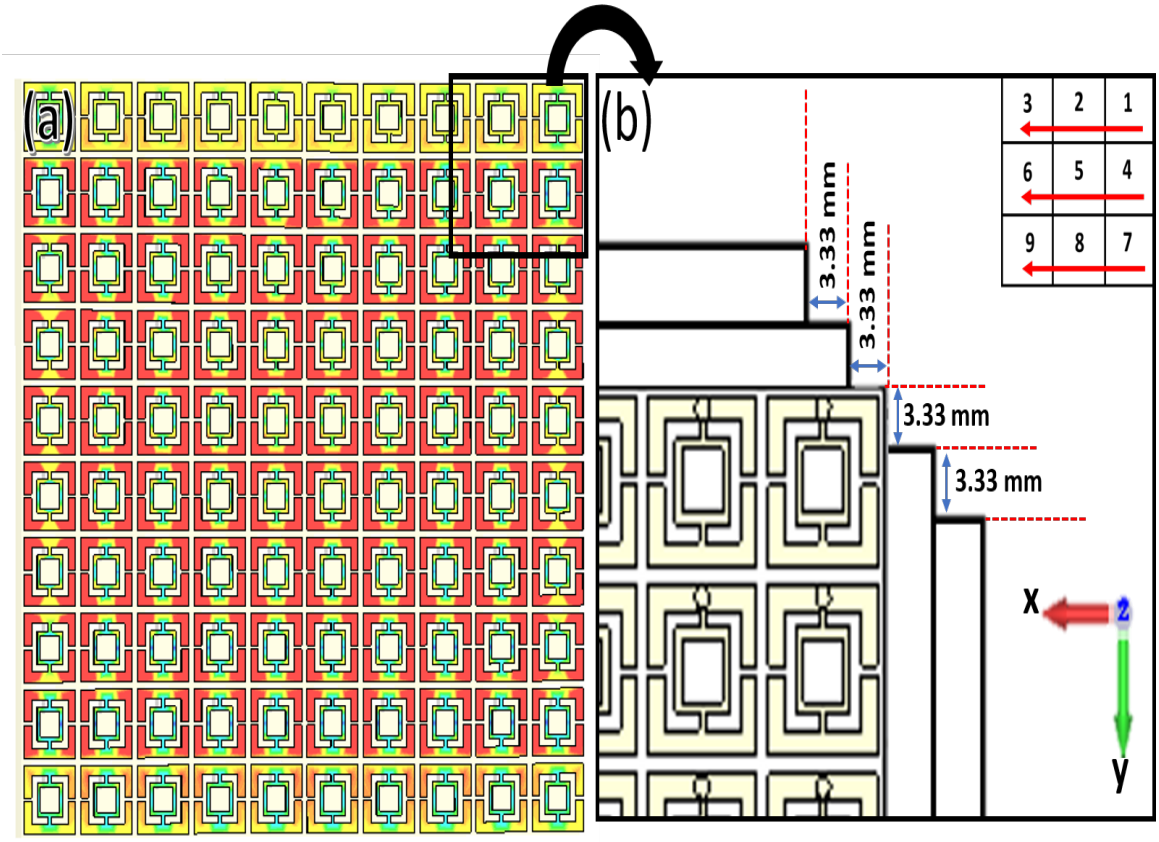

Figure 3.4: (a) The distribution of the surface current on the ELCs at the resonance frequency. The red color represents the highest intensity which is 112 A/m, and the blue color represents the lowest intensity which is 0 A/m. (b) The scanning procedure of the metasurface showing the length and direction of the scan steps. Inset illustrates the scanning steps sequence.

categorized the breast into four classes, depending on the density of the tissue: Class A, extremely dense breast (more than 75% fibroglandular tissue); Class B, heterogeneously dense (75% to 50% fibroglandular tissue); Class C, fibroglandular scattered areas (50% to 25% fibroglandular tissue); and Class D, almost entirely fatty (less than 25%). The last two groups are labeled as non-dense breasts, whereas the first two groups are labeled as dense breasts. It should be noted that the breast density is correlated with a greater risk of developing breast cancer (in USA, approximately 50% of women have dense breasts [127, 156]).

When examining heterogeneously and extremely dense breasts, mammography poses difficulties since cancerous tumors and dense tissue do not present a sufficient contrast [128]. Therefore, this research primarily focuses on the efficacy of the system developed here for detecting early stage cancerous tumors in dense breasts.

In this work, the breast models were designed using different biological breast tissue contents and specifying the electrical properties for each tissue. In CST, an extremely dense breast was designed using built-in human biological tissue, while considering the variations in the content of the tissue in order to realize a realistic biological breast. The prototypes of the breast were modeled as a hemispherical breast of 50 mm radius consisting of 2 mm thick skin and 65 mm internal tissue composed of fibroglandular and fat tissue, as illustrated in Fig. 3.5(a). Realistic dielectric properties were assigned to the tissues of the breast model by CST at 1.9 GHz based on the human dielectric properties database [130]. It should be noted that the electrical properties of the breast tissue change with frequency without any interference from the user. The relative permittivity and electrical conductivity were considered to be 58 and 1.56 S/m, for fibroglandular tissues, and 5.25 and 0.1 S/m for fat tissues. The permittiity contrast between cancerous and healthy tissue was assumed to be approximately 2:1 to ensure low contrast as reported in previous studies [135]. Therefore, the dielectric constant and electrical conductivity of the tumor were proposed to be 100 and 4 S/m. It should be emphasized here that precise values of the dielectric properties of the breast tissues including tumors is not important for the applicability of our method. The method hinges primarily on the contrast between the tissues' properties. The surface of the breast was flattened to decrease the breast thickness and to create a consistent surface region, thus the breast was evenly radiated. The flattening of the breast is similar to the flattening that takes place in mammography.

3.3.1 tumor detection

The system for breast cancer diagnosis proposed here relies on two basic factors: (i) the average female breasts have symmetrical content and structure; and (ii) The extremely low likelihood that a cancerous tumor occurs in both breasts at the same time. The detection strategy in this study is conducted by using the same source of microwave radiation for both breast phantoms. The recorded electromagnetic energy on the metasurface film (the power dissipated in the resistive loads of the ELC cells) is then evaluated for determination of tumor presence within the breast. Determining the presence of a tumor by relying solely on the naked-eye's direct observation of the energy signature may lead to a detection error. However, as shown below, the use of artificial intelligence can significantly increase the detection accuracy.

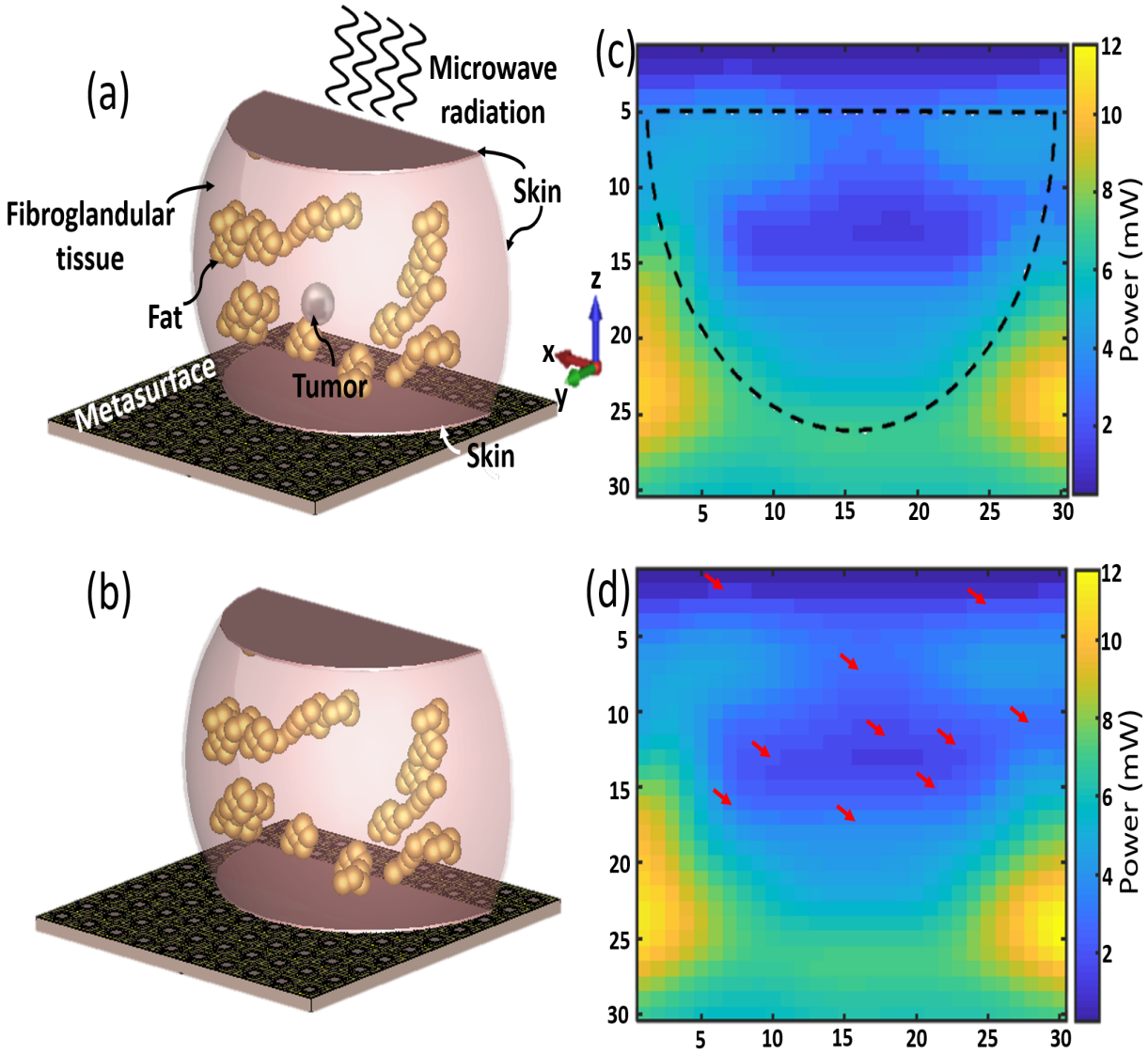

Figure 3.5: Models of an extremely dense breast. (a) With a 10 mm tumor. (b) Without a tumor. The recorded power pattern on the metasurface film for different breasts. (c) With a cancerous tumor. (d) Without a tumor. The red arrows indicate the location of some difference compared to (c)

The size of the metasurface array is 10 cells × 10 cells, which provides an impression

with a 100-pixel resolution. Such a resolution may not be sufficient. Therefore, in order to increase the resolution, the entire metasurface was moved in the xy plane by a fraction of a unit cell. The first three scan steps were in increments of 3.33 mm (equivalent to one-third of the length of the unit cell) in the x-direction. Then, the metasurface was returned to its initial location (x=0, y=0) and moved one step by 3.33 mm in the y-direction. This followed by three uniform steps in the x-direction. Next, the metasurface was returned to its initial location (this time at x=0, y= 3.33 mm) and moved again one step in y direction by additional 3.33 mm to be at x=0, y= 6.66. Then the three steps in the x-direction are repeated again as seen in Fig. 3.4(b).

Applying this scanning technique created a virtual metasurface with a 30 $\times$ 30 pixels, thus increasing the effective resolution by three time while eliminating the need to miniaturize the unit cells. Although increasing the scanning steps increases the resolution, the scanning steps applied here were found to be sufficient to prove the feasibility of the proposed method.

Two identical and extremely dense breast models were constructed including a tumor with an electrical conductivity and relative permittivity greater than that of fibroglandular tissues and with a diameter of 10 mm (see Fig. 3.5(a) and (b)). The breasts were illuminated by a plane wave with an electric field intensity of 150 v/m. The power impressions recorded by the metasurface for breasts with and without a tumor, are shown in Fig. 3.5(c) and (d). The observed results show that the recorded power impression for the normal breast differed from that of breast without a tumor. The tumor was positioned at a distance of approximately 25 mm from the metasurface film (in the z-direction; see Fig. 3.5). Several techniques were used utilizing Matlab to enhance distinguishing of the differences between the images of this chapter(i.e., Figs. 3.5 - 3.8. The results are included in Appendix A)

Different tumor sizes with diameters of 8 mm, 10 mm, and 12 mm were inserted inside identical breast models (one tumor for each breast). The location of the tumors inside the breasts were fixed, while the depth of the tumors (distance form the metasurface) were maintained at 20 mm. Despite a small change in the tumor size, the influence on the transmitted energy is noticeable as seen in Fig. 3.6. The tumor with a diameter of 8 mm had a slight change on the power impression compared to the reference (healthy breast). However, for tumors with diameters of 10 mm and 12 mm, the change in the power impression was more pronounced. Thus, When the tumor becomes smaller in size and deeper inside the tissue, detecting the abnormality becomes more difficult. However, the flexibility of implementing this technique allows applying the test either vertically, where the microwave source is above the breast and the metasurface is positioned below the breast, or horizontally, where the microwave source is on the left side and the metasurface

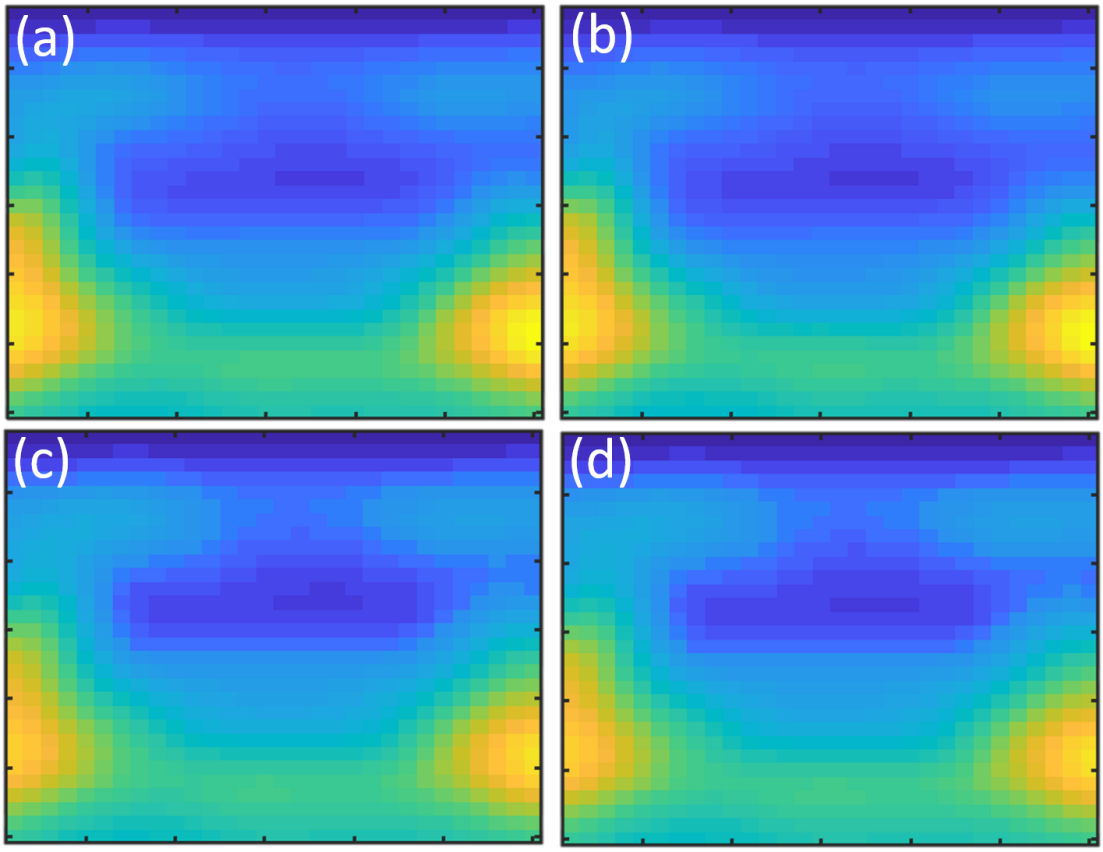

Figure 3.6: Captured power pattern of the breast: (a) without tumor (reference), (b) with an 8 mm diameter tumor, (c) with a 10 mm diameter tumor, and (d) with a 12 mm diameter tumor.

is on the right side of the breast, and vise versa. Adopting such implementation addresses the challenge of detecting small and deeper tumors. It should be noted that a breast cancer tumor with diameter of 20 mm is considered as an early stage breast cancer [157, 158].

The tumor location inside the breast was changed in order to examine the influence of the location on the power impression. The size of the tumors was kept at 10 mm, and tumor locations was changed in the x- and y- directions, while fixing the location in z-direction at 20 mm (see Fig. 3.7 (a)-(c)). The corresponding power impressions are shown in Fig. 3.7 (d)-(f). Next, the depth of the tumor inside the breast (the distance from metasurface

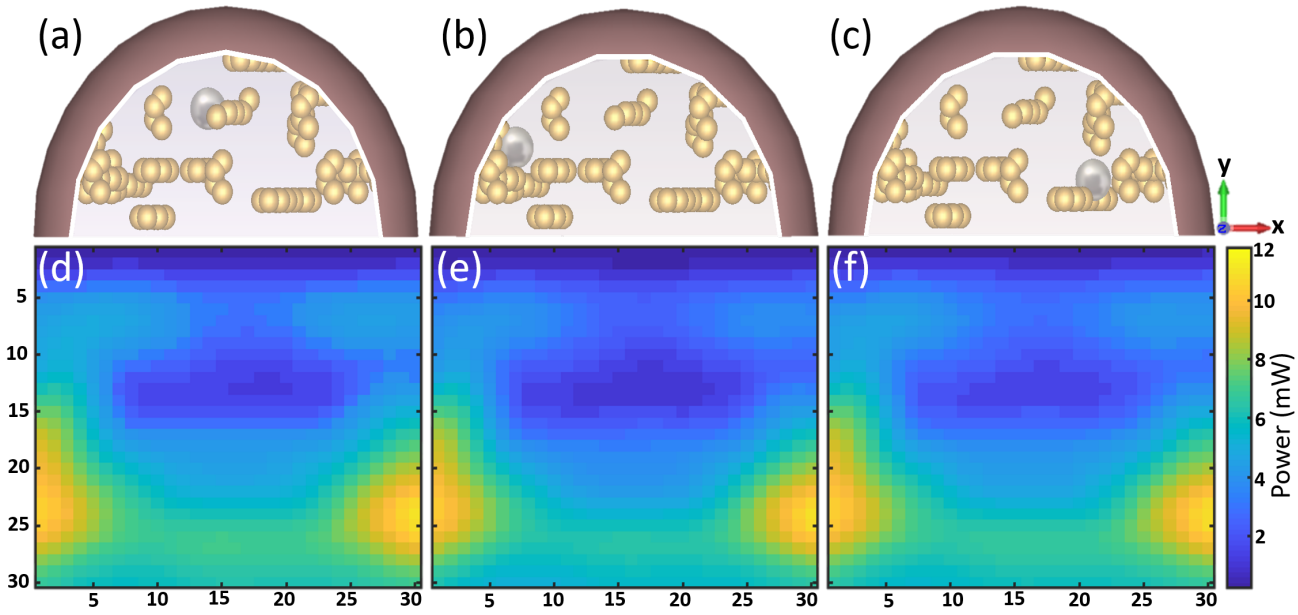

Figure 3.7: Different tumor positions at (a) x=-2, y=5, z=20, (b) x=-10, y=0, z=20, and (c) x=10, y=5, z=20, and corresponding power signatures on the metasurface film at (d), (e), and (f), respectively.

in the z-direction) was varied resulting in the impressions shown in Fig. 3.8.

3.4 Convolution Neural Network

Since there is a difference in the densities of breast tissues, the analyses of breast medical images resulting from various imaging techniques is typically subjected to the radiologist's expertise with significant probability of misdiagnoses. In fact, around 25% of breast cancer cases are misdetected or deemed as false-negative [159]. Here, it is shown that artificial intelligence can be used to enhance the detection accuracy.

As a detection improvement for MRI brain images, CNN was used to diagnose Alzheimer's diseases that correspond to anatomical brain landmarks [103]. Zhou et al. used an end-to-end learning approach to manipulate a CNN to automatically find and segment the computed tomography results of an abdominal organ [104]. Recent research studies proposed a stand-alone system for breast cancer detection, achieving results that match those of an

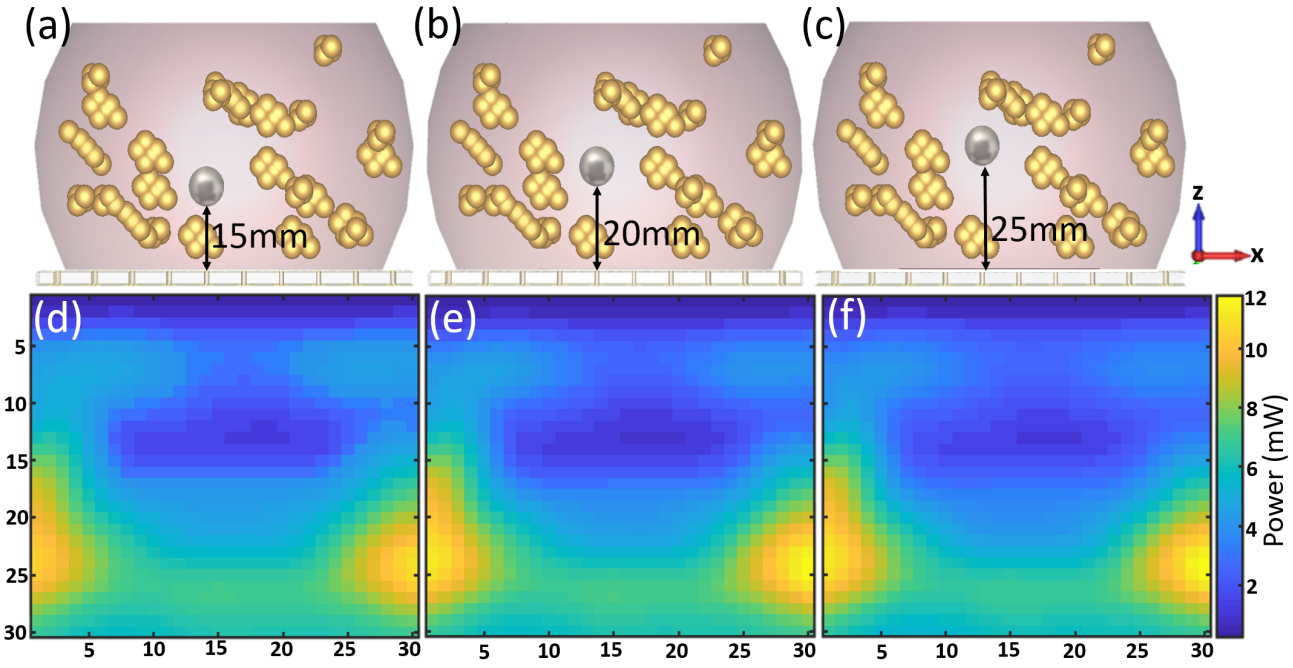

Figure 3.8: Change in the depth of the tumor location inside the breast (distance from the metasurface) and the consequent effect on the recorded power distribution.

average radiologists [160]. In addition to the qualitative findings (the mere determination of the presence or absence of a tumor), CNN may help determine the tumor's quantitative characteristics such as its position and size, which are not easy to determine by a naked-eye examination of the electromagnetic energy impression recorded by the metasurface.

In addition to enhancing the detection accuracy, the key aim of incorporating machine learning is to improve the detection performance in two areas that are not currently covered by other breast cancer diagnosis methods: i) identifying the tumor that exists when both breasts are asymmetric; and ii) recognizing the tumor characteristics in terms of size and position. To this end, 20 extremely dense breast phantoms, consisting of various types of internal tissue, were developed and examined using CST to produce the necessary dataset (the set of the power impression images) for a machine learning procedure. Dense breast models were composed of about 10-25% breast fat tissue and 75-90% fibroglandular tissue. Towards obtaining a perfect asymmetry of each designed breast, a specific internal architecture was assigned for each breast.

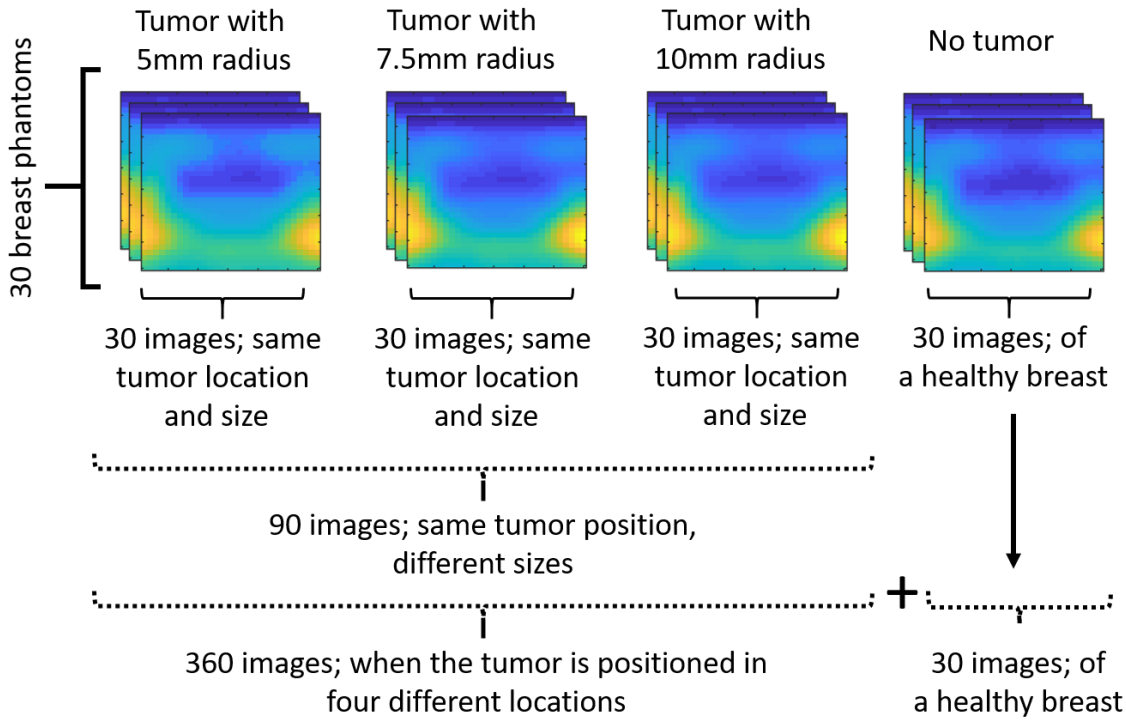

Figure 3.9: Schematic showing the procedure of generating and organizing the dataset for CNN where 30 different breast models were used to generate 30 images of healthy breasts and 30 images of non-healthy breasts. Three tumor sizes for the same location resulted in 90 images. For four tumor positions, the number of images increased to 360.

The first series of simulations of the breast models was conducted without embedding a tumor inside the breasts in order to generate the power pattern images of non-identical healthy breasts. Such a step provides the first dataset that consists of 30 images of healthy breasts. In order to generate the second dataset (images) of variant-tissue tumorous breasts, the simulations were conducted after a tumor was inserted inside each breast model, with a defined position and size for each tumor. The tumor location was altered at four different positions: (-5, 10, 20), (10, 10, 25), (-15, 5, 10), and (25, 0 , 0). For each tumor position, three tumor sizes, namely diameters of 10, 15, and 20 mm, were considered. The obtained dataset from the second series consisted of 30 images for each tumor position with a fixed size and 90 images for each location of the tumor, regardless of the tumor size (i.e., 30 images $\times$ three different sizes). As the tumor location changed between four different positions, the total increased to 360 images (30 $\times$ three sizes $\times$ four

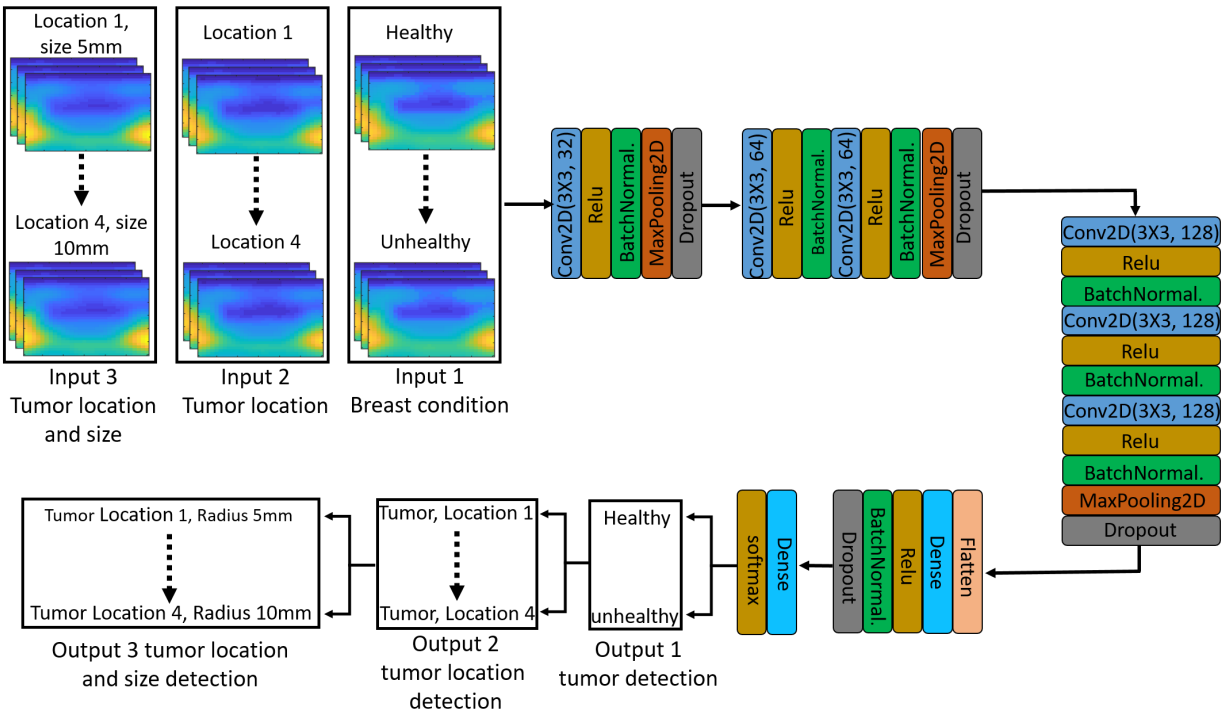

Figure 3.10: Schematic illustrating the CNN for the hybrid technique. The three dataset inputs for the CNN system shown are: Input 1 assigned for detecting tumor presence; Input 2 assigned for tumor location detection; and Input 3 assigned for tumor location and size detection. The CNN framework is shown after the input, where the blue square shows the size and number of filters for each convolutions layer. The left part of the figure is the categories for each input set.

positions = 360 images), as shown in Fig. 3.9.

In order to first train the CNN to differentiate between a healthy and malignant breast, even while considering that all breasts contain up to 25% variance in internal tissue, 30 healthy breast images were assembled as an individual group and labeled as a "healthy breast" set to be compared with another 30 tumorous breast images that were labeled as a "malignant breast" set. Secondly, obtaining quantitative data about tumors from cancerous breast images necessitates coordinating the dataset in a proper approach that trains the CNN classifier to extract the position and size of the tumor. Accordingly, based on the tumor's position, four groups of malignant breast images, consisting of 360 images (90 images for each group), were labeled as "Location 1", "Location 2", "Location 3" and

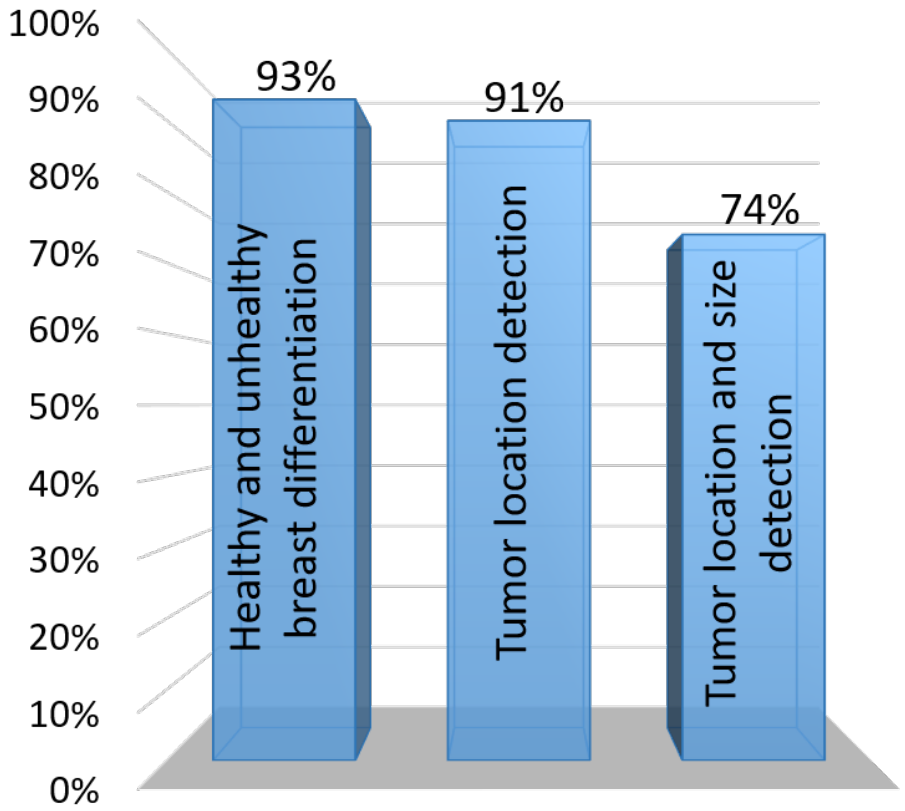

Figure 3.11: Machine learning results. The accuracy of distinction between breasts with a cancerous tumor and a breast containing healthy tissue in asymmetrical internal tissue breasts is shown in the left bar. The middle bar represents the accuracy of detection tumor location. The right bar shows the accuracy of detection of the tumor size and location simultaneous.

"Location 4", and allocated to train the CNN to evaluate the 3D location of the tumor inside the breast. Similarly, the 360 images were organized to create twelve groups (30 images for each set) describing the size and position of the tumor, then assigned to train the CNN to concurrently determine the location and size of the tumor.

The datasets, which were imported as an input for the CNN to be entered into multi-stage processing, begin with data prepossessing, classification, and training, and end with the testing stage. The structure of the CNN system is shown in Fig. 3.10, including the dataset entry configuration and the output classification for each input group. The datasets

were randomly split into 80% training and 20% evaluation (testing) sets. The CNN system uses the training set to establish the connection between the input and the output, while the testing data helps to measure the accuracy of the system (i.e., how accurate the decision of the system becomes after training).

The obtained accuracy is illustrated in Fig. 3.11. Although the dataset is relatively small, the performance results reveal that it is sufficient to train the system and achieve good detection accuracy. In terms of distinguishing between healthy and malignant breasts among asymmetric breasts models, the system exhibits an accuracy of approximately 93%, as shown in Fig. 3.11, in determining which breast has a tumor and which does not, in spite of the variation of internal tissue content even in the same breast category (i.e., healthy or malignant). Moreover, the position of the tumors was localized with a performance accuracy of about 91%, while the determination of the size and location simultaneously shows 74% accuracy, as seen in Fig. 3.11. It should be emphasized that the machine learning system performance can be substantially improved by increasing the dataset for each image group category and improving the CNN algorithm, which will be developed in a separate future investigation.

Table 3.1 lists the classification report for each class of the dataset after passing through the CNN. The table specifies the precision, recall, F1-score, and support score for each input class individually. The precision, which is the percentage of the correct predictions, of the healthy vs unhealthy breasts has values of 0.75 and 1 for the healthy and unhealthy classes, respectively. The percentage of the founded positive cases by the CNN is known as recall, and for the two classes (i. e; healthy and unhealthy), the recall was 1. The F1 score represents the harmonic mean of the precision and recall, and it defines the positive prediction percentage that was correct, where Support represents the number of samples for each category of the dataset. The value of the F1 score and the Support can be seen in Table 3.1. Similarly, the classification report for each input of the dataset is listed in Table 3.1.

3.5 Experimental Validation

3.5.1 Breast phantom fabrication

Realistic breast phantoms that mimic the real human breast properties were fabricated. The breast phantoms were fabricated using the oil-in-gelatin methodology [161], whereas the tumorous breasts were fabricated according to [162]. Both techniques established the

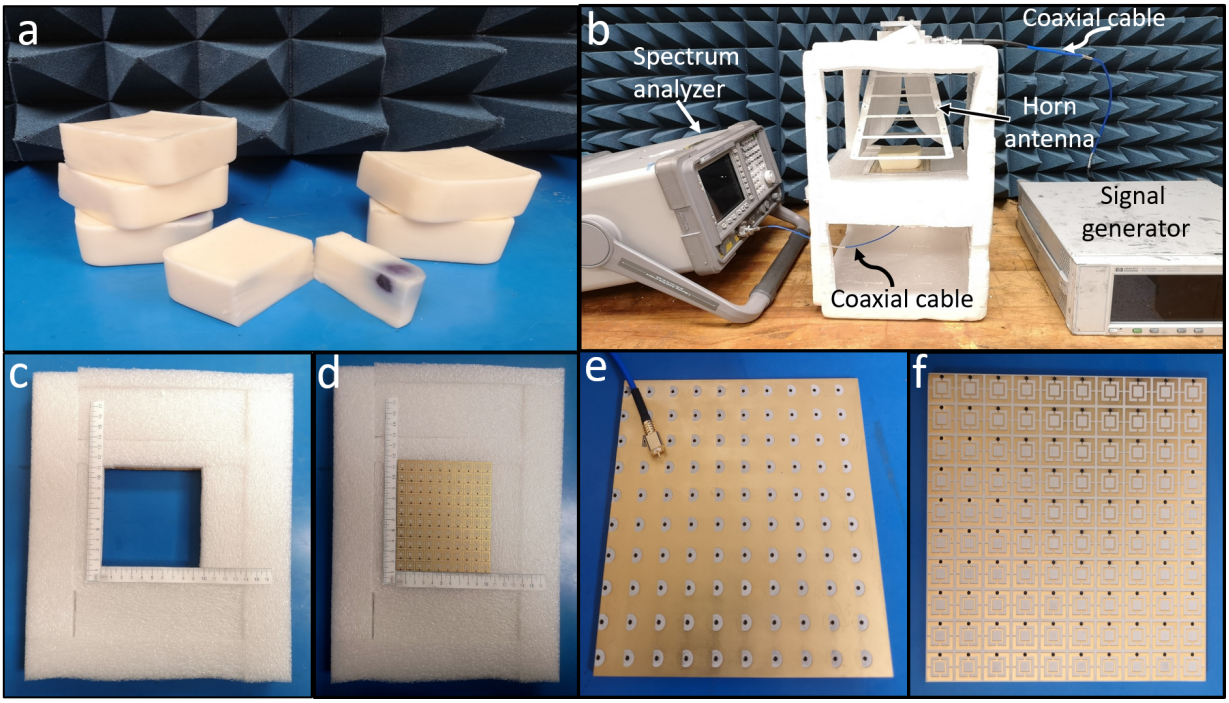

Figure 3.12: The experimental procedure of metasurface detection modality. (a) The experiments setup. Top view of the metasurface-phantom holder (b) without metasurface sheet, and (c) with the metasurface sheet. (d) The designed breast phantoms including a cross-section of one of the tumor embedded phantoms.

fabrication methodology based on the measured electrical properties of ex vivo breast tissues [163, 164, 17, 165, 166]. The composition of the breast phantom consisted of an aqueous gelatin mixture (bovine gelatin and demonized water) and an oil solution (half kerosene and half safflower oil). The electromagnetic properties of the phantoms were varied by adjusting the volume percentage of the phantom components, thus the desired breast tissue (category) can be constructed precisely. Adopting this fabrication methodology, the breast phantoms can mimic the electrical properties of the biological breast tissue over a broadband of frequency that contains the operation frequency of interest in this study.

The extremely dense breast phantoms were fabricated by adjusting the concentration of the oil solution into the gelatin mixture to be 20%. In case with a tumor, the mixture did not contain kerosene and had less oil percentage to achieve higher electrical properties compared to the hosting tissue (fibroglandular). Six phantoms were built to conduct the

qualitative and quantitative experimental parts (Fig. 3.12(a)). One breast phantom had no tumor to represent the healthy breast, whereas the rest were implanted with tumors. The tumors location and size were altered in each breast phantom to supply different phantom features for more dependable experimental validation.

3.5.2 Experimental procedure and results

The experimental system was designed by preparing a stand that can hold the radiation source (a horn antenna) and the metasurface-phantom holder as shown in Fig. 3.12(b). The metasurface-phantom holder has an open window that allows conducting the measurements through the backside of the metasurface while holding the metasurface sheet and the breast phantom on the top as illustrated in Fig. 3.12 (c) and (d). Two sides of the holder's window were scaled metrically in order to allow for precise breast scan. Such an experimental setup provides a simple radiation and measurements approach during the process of the experiments. A microwave signal with an amplitude of 20 dBm at 1.9 GHz was generated by an HP E4422B signal generator. This signal was then fed to the horn antenna to irradiate the breast phantom which is positioned at a standoff distance of 2 cm from the antenna. The metasurface was placed directly underneath the phantom to absorb the transmitted electromagnetic energy after propagating through the breast.

The power that arrives at the metasurface was recorded at each unit cell individually. A coaxial cable with an MCX PCB end launch jack and a second end connected to a spectrum analyser (Agilent E4407B) was used to measure the power in the load of the unit cell. The back of the unit cells was designed in a way that allows the pin of the MCX jack to slip inside the via, while the outer case of the cable would be connected to the ground plane as shown in Fig. 3.12 (e). The top layer of the fabricated metasurface array can be seen in Fig. 3.12 (f). The measurement of the power was conducted for all 100 unit cells. Then the measurements were repeated after incremental shifts in a manner identical to the numerical setup discussed above in order to enhance the resolution. The entire recorded measurements of all scanning steps were transferred to Matlab to reconstruct the capture power signature. It should be noted that the measurements were conducted for each unit cell while all other remaining unit cells were open-circuited. (In a more practical scenario, which is beyond our logistical capability, all unit cell can be connected to coaxial cables simultaneously.)

Two identical phantoms, one of which had an embedded synthetic tumor, were subjected to microwave radiation. The embedded tumor has a 10 mm diameter placed at a distance of 40 mm from the breast bottom that touches the metasurfce sheet, and positioned at (x=20 ,y=20 ,z=20) assuming the breast bottom center is the origin (i.e., x=0,

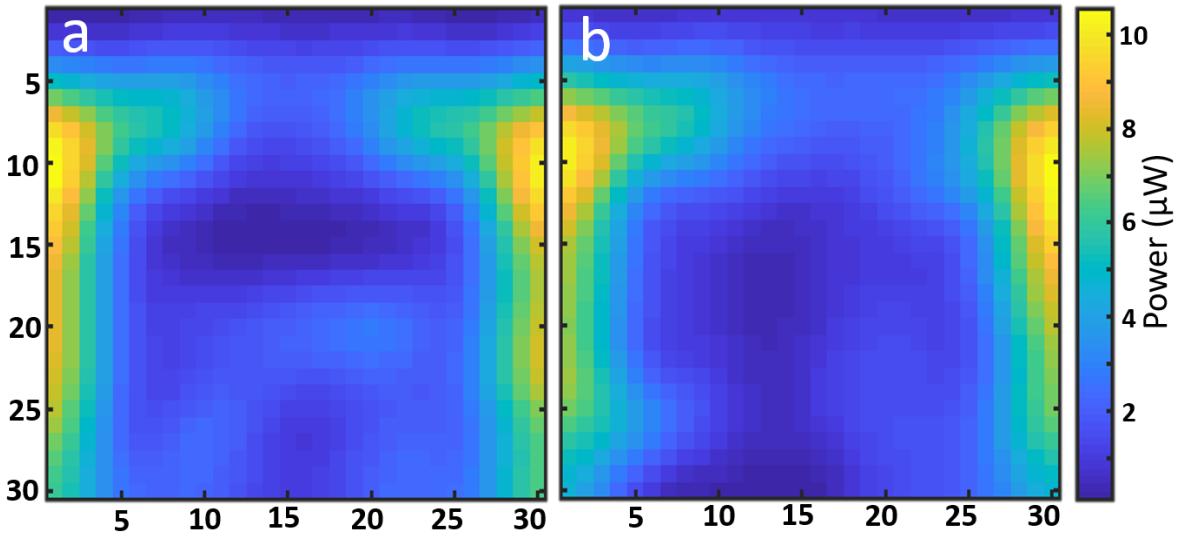

Figure 3.13: Measured power pattern on the metasurface film for the phantom (a) without a tumor and (b) with a 10 mm diameter synthetic tumor.

y=0, z=0) while z is pointing in the breast height direction. The contrast in the power signature between the healthy and tumorous phantoms is shown in Fig. 3.13.

To provide a quantitative assessment of the tumor features, the synthetic tumor size and/or location were changed inside the fabricated phantoms. First, the tumor was positioned in three different locations (x=20, y=20, z=20), (x=-20, y=0, z=30), and (x=0, y=-15, z=10) inside three identical breast phantoms, while the tumor diameter remained the same (15 mm). Subjecting these phantoms to the same radiation conditions resulted in a different energy expression for each phantom (see Fig. 3.14 (a), (b) and (c)). Second, to determine the effect of tumor size on the obtained energy signature, the tumor size was slightly increased to have three different sizes (10, 15 and 20 mm in diameter), while fixing the tumor position. Likewise, by comparing the resulting power signatures of these three breasts in Fig. 3.14 (d), (e) and (f), it can be determined that the change in tumor size and/or location provides a unique energy-related expression that can be used to extract quantitative data about the tumor. It should be noted that during the experimental procedures, breast phantoms were illuminated with exactly the same radiation intensity under identical conditions. The distinction between healthy and tumorous breasts can be significantly improved if both breasts were illuminated simultaneously, however, this setup

required additional resources that were not available to us.

Finally, it should be noted that the machine learning study in was implemented on realistic numerical phantoms, which comprise all breast tissue types, not on fabricated breast phantoms. This work, however, will limit the machine learning to the numerical phantoms because of the following reasons: a) The difficulties of fabricating accurate realistic breast phantoms that have similar accuracy to the numerical phantoms, and b) The time and cost of fabricating such breast phantoms (about 260 phantoms are required for this study). However, due to the accuracy of detection achieved using the numerical phantoms, training the proposed machine learning system on the numerical phantoms can establish a machine learning model that can be involved in the clinical trails to classify, detect, and determine the breast status.

3.6 Conclusion

This paper presents a breast cancer detection technique employing a metasurface as the sensor platform and machine learning to enhance the detection accuracy. The principle behind the detection system is based on capturing and comparing the transmitted energy through the breast utilizing a metasurface that consists of electrically small unit cells. Since the detection modality here is based on the energy impression of the breast, it should be emphasised that this technique is a detection rather than an imaging approach. This approach shows a similarity with mammography in the sense that an impression of the breast is constructed, however, while having the advantage of using microwave non-ionizing radiation with the ability to penetrate dense breast tissue.

The numerical and experimental evaluation of the proposed technique show the feasibility of the proposed technique in detecting the tumor presence inside the breast down to 10 mm diameter, and also determining the tumor location and size. Adopting the small steps scan of the metasurface increase the resolution of the captured-energy impression while keeping the size of the unit cells unchanged. Moreover, in case of asymmetrical breasts, the CNN is able to distinguish between healthy and tumorous breasts despite the change in internal tissue distribution. In addition, CNN provides the ability to extract quantitative information about the tumor such as location and size.

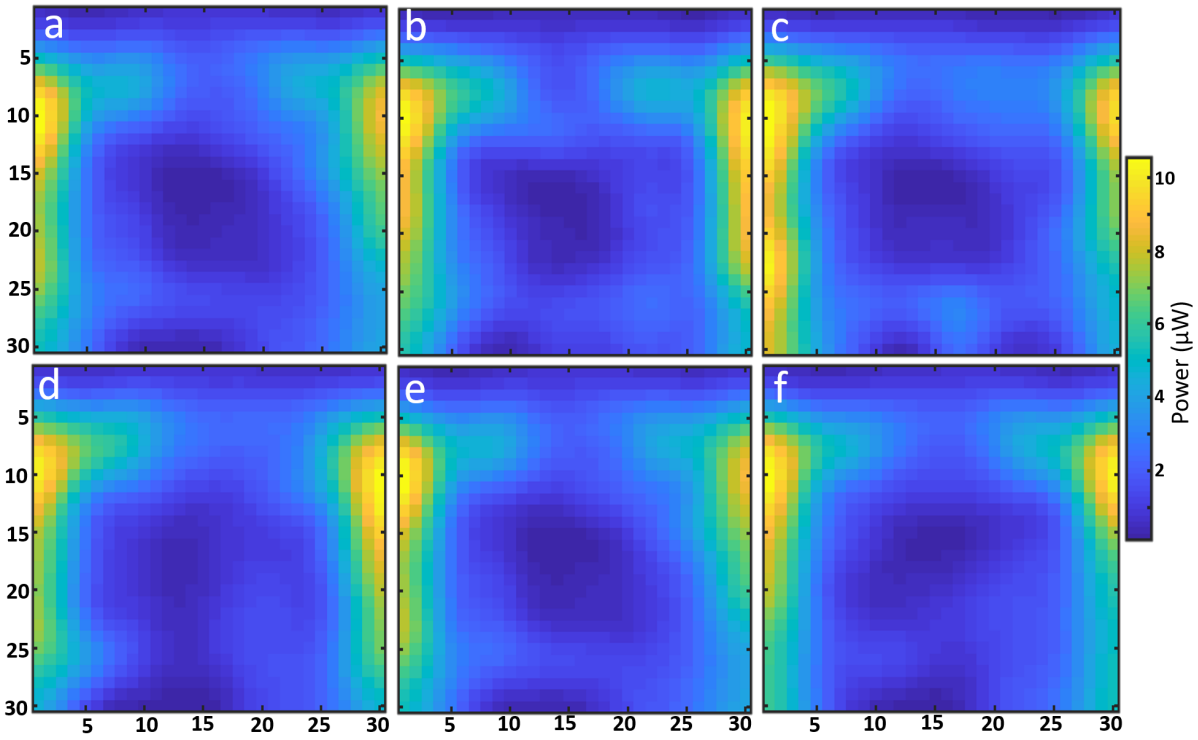

Figure 3.14: Power footprint of a 15 mm diameter tumor that positioned at (a) x=5, y=5, z=15, (b) x=0, y=0, z=15, and (c) x=20,y=10, z=15. The measured power of the fixed-location tumorous phantom with (d) a 10 mm diameter tumor, (e) a 15 mm diameter tumor, and (f) a 20 mm diameter tumor.

Table 3.1: Classification Report for CNN Algorithm

	Precision (%)	Recall (%)	F1 Scores (%)	Support (#)
Healthy	0.75	1.00	0.86	6
Unhealthy	1.00	1.00	1.00	7
Location1	0.71	1.00	0.83	42
Location2	1.00	0.57	0.73	40
Location3	1.00	1.00	1.00	47
Location4	1.00	1.00	1.00	51
Location1, 5mm	1.00	0.43	0.60	7
Location1, 7.5mm	1.00	1.00	1.00	4
Location1, 10mm	0.40	0.67	0.50	6
Location2, 5mm	1.00	1.00	1.00	4
Location2, 7.5mm	0.50	0.25	0.33	4
Location2, 10mm	0.62	0.71	0.67	7
Location3, 5mm	1.00	1.00	1.00	8
Location3, 7.5mm	0.36	1.00	0.53	4
Location3, 10mm	1.00	1.00	1.00	4
Location4, 5mm	0.50	0.40	0.44	5
Location4, 7.5mm	1.00	0.18	0.31	11
Location4, 10mm	0.38	0.89	0.53	9

Chapter 4

Flexible Metasurface system for Breast Cancer Detection

4.1 Introduction

Several applications require placing the antenna on a non-flat surface and/or integrating the antenna in the device profile. This is more desired in biomedical applications that necessitate utilizing body-worn antennas. Several recently proposed microwave breast cancer detection studies have introduced flexible and wearable antenna for breast cancer screening. Bahrami et al. [167] proposed the first wearable antenna array system that consists of 16 antenna that can be worn directly on the breast. Santorelli et al. [168] later introduced a flexible multilayer circuit board that has 16 embedded antenna for breast cancer imaging and monitoring. Both studies conducted the experimental part using a breast phantom to detect tumor presence inside the breast phantom. Porter et al. [61] subsequently developed a wearable-clinical prototype system for extended health monitoring for breast cancer. The antenna array was integrated in a single side of a bra, allowing a compact interface with patients while conducting the measurements.

The wearable/flexible antenna array for breast cancer has less system complexity, greater cost efficiency, and higher portability. However, the size of the breast surface requires the design of a smaller antenna footprint in order to integrate more antenna into the array. This is considered as the main constraint in the low frequency spectrum since the antenna size is comparable to the wavelength, which means large antenna dimensions. This can be solved by designing an ultra-wideband antenna in a trade-off with the antenna performance when used as a conformal antenna [169]. Moreover, conventional antennas are

limited to certain antenna designs, such as patch, monopole, and dipole, thus the radiation pattern is also limited. Regardless of the limitations in electrically-small antennas, they can provide an alternative solution when size is the most critical factor.

In this chapter, a flexible-conformal metasurface is utilized as a breast cancer detection modality. The proposed technique is based on illuminating the breast by a metasurface antenna and receiving the scattered wave power using electrically small metasurface cells. The receiver is expected to provide an electromagnetic energy pattern instead of an image that maps the breast's internal tissue profile. Different energy patterns can be obtained for healthy and cancerous breasts. By using a metasurface, the antenna number-penetration-resolution trade-off that limits the capability of conventional MWI techniques can be avoided. In addition, the necessity for antenna miniaturization to enhance the resolution can be avoided by the requirement of just a few scanning steps of the metasurface sheet.

4.2 Designing the Flexible Metasurface Transmitter and Receiver

The building block of the metasurface transmitter and receiver is a unit cell that is comprised of two split ring resonators positioned face to face to form an ELC resonator, as shown in Fig. 4.1(a). The unit cell is shaped from copper that has a thickness of 35 μm on a flexible dielectric Rogers RT 6002 substrate that has a 2.54 mm thickness, 2.94 dielectric constant, and a 0.0012 loss tangent. The back of the substrate is covered by a metallic ground plane to shield the unit cell from external interference. A via that connects the top of the unit cell to the ground plane was designed to act as a path to pass the signal to the top radiators (ELC) in the case of the transmitter, and to act as a path for the current to flow from the ELC to the load when the metasurface is utilized as a receiver, as illustrated in Fig. 4.1(b).

With the aim of investigating the behavior of the unit cell, the full-wave electromagnetic simulation software CST Microwave Studio was utilized [129]. The dimensions of the unit cell and the spacing between the adjacent unit cells were optimized to reach the highest reflection coefficient/absorption for the transmitter/receivers when the impedance value of the feeding port/resistive load for the transmitter/receiver is 50 Ω. Such an approach can avoid the need for a matching circuit for the transmitter and receivers, hence greater simplicity can be introduced into the system structure. During the optimization process, the location of the via is another critical factor that plays a significant role in

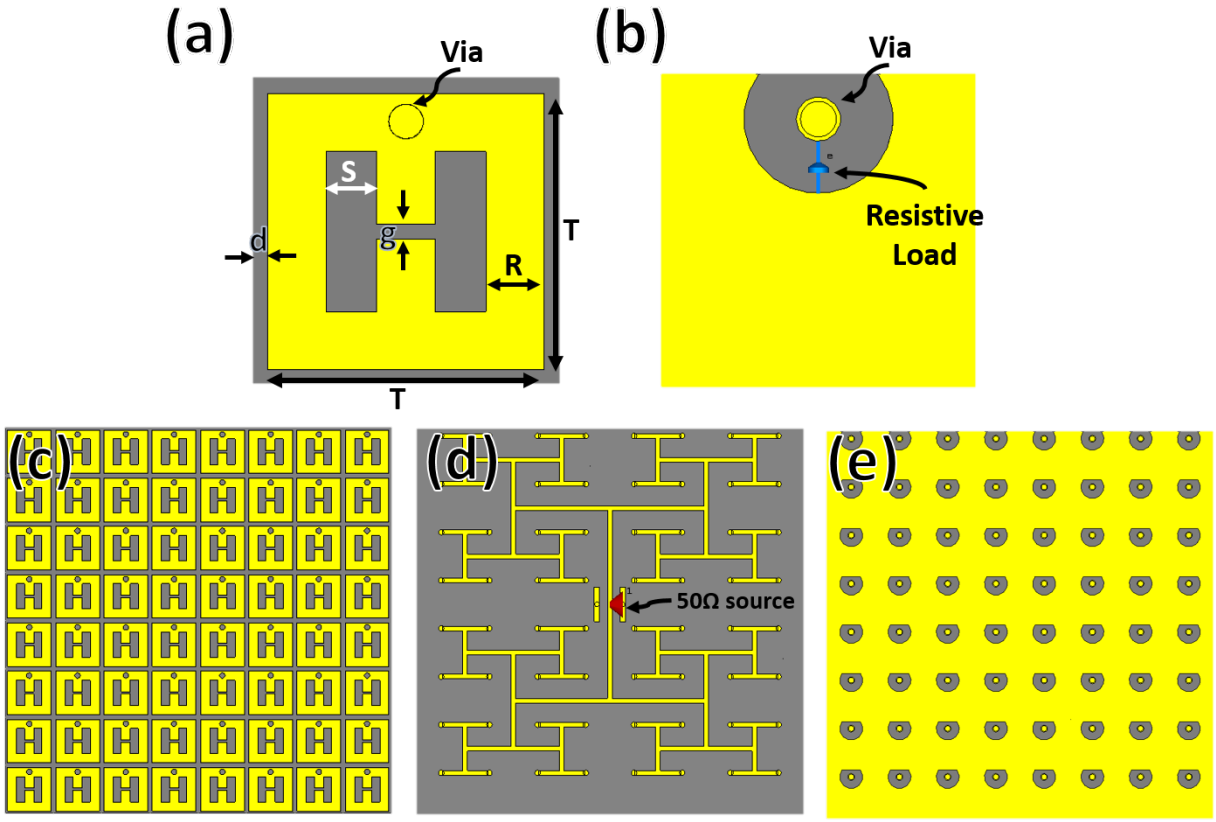

Figure 4.1: Schematic showing the proposed metasurface: (a) top view of the designed unit cell and the geometry of the ELC, (b) back view of the unit cell, (c) front view of the transmitter/receiver, (d) back view of the transmitter shows the feeding network, and (e) back view of the receiver.

maximizing the ELC power radiation/absorption by delivering the power from/to the signal source/terminated load. In order to simulate an infinite periodic structure, the boundary conditions should be applied in such a way that the magnetic and electric field are parallel to the surface of the unit cell. This can be achieved by placing the unit cell inside a waveguide that has a perfect magnetic wall in the y-z plane, a perfect electrical wall in the x-z plane, and an open ends at the z-axis to host the excitation ports. The length and width of the ELC strip is T=10 and R= 2 mm, respectively, the distance between the cells is d= 0.5 mm, the gap of the resonator is g=0.5 mm, and the distance between the strips is S=1.75 mm, as seen in Fig. 4.1(a).

The unit cells were arranged in an 8x8 periodic structure to form the metasurface transmitter/receiver film, as illustrated in Fig. 4.1(c). Since the separation distance between the unit cells is small, to the degree that it cannot host the feeding network, a second Rogers RT 6002 substrate (0.508 mm thick) was inserted at the top of the ground plane. The presence of the second substrate allows the building of a feeding network for the transmitter that can be supplied by a single feeding source, as shown in Fig. 4.1(d). In the receiver, since the power should be individually recorded in each unit cell, the second ground plane is shaped in such a way to separate the vias from the ground plane and to allow connecting each via to the ground plane through a resistive load, as seen in Fig. 4.1(e). The multiple-layer design of the developed metasurface transmitter and receiver is illustrated in Fig. 4.2. A second substrate was introduced into the receiver design to achieve accurate antenna reciprocity between the transmitter and the receiver.

The transmitter and receiver were bent cylindrically by a radius of about 42 mm (breast radius in addition to skin thickness), as seen in Fig. 4.3(a). The transmitter was supplied by a discrete port that has a 50 Ω impedance while, at the receiving side, each unit cell of the metasurface was terminated by a resistive load of 50 Ω to act as a pixel sheet to individually capture the electromagnetic energy. The measured reflection coefficient and the power across the resistive load at the resonance frequency is shown in Fig. 4.3(b). The radiation pattern and the gain of the transmitter can be seen in Fig. 4.3(c).

It should be mentioned that Rogers RT 6002 is a highly bendable material thus, when it is utilized as a substrate, metasurface film exhibits high flexibility. This flexibility allows the developed metasurface array to be utilized as a wearable transmitter or receiver. Therefore, such a design can be integrated into a bra-like setup or fixed inside a bowl-like container. This provides a less complex and compress-free system for breast cancer detection.

4.3 Numerical validation

4.3.1 Breast phantom design

The breast models were designed using methods similar to those reported in Chapter 2 and Chapter 3. Realistic breast tissue, including the skin, as well as fibroglandular and fatty tissue that is available in CST, are utilized to form an extremely dense breast. The breast has a cylindrical shape with a radius of 40 mm and an approximate length of 100 mm (the extent from the chest to the base of the nipple). The breast is covered by 2mm thick skin, while the internal breast tissue is comprised of fibroglandular and fat tissue with 75% and

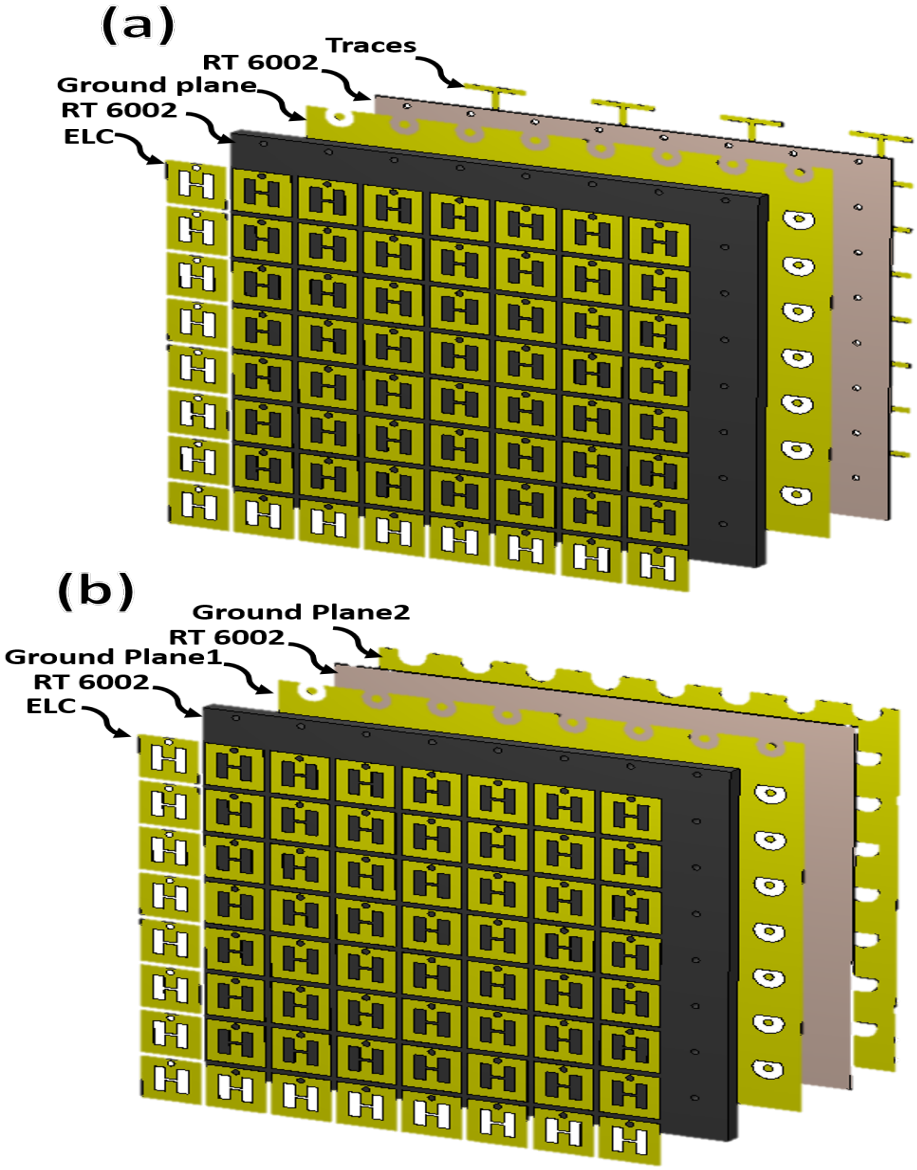

Figure 4.2: An extended view of the designed flexible metasurface (a) transmitter, and (b) receiver. The diagram shows the layer stacking order that has resonators (ELCs), Rogers RT6002 substrate, ground plane, another Rogers RT6002 as a second substrate, and the feeding network for the transmitter or the second ground plane for the receiver.

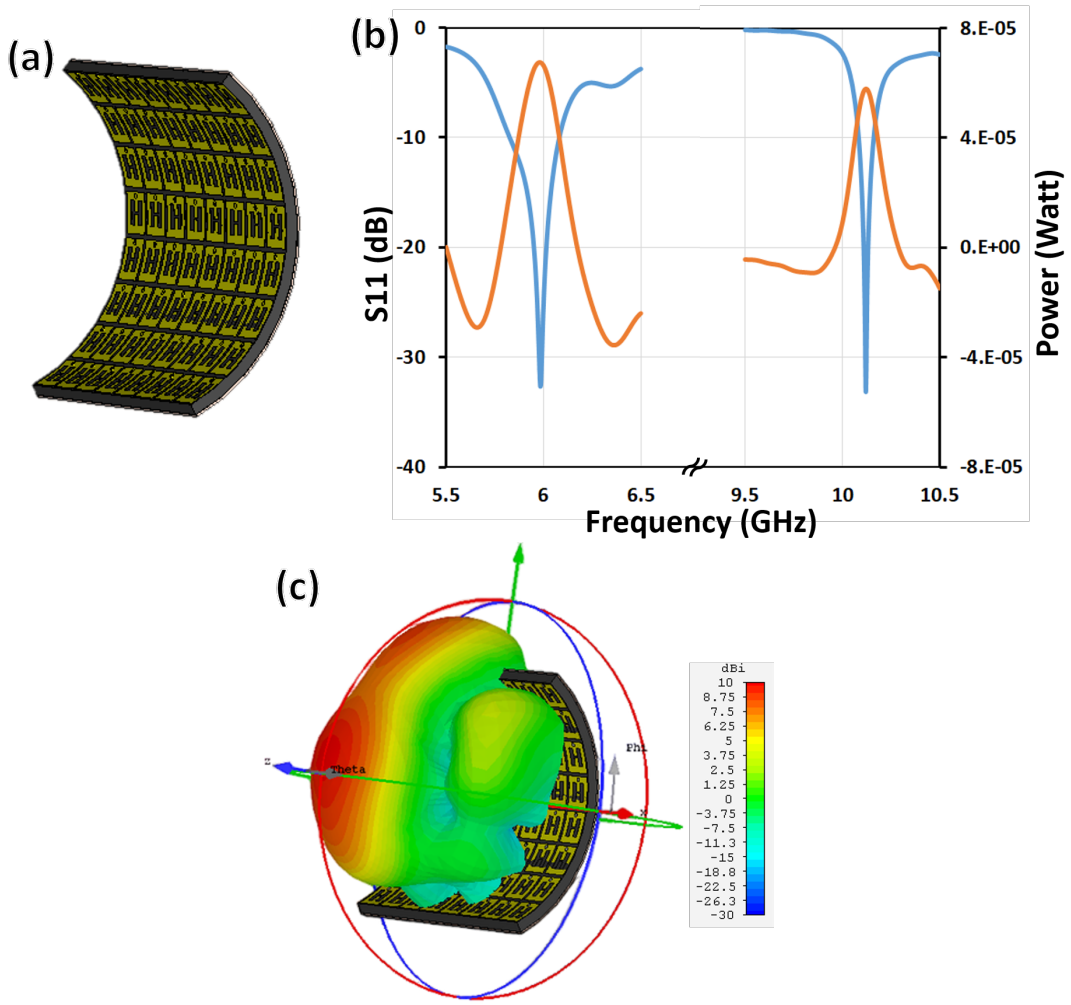

Figure 4.3: (a) Schematic of the conformal metasurface transmitter and receiver. (b) The reflection coefficient and the power across one of the terminated loads at the resonance frequency. (c) The radiation pattern and the gain of the transmitter.

25% of breast volume, respectively, as shown in Fig. 4.4. The electrical properties were determined for each breast tissue over a frequency of operation based on the measurement of electrical properties of real human breast tissue provided by IFAC-CNR [130]. When the resonance frequency of the transmitter and receiver is 10.16 GHz, based on the IFAC-CNR, the relative permittivity and electrical conductivity of the fibroglandular tissue are

45 and 12.4 S/m, respectively, and 33.3 and 9.1 S/m, respectively, for the skin, while the fat has a relative permittivity of about 3.86 and electrical conductivity of about 0.75 S/m. Toward implementing low contrast between the cancerous tissue and the surrounding tissue (fibroglandular), the cancerous tissue was assigned 95 and 24 S/m for the relative permittivity and conductivity, respectively, which represents a 2:1 difference, as applied in [135].

4.3.2 Cancerous tissue detection

Toward investigating the capability of the proposed modality, the conformal metasurface transmitter and receiver were placed (in opposite directions) on a realistic breast phantom model, as illustrated in Fig. 4.5(a) and (b). Aiming to investigate the feasibility of the proposed flexible system to detect tumor presence inside extremely dense breasts, two identical extremely dense breast phantoms were designed. With the objective to differentiate between healthy and malignant breasts, a a 5 mm radius cancerous tumor was implanted inside one of the breast phantoms, as shown in Fig. 4.6(a) and (b). The metasurface transmitter illuminated the breast with microwave radiation at 10.16 GHz.

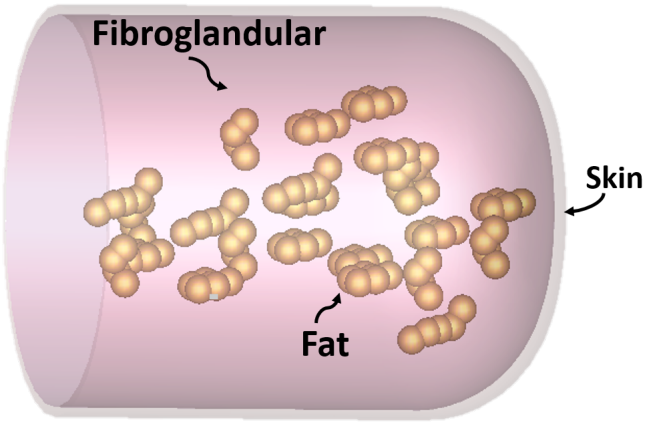

Figure 4.4: The designed extremely dense breast model.

Based on the designed metasurface, the maximum image resolution that can be achieved is 64 power readings (image pixels). In some cases, this level of spatial resolution is not sufficient to provide a clear view for the final appearance of the image. However, unlike the long scan process in single transmitter/receiver imaging techniques, the metasurface can be scanned in only a few steps to provide a higher resolution in a shorter scanning

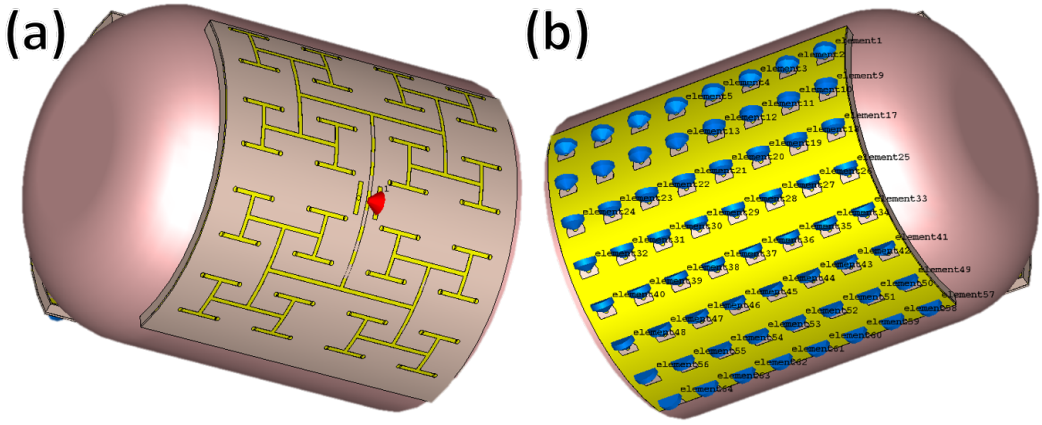

Figure 4.5: The numerical setup shows (c) the conformal transmitter and (d) the receiver on the breast model.

time. The resolution enhancement in this work was conducted by scanning (rotating and shifting) the metasurface sheets (the transmitter and receiver) over the breast by a fraction of the unit cell length. The scan was performed by changing the position of the conformal metasurface films in and around the x-axis. Three scanning steps were first applied to rotate the metasurface films around the x axis by 3.3 mm for each scan step, which is equal to one-third of the unit cell length. The sheet was then moved in the x-direction by 3.3 mm, followed by rotating around the x-axis by three steps, with similar step size and numbers as the first movement (i.e., three scanning steps with 3.3 mm step size for each). Subsequently, the metasurface sheets were moved in the x-direction by another 3.3 mm, and the three steps were then repeated in the x-direction, as illustrated in Fig. 4.7.

Implementing the nine scanning steps, the resolution can be elevated three times compared to a non-scanned situation, and the imaging pixel can be increased to 24x24 pixels. The critical achievement here is resolution enhancement, while the size of the unit cell is maintained. Therefore, the desired unit cell size and frequency of operation can be gathered with no need for miniaturizing procedures. It should be emphasized that, although a higher resolution can be obtained by increasing the number of scanning steps, only a few steps are sufficient to overcome the time-consuming scanning challenge present in other modalities and to prove the feasibility of the proposed modality in breast screening.

After each radiation session step, the transmitted wave energy through the breast reached the metasurface receiver where the generated surface current at the ELC flowed through the vias toward the resistive loads of each unit cell. The consumed power at the resistive loads was measured individually and post processed using Matlab to construct

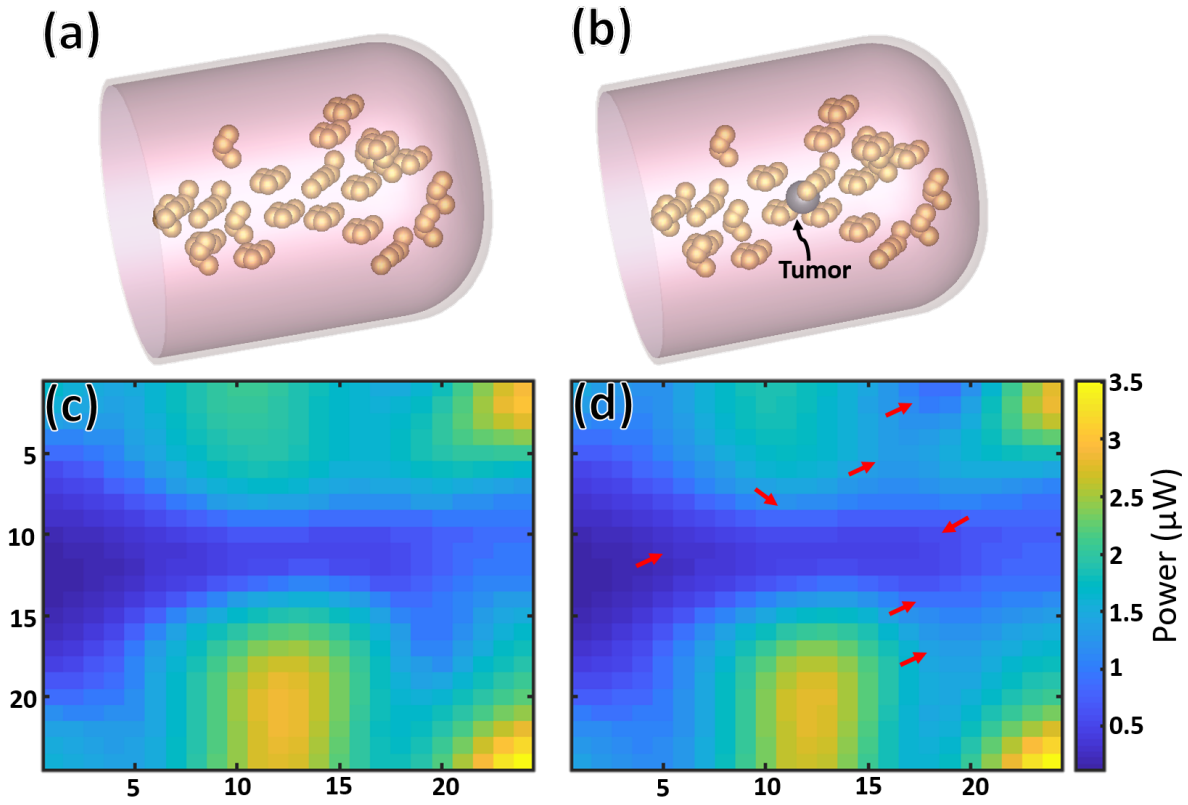

Figure 4.6: Extremely dense breast models (a) without a tumor and (b) with a tumor. The measured power pattern on the metasurface receiver for a breast (b) without a tumor and (d) with a tumor. The red arrows indicate the location of some difference compared to (c)

the received energy pattern for each breast, as seen in Fig. 4.6(c) and (d). The obtained energy expressions of the healthy breast and the breast with cancerous tissue are different, which is a result of the different internal content of each breast. The presence of the tumor affects the wave propagation through the breast, hence changes the transmitted wave that hits the metasurface receiver. Several techniques were used utilizing Matlab to enhance distinguishing of the differences between the images of this chapter(i.e., Figs. 4.6, 4.8, 4.9, and 4.10). The results are included in Appendix B

The location of a 5 mm tumor was altered inside the breast to investigate the effects that may occur on the energy pattern. The distance between the cancerous tumor and

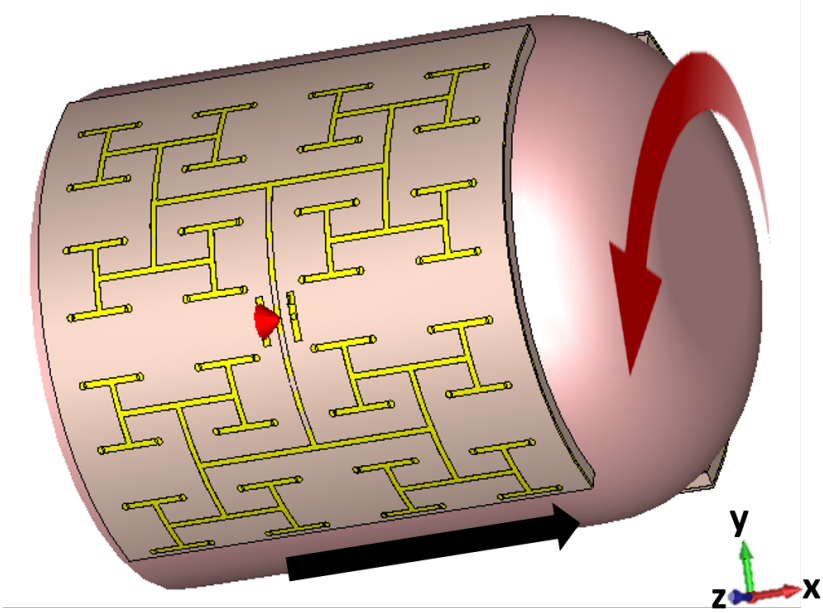

Figure 4.7: The scanning process of the conformal metasurface films. The red arrow shows the breast rotation steps around the x-axis, while the black arrow indicates the scan steps in the x-direction.

the transmitter was fixed at about 40 mm, while the tumor location was changed inside the same breast model. Three different locations were assigned to the tumor, resulting in a distinctive energy pattern that appeared on the metasurface receiver for each tumor position, as seen in Fig 4.8 (a), (b) and (c). This can be attributed to the different tumor presence inside the breast, which affects the propagation of the electromagnetic wave inside the breast, hence different electromagnetic energy reached the receiver.

Similarly, the distance between the tumor and the receiver (i.e., the depth of the tumor inside the breast) was subjected to variation for more evaluation for the proposed modality capability. As shown in Fig. 4.9 , the change in the tumor depth inside the breast influenced the received electromagnetic energy, although the tumor depth was changed slightly by about 10 mm for each detection run.

With a view to investigating the capability of the system in order to distinguish between different tumor sizes, three tumor sizes were inserted inside three identical breast models. The tumor location and depth were fixed for all tumors. The measured power pattern can be seen in Fig. 4.10, where the change in the power pattern of the 3 mm radius tumor

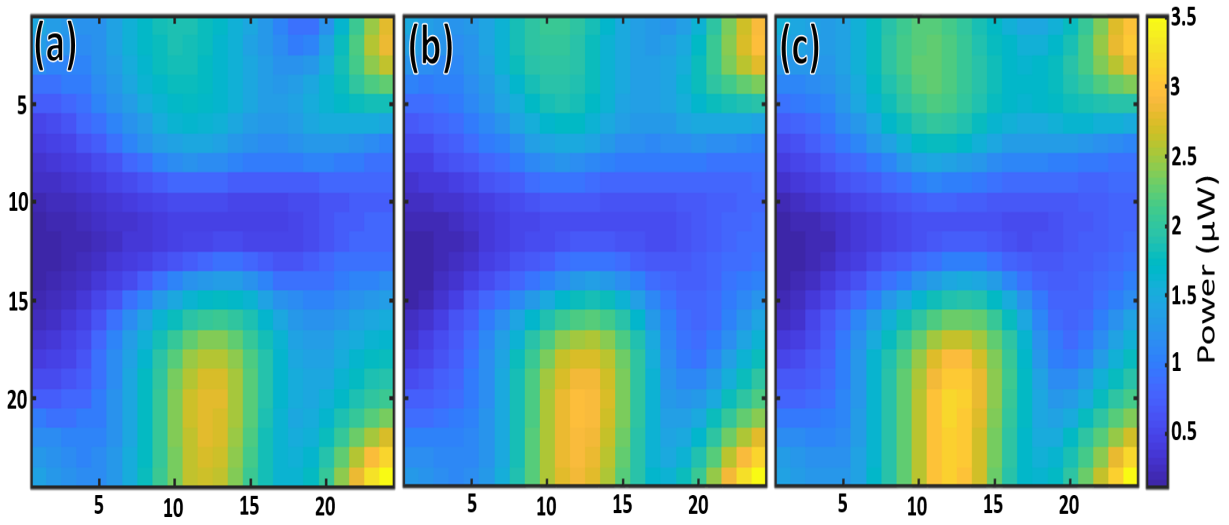

Figure 4.8: The recorded power of different tumor locations inside the breast. Assuming the center of the breast model is the origin point, the tumor is located at (a) x=0, y=0, z=0, (b) x=-20, y=5, z=5, and (c) x=10, y=5, z=-5.

shows no difference when comparing Fig. 4.10 (e) to the breast without a tumor, as shown in Fig. 4.6(c), while the tumors with radii of 5 mm, 7.5 mm, and 10 mm have different impressions, as shown in Fig. 4.10 (f), (g), (h). It can be concluded that, detecting a tumor inside the breast faces challenges when the tumor size is smaller and located deeper inside the breast. However, the flexibility of the proposed system allows rotating the metasurface around the breast to conduct the measurement from different sides and locations, which can overcome such a constraint.

4.4 Conclusion

A conformal-flexible metasurface array for breast cancer detection has been introduced. The proposed system provides an impression of the electromagnetic energy that offers valuable data for identifying the presence of an anomaly inside the breast. Engaging the metasurface in the transmitter and receiver sides provides a solution to the limitation in the resolution and penetration capability of traditional MWI. The proposed technique shows a high capability to detect a 5 mm radius cancerous tissue inside dense breast tissue.

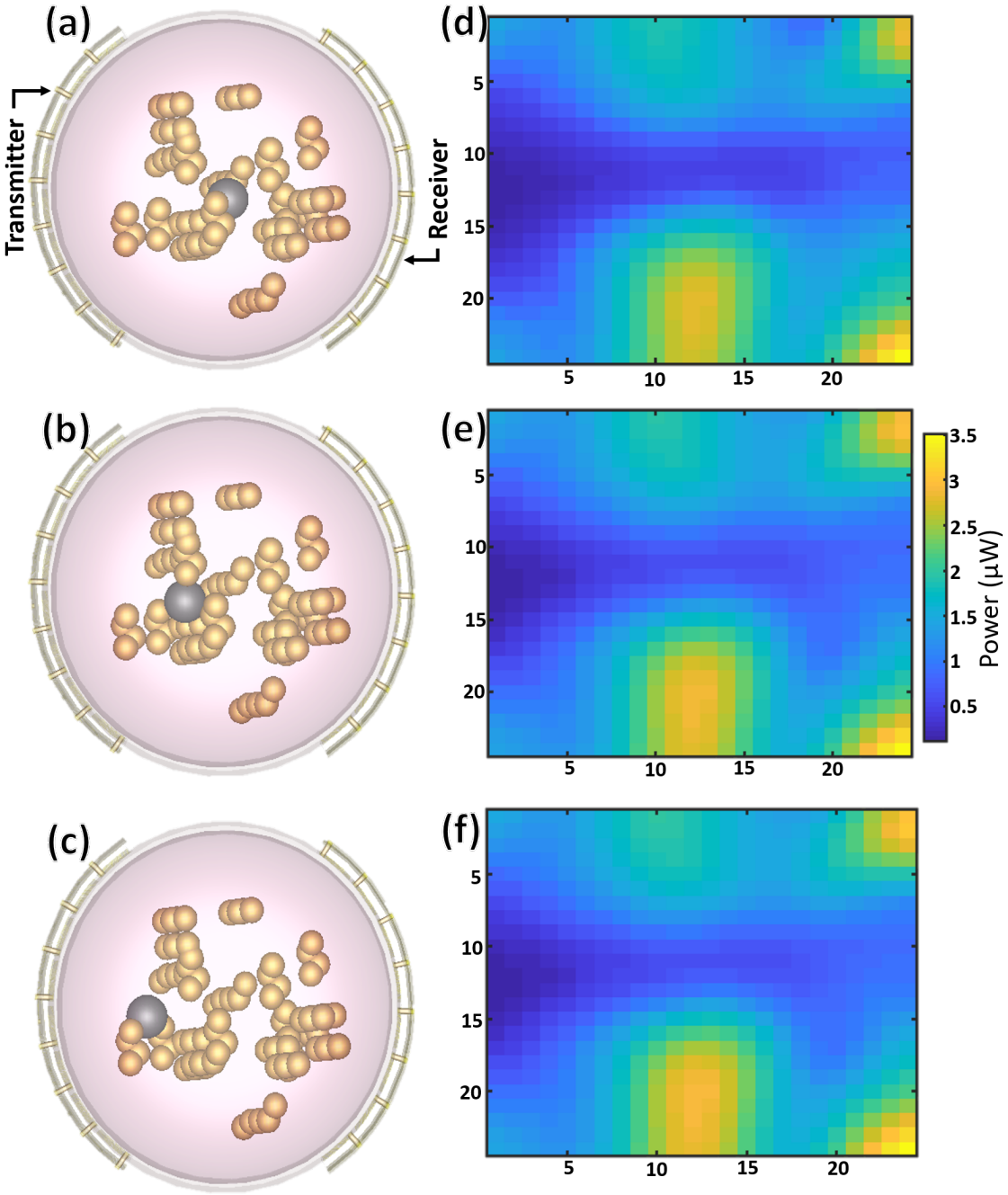

Figure 4.9: The difference in the power impression due to the change in tumor distance from the receiver. (a) 40 mm, (b) 50 mm, and (c) 60 mm from the receiver.

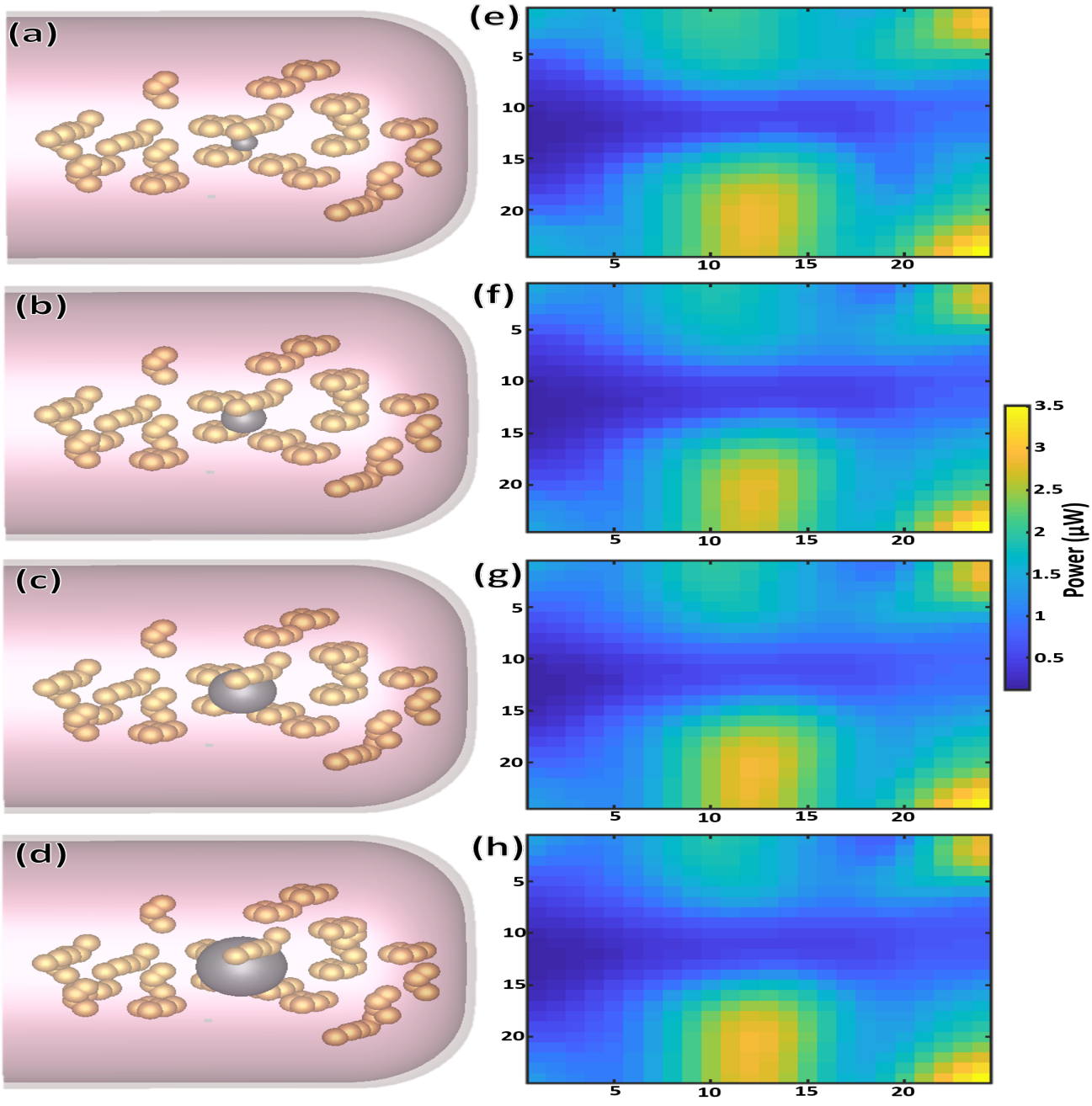

Figure 4.10: Different tumor size radii of (a) 3 mm, (b) 5 mm, (c) 7.5 mm, and (d) 10 mm, and the related resultant power impression are shown in (e), (f), (g), and (h), respectively.

Chapter 5

Accomplished and Future Work

5.1 Accomplished Work

The accomplished contributions of this dissertation can be summarized in the following list:

1. Introduction of a new microwave-thermography hybrid technique for breast cancer detection that incorporates two different detection systems and implements a different detection approach. **(Chapter 1)**

2. Determination of the capability of the introduced technique to detect early stage cancerous tumors in extremely dense breasts. **(Chapter 1)**

3. Development of a new fundamental concept for breast cancer detection based on using heat patterns of the transmitted wave power to extract valuable detection-related data. **(Chapter 1)**

4. Achievement of a high detection accuracy and extraction of valuable quantitative data from heat and energy impression images of cancerous tumors by involving machine learning for imaging classification. **(Chapter 1 & 2)**

5. Extension of the study range to include asymmetry in female breasts in order to elevate the capabilities of the proposed techniques and to prepare the systems for more practical detection scenarios. **(Chapter 1 & 2)**

6. Proposal of a new breast cancer detection system using metasurfaces as the imaging medium in a very near field. **(Chapter 2)**

7. Presentation of a new detection principle for breast cancer established on utilizing the absorbed transmitted electromagnetic energy to reconstruct energy patterns for use as detection indicators. **(Chapter 2)**

8. Introduction to the implementation of a metasurface film as an image sensor pixel array in the microwave regime for biomedical imaging. **(Chapters 2 & 3)**

9. Development of a flexible metasurface film system as a wearable breast cancer detection system. **(Chapter 3)**

10. Completion of a comprehensive investigation that shows the feasibility of the developed wearable system in detecting the presence of an anomaly inside the breast and differentiating between different tumor locations and sizes. **(Chapter 3)**

11. Provision of a solution to the antenna number-penetration-resolution trade-off issue that exists in conventional MWI. **(Chapter 3)**

5.2 List of Publications

1. Dawood Alsaedi, Alexander Melnikov, Khalid Muzaffar, Andreas Mandelis, and Omar M Ramahi."A Microwave-Thermography Hybrid Technique for Breast Cancer Detection," *IEEE Journal of Electromagnetics, RF and Microwaves in Medicine and Biology*, 2021. doi: 10.1109/JERM.2021.3072451. **(Published)**

2. Dawood Alsaedi, and Omar M Ramahi. "A Microwave-Thermography Hybrid Technique for Breast Cancer Detection," *US Provisional Patent*, April 2021. **(Patented)**

3. Dawood Alsaediand, Mohamed El Badawe, and Omar M Ramahi."A Breast Cancer Detection System using Metasurfaces with Convolution Neural Network: A Feasibility Study," *IEEE Transactions on Medical Imaging*, 2021. **(Submitted)**

4. Dawood Alsaedi, Mohamed El Badawe, and Omar M Ramahi."A Metasurface for Biomedical Imaging Applications," *2021 IEEE International Symposium on Antennas and Propagation and North American Radio Science Meeting*, 2021. **(Submitted)**

5. Dawood Alsaedi, Mohamed El Badawe, and Omar M Ramahi."A Microwave-Thermography-Convolution Neural Network Technique for Breast Cancer Detection," *2021 IEEE International Symposium on Antennas and Propagation and North American Radio Science Meeting*, 2021. **(Submitted)**

6. Dawood Alsaedi, Alexander Melnikov, Khalid Muzaffar, Andreas Mandelis, and Omar M Ramahi."A Microwave Thermography Technique for Breast Cancer Detection," *2020 IEEE International Symposium on Antennas and Propagation and North American Radio Science Meeting*, 2020. **(Accepted)**

5.3 Future Work

The future work plan is determined with the aim to improve the proposed techniques by working on the following points:

1. **Develop** the flexible metasurface system to have a transmitter that is capable of steering the beam by individually shifting the phase of the radiators. Such an improvement can enhance the radiation directionality of the transmitter, which may result in higher resolution and higher detection accuracy, as shown in Fig 5.1.

2. **Improve** the measurement process of the flexible metasurface technique by building an electronic switching system that electronically records the absorbed individual energy of each unit cell of the metasurface receiver, as illustrated in Fig 5.2.

3. **Integrate** the flexible metasurface system in a bra-like configuration to enhance the simplicity of the examination procedures and to push the system toward use as a home health monitoring device.

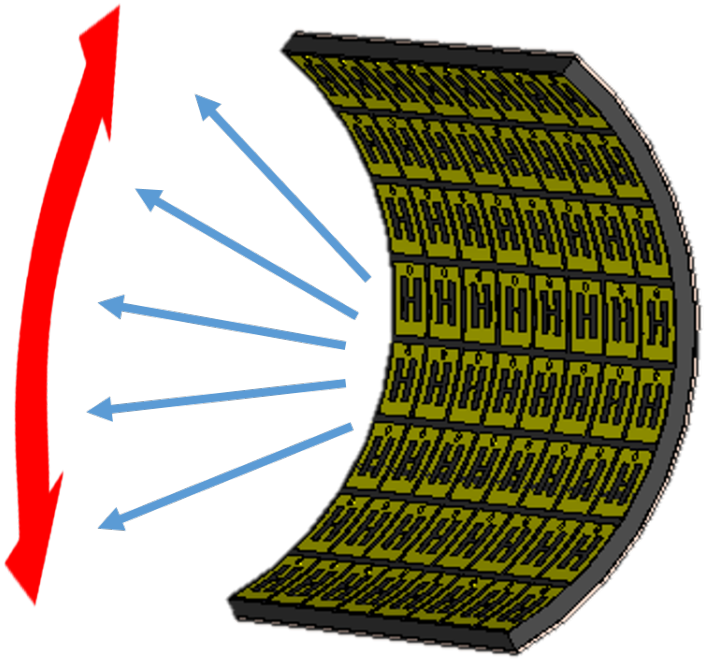

Figure 5.1: Schematic of radiation steering in the conformal metasurface transmitter.

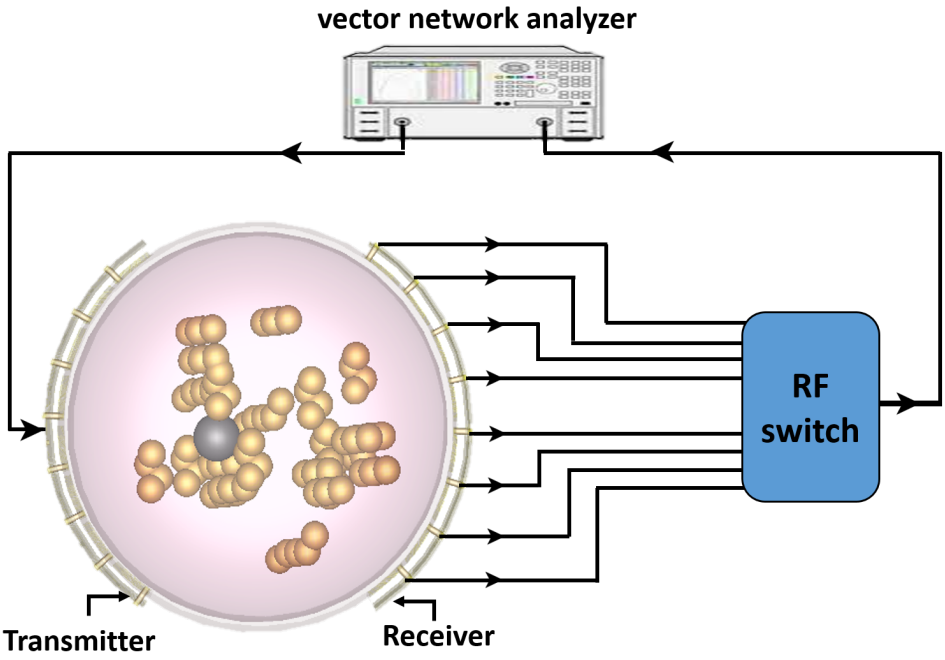

Figure 5.2: Diagram of the future work plan to improve the measurement process using an RF switch to automate the switching between the receiver unit cells.

References

[1] World Health Organization, "Breast cancer," 2021. [Online]. Available: https://www.who.int/news-room/fact-sheets/detail/breast-cancer. [Last accessed 17 May 2021].

[2] Canadian Cancer Society, "Canadian Cancer Statistics 2020, available at: https://www.cancer.ca/en/cancer-information/cancer-type/breast/statistics/?region=on," 2020.

[3] American Cancer Society, "Cancer Facts & Figures, 2021, available at: https://www.cancer.org/content/dam/cancer-org/research/cancer-facts-and-statistics/annual-cancer-facts-and-figures/2021/cancer-facts-and-figures-2021.pdf.," 2021.

[4] B. J. Mohammed, *Design and Implementation of Microwave Imaging Systems for Medical Applications*. PhD thesis, The University of Queensland, 2014.

[5] B. C. M. Morrow, R. Schmidt and C. Hasset, "Preoperative Evaluation of Abnormal Mammographic Findings to Avoid Unnecessary Breast Biopsies," *Arch. Surg.*, vol. 129, no. 1, pp. 1091–1096, 1994.

[6] P. Hoekstra, "Quantitive digital thermology: 21st century imaging systems," (Hamilton, Canada), OAND Conference, Aug. 2010.

[7] D. A. Kennedy, T. Lee, and D. Seely, "A Comparative Review of Thermography as a Breast Cancer Screening Technique," *Integrative Cancer Therapies*, vol. 8, no. 1, pp. 9–16, 2009.

[8] M. T. Ghasr, M. A. Abou-Khousa, S. Kharkovsky, R. Zoughi, and D. Pommerenke, "Portable real-time microwave camera at 24 GHz," *IEEE Transactions on Antennas and Propagation*, 2012.

[9] J. C. Newell, D. Isaacson, and J. L. Mueller, "Special issue on electrical impedance imaging," *IEEE Transactions on Medical Imaging*, vol. 21, no. 6, pp. 553–554, 2002.

[10] A. P. Smith, P. a. Hall, and D. M. Marcello, "Emerging technologies in breast cancer detection.," *Radiology management*, vol. 26, no. M, pp. 16–24; quiz 25–7, 2005.

[11] W. A. Berg, J. D. Blume, J. B. Cormack, B. Ellen, D. Lehrer, M. Böhm-vélez, E. D. Pisano, R. A. Jong, W. P. Evans, M. J. Morton, M. C. Mahoney, L. H. Larsen, R. G. Barr, and D. M. Farria, "Combined Screening with Ultrasound and Mammography Compared to Mammography Alone in Women at Elevated Risk of Breast Cancer : Results of the First-Year Screen in ACRIN 6666," *Jama*, vol. 299, no. 18, pp. 2151–2163, 2009.

[12] A. J. Surowiec, S. S. Stuchly, J. R. Barr, and A. Swarup, "Dielectric Properties of Breast Carcinoma and the Surrounding Tissues," *IEEE Transactions on Biomedical Engineering*, vol. 35, no. 4, pp. 257–263, 1988.

[13] T. Henriksson, N. Joachimowicz, C. Conessa, and J.-c. Bolomey, "Quantitative microwave imaging for breast cancer detection using a planar 2.45 GHz system," *IEEE Trans. Instrum. Meas.*, vol. 59, no. 10, pp. 2691–2699, 2010.

[14] M. Lazebnik *et al.*, "A large-scale study of the ultrawideband microwave dielectric properties of normal, benign and malignant breast tissues obtained from cancer surgeries," *Physics in Medicine & Biology*, vol. 52, no. 20, pp. 6093–6115, 2007.

[15] S. Chaudhary, R. Mishra, A. Swarup, and J. M. Thomas, "Dielectric properties of normal & malignant human breast tissues at radiowave & microwave frequencies.," *Indian Journal of Biochemistry & Biophysics*, vol. 21, pp. 76–79, 1984.

[16] A. J. Surowiec, S. S. Stuchly, J. R. Barr, and A. Swarup, "Dielectric properties of breast carcinoma and the surrounding tissues," *IEEE Transactions on Biomedical Engineering*, vol. 35, no. 4, pp. 257–263, 1988.

[17] A. Martellosio, M. Pasian, M. Bozzi, L. Perregrini, A. Mazzanti, F. Svelto, P. E. Summers, G. Renne, L. Preda, and M. Bellomi, "Dielectric properties characterization from 0.5 to 50 ghz of breast cancer tissues," *IEEE Transactions on Microwave Theory and Techniques*, vol. 65, no. 3, pp. 998–1011, 2016.

[18] P. E. Summers, A. Vingiani, S. Di Pietro, A. Martellosio, P. F. Espin-Lopez, S. Di Meo, M. Pasian, M. Ghitti, M. Mangiacotti, R. Sacchi, *et al.*, "Towards mm-wave spectroscopy for dielectric characterization of breast surgical margins," *The Breast*, vol. 45, pp. 64–69, 2019.

[19] E. C. Fear, S. C. Hagness, P. M. Meaney, M. Okoniewski, and M. A. Stuchly, "Enhancing breast tumor detection with near-field imaging," *IEEE Microwave Magazine*, vol. 3, no. 1, pp. 48–56, 2002.

[20] M. A. Aldhaeebi, K. Alzoubi, T. S. Almoneef, S. M. Bamatraf, H. Attia, and O. M. Ramahi, "Review of microwaves techniques for breast cancer detection," *Sensors*, vol. 20, no. 2390, 2020.

[21] T. M. Grzegorczyk *et al.*, "Fast 3-d tomographic microwave imaging for breast cancer detection," *IEEE Transactions on Medical Imaging*, vol. 31, no. 8, pp. 1584–1592, 2012.

[22] J. M. Felicio, J. M. Bioucas-Dias, J. R. Costa, and C. A. Fernandes, "Microwave breast imaging using a dry setup," *IEEE Transactions on Computational Imaging*, vol. 6, pp. 167–180, 2019.

[23] Y. Mohtashami, N. Behdad, and S. C. Hagness, "Toward flexible microwave ablation antennas with a balun-free helical dipole design," *IEEE Transactions on Antennas and Propagation*, vol. 68, no. 7, pp. 5052–5060, 2020.

[24] L. M. Neira, B. D. Van Veen, and S. C. Hagness, "High-resolution microwave breast imaging using a 3-d inverse scattering algorithm with a variable-strength spatial prior constraint," *IEEE Transactions on Antennas and Propagation*, vol. 65, no. 11, pp. 6002–6014, 2017.

[25] M. D. Hossain and A. S. Mohan, "Cancer detection in highly dense breasts using coherently focused time-reversal microwave imaging," *IEEE Transactions on Computational Imaging*, vol. 3, no. 4, pp. 928–939, 2017.

[26] L. E. Larsen and J. H. Jacobi, "Medical applications of microwave imaging," tech. rep., INSTITUTE OF ELECTRICAL AND ELECTRONICS ENGINEERS INC NEW YORK, 1985.

[27] B. Bocquet, J. Van de Velde, A. Mamouni, Y. Leroy, G. Giaux, J. Delannoy, and D. Delvalee, "Microwave radiometric imaging at 3 ghz for the exploration of breast tumors," *IEEE Transactions on Microwave Theory and Techniques*, vol. 38, no. 6, pp. 791–793, 1990.

[28] S. Mouty, B. Bocquet, R. Ringot, N. Rocourt, and P. Devos, "Microwave radiometric imaging (mwi) for the characterisation of breast tumours," *The European Physical Journal Applied Physics*, vol. 10, no. 1, pp. 73–78, 2000.

[29] C. Pichot, L. Jofre, G. Peronnet, and J. Bolomey, "Active microwave imaging of inhomogeneous bodies," *IEEE transactions on antennas and propagation*, vol. 33, no. 4, pp. 416–425, 1985.

[30] P. M. Meaney, M. W. Fanning, D. Li, S. P. Poplack, and K. D. Paulsen, "A clinical prototype for active microwave imaging of the breast," *IEEE Transactions on Microwave Theory and Techniques*, vol. 48, no. 11, pp. 1841–1853, 2000.

[31] X. Wang, H. Xin, D. Bauer, and R. Witte, "Microwave induced thermal acoustic imaging modeling for potential breast cancer detection," in *2011 IEEE International Symposium on Antennas and Propagation (APSURSI)*, pp. 722–725, IEEE, 2011.

[32] J. Song, Z. Zhao, J. Wu, X. Zhu, Z. Nie, and Q.-H. Liu, "Thermo-acoustic imaging for different breast tissues in microwave induced thermo-acoustic tomography system," in *2013 IEEE Antennas and Propagation Society International Symposium (APSURSI)*, pp. 2032–2033, IEEE, 2013.

[33] K.-C. Kwon, Y.-T. Lim, C.-H. Kim, N. Kim, C. Park, K.-H. Yoo, S.-H. Son, and S.-I. Jeon, "Microwave tomography analysis system for breast tumor detection," *Journal of medical systems*, vol. 36, no. 3, pp. 1757–1767, 2012.

[34] S. Semenov, "Microwave tomography: review of the progress towards clinical applications," *Philosophical Transactions of the Royal Society A: Mathematical, Physical and Engineering Sciences*, vol. 367, no. 1900, pp. 3021–3042, 2009.

[35] P. M. Meaney, M. W. Fanning, D. Li, S. P. Poplack, and K. D. Paulsen, "A clinical prototype for active microwave imaging of the breast," *IEEE Transactions on Microwave Theory and Techniques*, vol. 48, no. 11, pp. 1841–1853, 2000.

[36] T. M. Grzegorczyk, P. M. Meaney, P. A. Kaufman, K. D. Paulsen, *et al.*, "Fast 3-d tomographic microwave imaging for breast cancer detection," *IEEE transactions on medical imaging*, vol. 31, no. 8, pp. 1584–1592, 2012.

[37] A. E. Souvorov, A. E. Bulyshev, S. Y. Semenov, R. H. Svenson, and G. P. Tatsis, "Two-dimensional computer analysis of a microwave flat antenna array for breast cancer tomography," *IEEE Transactions on Microwave Theory and Techniques*, vol. 48, no. 8, pp. 1413–1415, 2000.

[38] G. Bindu, L. Anil, T. Vinu, C. Aanandan, and K. Mathew, "Active microwave imaging for breast cancer detection," 2006.

[39] E. C. Fear, P. M. Meaney, and M. A. Stuchly, "Microwaves for breast cancer detection?," *IEEE potentials*, vol. 22, no. 1, pp. 12–18, 2003.

[40] P. M. Meaney, K. D. Paulsen, and T. P. Ryan, "Two-dimensional hybrid element image reconstruction for tm illumination," *IEEE transactions on antennas and propagation*, vol. 43, no. 3, pp. 239–247, 1995.

[41] P. M. Meaney, K. D. Paulsen, A. Hartov, and R. K. Crane, "An active microwave imaging system for reconstruction of 2-d electrical property distributions," *IEEE Transactions on Biomedical Engineering*, vol. 42, no. 10, pp. 1017–1026, 1995.

[42] P. M. Meaney, K. D. Paulsen, and J. T. Chang, "Near-field microwave imaging of biologically-based materials using a monopole transceiver system," *IEEE Transactions on Microwave Theory and Techniques*, vol. 46, no. 1, pp. 31–45, 1998.

[43] A. H. Golnabi, P. M. Meaney, and K. D. Paulsen, "Tomographic microwave imaging with incorporated prior spatial information," *IEEE Transactions on Microwave Theory and Techniques*, vol. 61, no. 5, pp. 2129–2136, 2013.

[44] A. H. Golnabi, P. M. Meaney, S. Geimer, and K. D. Paulsen, "Microwave imaging for breast cancer detection and therapy monitoring," in *2011 IEEE Topical Conference on Biomedical Wireless Technologies, Networks, and Sensing Systems*, pp. 59–62, IEEE, 2011.

[45] S. Y. Semenov, A. E. Bulyshev, A. Abubakar, V. G. Posukh, Y. E. Sizov, A. E. Souvorov, P. M. van den Berg, and T. C. Williams, "Microwave-tomographic imaging of the high dielectric-contrast objects using different image-reconstruction approaches," *IEEE transactions on Microwave Theory and Techniques*, vol. 53, no. 7, pp. 2284–2294, 2005.

[46] S.-H. Son, N. Simonov, H.-J. Kim, J.-M. Lee, and S.-I. Jeon, "Preclinical prototype development of a microwave tomography system for breast cancer detection," *ETRI journal*, vol. 32, no. 6, pp. 901–910, 2010.

[47] D. J. Pagliari, A. Pulimeno, M. Vacca, J. A. Tobon, F. Vipiana, M. R. Casu, R. Solimene, and L. P. Carloni, "A low-cost, fast, and accurate microwave imaging system for breast cancer detection," in *2015 IEEE Biomedical Circuits and Systems Conference (BioCAS)*, pp. 1–4, IEEE, 2015.

[48] S. Hosseinzadegan, A. Fhager, M. Persson, S. D. Geimer, and P. M. Meaney, "Discrete dipole approximation-based microwave tomography for fast breast cancer imaging," *IEEE Transactions on Microwave Theory and Techniques*, vol. 69, no. 5, pp. 2741–2752, 2021.

[49] S.-I. Jeon, B.-R. Kim, and S.-H. Son, "Clinical trial of microwave tomography imaging," in *2016 URSI Asia-Pacific Radio Science Conference (URSI AP-RASC)*, pp. 1–2, IEEE, 2016.

[50] S. C. Hagness, A. Taflove, and J. E. Bridges, "Three-dimensional fdtd analysis of an ultrawideband antenna-array element for confocal microwave imaging of nonpalpable breast tumors," in *IEEE Antennas and Propagation Society International Symposium. 1999 Digest. Held in conjunction with: USNC/URSI National Radio Science Meeting (Cat. No. 99CH37010)*, vol. 3, pp. 1886–1889, IEEE, 1999.

[51] S. K. Davis, X. Li, E. J. Bond, S. C. Hagness, and B. D. Van Veen, "Frequency-domain penalized least-squares beamformer design for early detection of breast cancer via microwave imaging," in *Sensor Array and Multichannel Signal Processing Workshop Proceedings, 2002*, pp. 120–124, IEEE, 2002.

[52] E. J. Bond, X. Li, S. C. Hagness, and B. D. Van Veen, "Microwave imaging via space-time beamforming for early detection of breast cancer," *IEEE Transactions on Antennas and Propagation*, vol. 51, no. 8, pp. 1690–1705, 2003.

[53] R. Nilavalan, A. Gbedemah, I. Craddock, X. Li, and S. C. Hagness, "Numerical investigation of breast tumour detection using multi-static radar," 2003.

[54] S. K. Davis, H. Tandradinata, S. C. Hagness, and B. D. Van Veen, "Ultrawideband microwave breast cancer detection: a detection-theoretic approach using the generalized likelihood ratio test," *IEEE transactions on biomedical engineering*, vol. 52, no. 7, pp. 1237–1250, 2005.

[55] E. Fear and J. Sill, "Preliminary investigations of tissue sensing adaptive radar for breast tumor detection," in *Proceedings of the 25th Annual International Conference of the IEEE Engineering in Medicine and Biology Society (IEEE Cat. No. 03CH37439)*, vol. 4, pp. 3787–3790, IEEE, 2003.

[56] E. C. Fear, J. Bourqui, C. Curtis, D. Mew, B. Docktor, and C. Romano, "Microwave breast imaging with a monostatic radar-based system: A study of application to patients," *IEEE transactions on microwave theory and techniques*, vol. 61, no. 5, pp. 2119–2128, 2013.

[57] I. Craddock, A. Preece, J. Leendertz, M. Klemm, R. Nilavalan, and R. Benjamin, "Development of a hemi-spherical wideband antenna array for breast cancer imaging," 2006.

[58] M. Klemm, I. Craddock, J. Leendertz, A. Preece, and R. Benjamin, "Breast cancer detection using symmetrical antenna array," 2007.

[59] M. Klemm, I. Craddock, J. Leendertz, A. Preece, D. Gibbins, M. Shere, and R. Benjamin, "Clinical trials of a uwb imaging radar for breast cancer," in *Proceedings of the Fourth European Conference on Antennas and Propagation*, pp. 1–4, IEEE, 2010.

[60] E. Porter, E. Kirshin, A. Santorelli, M. Coates, and M. Popović, "Time-domain multistatic radar system for microwave breast screening," *IEEE Antennas and Wireless Propagation Letters*, vol. 12, pp. 229–232, 2013.

[61] E. Porter, H. Bahrami, A. Santorelli, B. Gosselin, L. A. Rusch, and M. Popović, "A wearable microwave antenna array for time-domain breast tumor screening," *IEEE transactions on medical imaging*, vol. 35, no. 6, pp. 1501–1509, 2016.

[62] K. Muzaffar, D. Roy, S. Tuli, and S. Koul, "Frequency modulated thermal wave imaging for visualizing power density of electromagnetic waves on plane surfaces," *Research in Nondestructive Evaluation*, pp. 1–15, 2017.

[63] C. Hellier, *Handbook of Nondestructive Evaluation*. New York, NY, USA: Mcgraw-hill, 2001.

[64] A. B. Bakht, B.; Mufti, *Bridges: Analysis, Design, Structural Health Monitoring, and Rehabilitation*. Cham, Switzerland: Springer, 2015.

[65] D. L. Balageas, P. Levesque, and A. A. Deom, "Characterization of electromagnetic fields using a lock-in infrared thermographic system," in *Thermosense XV: An International Conference on Thermal Sensing and Imaging Diagnostic Applications*, vol. 1933, pp. 274–286, International Society for Optics and Photonics, 1993.

[66] N. Chiyo, M. Arai, Y. Tanaka, A. Nishikata, T. Hirano, and T. Maeno, "Measurement technique for electromagnetic field intensity distribution using infrared 2-d lock-in amplifier," in *Electrical Insulation and Dielectric Phenomena (CEIDP), 2010 Annual Report Conference on*, pp. 1–4, IEEE, 2010.

[67] K. Muzaffar, S. Tuli, and S. Koul, "Beam width estimation of microwave antennas using lock-in infrared thermography," *Infrared Physics & Technology*, vol. 72, pp. 244–248, 2015.

[68] H. Zhang, R. Yang, Y. He, A. Foudazi, L. Cheng, and G. Tian, "A review of microwave thermography nondestructive testing and evaluation," *Sensors*, vol. 17, no. 5, p. 1123, 2017.

[69] C. Ibarra-Castanedo, J. R. Tarpani, and X. P. Maldague, "Nondestructive testing with thermography," *European Journal of Physics*, vol. 34, no. 6, p. S91, 2013.

[70] R. M. Sega and J. D. Norgard, "Infrared measurements of scattering and electromagnetic penetration through apertures," *IEEE Transactions on Nuclear Science*, vol. 33, no. 6, pp. 1657–1663, 1986.

[71] *Non destructive evaluation of absorbing materials using microwave stimulated infrared thermography*, (Berlin, Germany), Springer, 1993.

[72] G. d'Ambrosio, R. Massa, M. Migliore, G. Cavaccini, A. Ciliberto, and C. Sabatino, "Microwave excitation for thermographic nde: An experimental study and some theoretical evaluations," *Materials Evaluation*, vol. 53, 4 1995.

[73] S. A. Keo, F. Brachelet, F. Breaban, and D. Defer, "Steel detection in reinforced concrete wall by microwave infrared thermography," *Ndt & E International*, vol. 62, pp. 172–177, 2014.

[74] D. WL, "A New Method of Observing Electromagnetic Fields at High Frequencies by Use of Test Paper," *Bull. Yamagata Univ.Yamagata, japan*, 1955.

[75] L. G. Gregoris *et al.*, "Thermography in microwave holography," *Applied optics*, vol. 14, no. 7, pp. 1487–1489, 1975.

[76] M. D., *Quantification of the thermographic mapping of microwave fields*. PhD thesis, University of Colorado, Colorado Springs, CO, USA, 1991.

[77] D. L. Balageas, P. Levesque, and A. A. Deom, "Characterization of electromagnetic fields using a lock-in infrared thermographic system," in *Thermosense XV: An International Conference on Thermal Sensing and Imaging Diagnostic Applications*, vol. 1933, pp. 274–286, International Society for Optics and Photonics, 1993.

[78] T. Crépin, F. Issac, D. Prost, and S. Bolioli, "Microwave electric field imaging of metamaterials using thermoemissive films," *IEEE Antennas and Propagation Magazine*, vol. 56, no. 3, pp. 37–42, 2014.

[79] S. Zouhdi, A. Sihvola, and M. Arsalane, *Advances in electromagnetics of complex media and metamaterials*, vol. 89. Springer Science & Business Media, 2012.

[80] C. L. Holloway, R. R. Delyser, R. F. German, P. McKenna, and M. Kanda, "Comparison of electromagnetic absorber used in anechoic and semi-anechoic chambers for emissions and immunity testing of digital devices," *IEEE Transactions on Electromagnetic Compatibility*, vol. 39, no. 1, pp. 33–47, 1997.

[81] D. R. Smith, W. J. Padilla, D. Vier, S. C. Nemat-Nasser, and S. Schultz, "Composite medium with simultaneously negative permeability and permittivity," *Physical review letters*, vol. 84, no. 18, p. 4184, 2000.

[82] M. Lapine and S. Tretyakov, "Contemporary notes on metamaterials," *IET microwaves, antennas & propagation*, vol. 1, no. 1, pp. 3–11, 2007.

[83] K. Achouri, M. A. Salem, and C. Caloz, "General metasurface synthesis based on susceptibility tensors," *IEEE Transactions on Antennas and Propagation*, vol. 63, no. 7, pp. 2977–2991, 2015.

[84] R. Quarfoth and D. Sievenpiper, "Artificial tensor impedance surface waveguides," *IEEE Transactions on Antennas and Propagation*, vol. 61, no. 7, pp. 3597–3606, 2013.

[85] D. Shrekenhamer, W. Xu, S. Venkatesh, D. Schurig, S. Sonkusale, and W. J. Padilla, "Experimental realization of a metamaterial detector focal plane array," *Physical review letters*, vol. 109, no. 17, p. 177401, 2012.

[86] K. B. Alici and E. Özbay, "Radiation properties of a split ring resonator and monopole composite," *Physica status solidi (b)*, vol. 244, no. 4, pp. 1192–1196, 2007.

[87] S. Enoch, G. Tayeb, P. Sabouroux, N. Guérin, and P. Vincent, "A metamaterial for directive emission," *Physical Review Letters*, vol. 89, no. 21, p. 213902, 2002.

[88] T. S. Almoneef and O. M. Ramahi, "Metamaterial electromagnetic energy harvester with near unity efficiency," *Applied Physics Letters*, vol. 106, no. 15, p. 153902, 2015.

[89] E. F. Kuester, M. A. Mohamed, M. Piket-May, and C. L. Holloway, "Averaged transition conditions for electromagnetic fields at a metafilm," *IEEE Transactions on Antennas and Propagation*, vol. 51, no. 10, pp. 2641–2651, 2003.

[90] J. B. Pendry, "Negative refraction makes a perfect lens," *Physical review letters*, vol. 85, no. 18, p. 3966, 2000.

[91] N. Fang, H. Lee, C. Sun, and X. Zhang, "Sub–diffraction-limited optical imaging with a silver superlens," *Science*, vol. 308, no. 5721, pp. 534–537, 2005.

[92] J. A. Gordon, C. L. Holloway, J. Booth, S. Kim, Y. Wang, J. Baker-Jarvis, and D. R. Novotny, "Fluid interactions with metafilms/metasurfaces for tuning, sensing, and microwave-assisted chemical processes," *Physical Review B*, vol. 83, no. 20, p. 205130, 2011.

[93] D. Schurig, J. J. Mock, B. Justice, S. A. Cummer, J. B. Pendry, A. F. Starr, and D. R. Smith, "Metamaterial electromagnetic cloak at microwave frequencies," *Science*, vol. 314, no. 5801, pp. 977–980, 2006.

[94] W. Cai, U. K. Chettiar, A. V. Kildishev, and V. M. Shalaev, "Optical cloaking with metamaterials," *Nature photonics*, vol. 1, no. 4, pp. 224–227, 2007.

[95] C. L. Holloway, E. F. Kuester, J. A. Gordon, J. O'Hara, J. Booth, and D. R. Smith, "An overview of the theory and applications of metasurfaces: The two-dimensional equivalents of metamaterials," *IEEE Antennas and Propagation Magazine*, vol. 54, no. 2, pp. 10–35, 2012.

[96] A. S. Lundervold and A. Lundervold, "An overview of deep learning in medical imaging focusing on mri," *Zeitschrift für Medizinische Physik*, vol. 29, no. 2, pp. 102–127, 2019.

[97] W. Xiong, L. Wu, F. Alleva, J. Droppo, X. Huang, and A. Stolcke, "The microsoft 2017 conversational speech recognition system," in *2018 IEEE international conference on acoustics, speech and signal processing (ICASSP)*, pp. 5934–5938, IEEE, 2018.

[98] A. v. d. Oord, S. Dieleman, H. Zen, K. Simonyan, O. Vinyals, A. Graves, N. Kalchbrenner, A. Senior, and K. Kavukcuoglu, "Wavenet: A generative model for raw audio," *arXiv preprint arXiv:1609.03499*, 2016.

[99] D. S. Kermany, M. Goldbaum, W. Cai, C. C. Valentim, H. Liang, S. L. Baxter, A. McKeown, G. Yang, X. Wu, F. Yan, *et al.*, "Identifying medical diagnoses and treatable diseases by image-based deep learning," *Cell*, vol. 172, no. 5, pp. 1122–1131, 2018.

[100] J. Jiménez Luna, M. Skalic, G. Martinez-Rosell, and G. De Fabritiis, "Kdeep: Protein-ligand absolute binding affinity prediction via 3d-convolutional neural networks," *J. Chem. Inf. Model*, vol. 58, pp. 287–296, 2018.

[101] A. Radford, K. Narasimhan, T. Salimans, and I. Sutskever, "Improving language understanding by generative pre-training," 2018.

[102] A. Krizhevsky, I. Sutskever, and G. E. Hinton, "Imagenet classification with deep convolutional neural networks," *Advances in neural information processing systems*, vol. 25, pp. 1097–1105, 2012.

[103] M. Liu, J. Zhang, E. Adeli, and D. Shen, "Landmark-based deep multi-instance learning for brain disease diagnosis," *Medical Image Analysis*, vol. 43, pp. 157–168, 2018.

[104] X. Zhou, R. Takayama, S. Wang, X. Zhou, T. Hara, and H. Fujita, "Automated segmentation of 3D anatomical structures on ct images by using a deep convolutional network based on end-to-end learning approach," in *Medical Imaging 2017: Image Processing*, vol. 10133, (Orlando,United States), p. 1013324, International Society for Optics and Photonics, 2017.

[105] J.-T. Lu, S. Pedemonte, B. Bizzo, S. Doyle, K. P. Andriole, M. H. Michalski, R. G. Gonzalez, and S. R. Pomerantz, "Deepspine: Automated lumbar vertebral segmentation, disc-level designation, and spinal stenosis grading using deep learning," in *Machine Learning for Healthcare Conference*, vol. 10133, (California, United State), pp. 403–419, Machine Learning Research, 2018.

[106] S. K. Davis, B. D. Van Veen, S. C. Hagness, and F. Kelcz, "Breast tumor characterization based on ultrawideband microwave backscatter," *IEEE transactions on biomedical engineering*, vol. 55, no. 1, pp. 237–246, 2007.

[107] B. Gerazov and R. C. Conceicao, "Deep learning for tumour classification in homogeneous breast tissue in medical microwave imaging," in *IEEE EUROCON 2017-17th International Conference on Smart Technologies*, pp. 564–569, IEEE, 2017.

[108] S. P. Rana, M. Dey, G. Tiberi, L. Sani, A. Vispa, G. Raspa, M. Duranti, M. Ghavami, and S. Dudley, "Machine learning approaches for automated lesion detection in microwave breast imaging clinical data," *Scientific reports*, vol. 9, no. 1, pp. 1–12, 2019.

[109] M. N. Sadiku, *Elements of electromagnetics*. Oxford university press, 2014.

[110] P. L. Costa, *Real-Time Visualisation of Antenna Patterns*. PhD thesis, MS thesis, Department of Electrical and Information Technology, Lund University, 2009.

[111] D. Sjöberg, "Analysis of wave propagation in stratified structures using circuit analogues, with application to electromagnetic absorbers," *European Journal of Physics*, vol. 29, no. 4, p. 721, 2008.

[112] H. Bosman, Y. Lau, and R. Gilgenbach, "Microwave absorption on a thin film," *Applied Physics Letters*, vol. 82, no. 9, pp. 1353–1355, 2003.

[113] J. D. Norgard, "Electromagnetic magnitude and phase measurements from infrared thermograms," in *Aerospace Conference, 1997. Proceedings., IEEE*, vol. 2, pp. 145–157, IEEE, 1997.

[114] D. Prost, F. Issac, and P. Reulet, "Large scale measurement of microwave electric field using infrared thermography and electromagnetic simulation," in *Progress In Electromagnetics Research Symposium Proceedings*, pp. 1021–1024, 2011.

[115] Y. Nagao, Y. Kawaguchi, Y. Sugiyama, S. Saji, and Y. Kashiki, "Relationship between mammographic density and the risk of breast cancer in japanese women: a case-control study," *Breast Cancer*, vol. 10, no. 3, pp. 228–233, 2003.

[116] H. Bahramiabarghouei, E. Porter, A. Santorelli, B. Gosselin, M. Popović, and L. A. Rusch, "Flexible 16 antenna array for microwave breast cancer detection," *IEEE Transactions on Biomedical Engineering*, vol. 62, no. 10, pp. 2516–2525, 2015.

[117] M. A. Aldhaeebi, T. S. Almoneef, H. Attia, and O. M. Ramahi, "Electrically small magnetic probe with PCA for near-field microwave breast tumors detection," *Progress In Electromagnetics Research*, vol. 84, pp. 177–186, 2019.

[118] M. A. Aldhaeebi, T. S. Almoneef, A. Ali, Z. Ren, and O. M. Ramahi, "Near field breast tumor detection using ultra-narrow band probe with machine learning techniques," *Scientific reports*, vol. 8, no. 1, pp. 1–16, 2018.

[119] M. T. Islam, M. Samsuzzaman, M. Islam, S. Kibria, M. J. Singh, *et al.*, "A homogeneous breast phantom measurement system with an improved modified microwave imaging antenna sensor," *sensors*, vol. 18, no. 9, p. 2962, 2018.

[120] M. K. Sharma *et al.*, "Experimental investigation of the breast phantom for tumor detection using ultra-wide band–mimo antenna sensor (umas) probe," *IEEE Sensors Journal*, vol. 20, no. 12, pp. 6745–6752, 2020.

[121] M. A. Aldhaeebi, T. S. Almoneef, H. Attia, and O. M. Ramahi, "Near-field microwave loop array sensor for breast tumor detection," *IEEE Sensors Journal*, vol. 19, no. 24, pp. 11867–11872, 2019.

[122] D. Prost, F. Issac, and P. Reulet, "Large scale measurement of microwave electric field using infrared thermography and electromagnetic simulation," in *Progress In*

Electromagnetics Research Symposium Proceedings, (Marrakesh, Morocco), pp. 1021–1024, 2011.

[123] E. Zastrow, S. Davis, and S. Hagness, "Safety assessment of breast cancer detection via ultrawideband microwave radar operating in swept-frequency mode," in *2006 IEEE Antennas and Propagation Society International Symposium*, (Albuquerque, United States), pp. 721–724, 2006.

[124] "Ieee recommended practice for measurements and computations of radio frequency electromagnetic fields with respect to human exposure to such fields,100 KHz-300 GHz," *IEEE Std C95.3-2002 (Revision of IEEE Std C95.3-1991)*, pp. i–126, 2002.

[125] I. C. on Non-Ionizing Radiation Protection *et al.*, "Guidelines for limiting exposure to electromagnetic fields (100 khz to 300 ghz)," *Health physics*, vol. 118, no. 5, pp. 483–524, 2020.

[126] A. Mashal, F. Gao, and S. C. Hagness, "Heterogeneous anthropomorphic phantoms with realistic dielectric properties for microwave breast imaging experiments," *Microwave and Optical Technology Letters*, vol. 53, no. 8, pp. 1896–1902, 2011.

[127] Y. Nagao, Y. Kawaguchi, Y. Sugiyama, S. Saji, and Y. Kashiki, "Relationship between mammographic density and the risk of breast cancer in Japanese women: a case-control study," *Breast Cancer*, vol. 10, no. 3, pp. 228–233, 2003.

[128] D. A. Kennedy, T. Lee, and D. Seely, "A comparative review of thermography as a breast cancer screening technique," *Integrative Cancer Therapies*, vol. 8, no. 1, pp. 9–16, 2009.

[129] C. M. Studio, "Computer simulation technology," 2017.

[130] N. Carrara and I. IFAC-CNR, "Dielectric properties of body tissues," *IFAC-CNR, http://niremf. ifac. cnr. it/tissprop*, 2014.

[131] C. Gabriel, "Compilation of the dielectric properties of body tissues at rf and microwave frequencies.," tech. rep., King's Coll London (United Kingdom) Dept of Physics, 1996.

[132] C. Gabriel, S. Gabriel, and y. E. Corthout, "The dielectric properties of biological tissues: I. literature survey," *Physics in medicine & biology*, vol. 41, no. 11, p. 2231, 1996.

[133] S. Gabriel, R. Lau, and C. Gabriel, "The dielectric properties of biological tissues: Ii. measurements in the frequency range 10 hz to 20 ghz," *Physics in medicine & biology*, vol. 41, no. 11, p. 2251, 1996.

[134] S. Gabriel, R. Lau, and C. Gabriel, "The dielectric properties of biological tissues: Iii. parametric models for the dielectric spectrum of tissues," *Physics in medicine & biology*, vol. 41, no. 11, p. 2271, 1996.

[135] M. Klemm, J. A. Leendertz, D. Gibbins, I. J. Craddock, A. Preece, and R. Benjamin, "Microwave radar-based differential breast cancer imaging: Imaging in homogeneous breast phantoms and low contrast scenarios," *IEEE Transactions on Antennas and Propagation*, vol. 58, no. 7, pp. 2337–2344, 2010.

[136] E. C. Fear, X. Li, S. C. Hagness, and M. A. Stuchly, "Confocal microwave imaging for breast cancer detection: Localization of tumors in three dimensions," *IEEE Transactions on Biomedical Engineering*, vol. 49, no. 8, pp. 812–822, 2002.

[137] W. T. Joines, Y. Zhang, C. Li, and R. L. Jirtle, "The measured electrical properties of normal and malignant human tissues from 50 to 900 mhz," *Medical physics*, vol. 21, no. 4, pp. 547–550, 1994.

[138] S. Hagness, K. Leininger, J. Booske, and M. Okoniewski, "Dielectric characterization of human breast tissue at microwave frequencies," *2nd World Congr. Microwave and Radio Frequency Processing, Orlando, FL*, 2000.

[139] V. Gazhonova, *3D automated breast volume sonography*. Cham: Springer, 2017.

[140] J.-H. Chen, S. Chan, D.-C. Yeh, P. T. Fwu, M. Lin, and M.-Y. Su, "Response of bilateral breasts to the endogenous hormonal fluctuation in a menstrual cycle evaluated using 3d mri," *Magnetic resonance imaging*, vol. 31, no. 4, pp. 538–544, 2013.

[141] L. Hussain, W. Aziz, S. Saeed, S. Rathore, and M. Rafique, "Automated breast cancer detection using machine learning techniques by extracting different feature extracting strategies," in *2018 17th IEEE International Conference On Trust, Security And Privacy In Computing And Communications/12th IEEE International Conference On Big Data Science And Engineering (TrustCom/BigDataSE)*, (New York, United States), pp. 327–331, 2018.

[142] J. H. Youk, E.-K. Kim, K. H. Ko, and M. J. Kim, "Asymmetric mammographic findings based on the fourth edition of bi-rads: types, evaluation, and management," *Radiographics*, vol. 29, no. 1, pp. e33–e33, 2009.

[143] G. BuSSe, D. Wu, and W. Karpen, "Thermal wave imaging with phase sensitive modulated thermography," *Journal of Applied Physics*, vol. 71, no. 8, pp. 3962–3965, 1992.

[144] C. Ng, M. M. Zamri, H. Ng, J. Ng, S. Mazlan, W. Chuah, Z. Ooi, Y. Ooi, and S. Chen, "Power plane defect findings in silicon with lock-in thermography & OBIRCH/TIVA techniques," in *2020 IEEE International Symposium on the Physical and Failure Analysis of Integrated Circuits (IPFA)*, pp. 1–4, IEEE, 2020.

[145] S. Johnston, H. Guthrey, F. Yan, K. Zaunbrecher, M. Al-Jassim, P. Rakotoniaina, and M. Kaes, "Correlating multicrystalline silicon defect types using photoluminescence, defect-band emission, and lock-in thermography imaging techniques," *IEEE Journal of Photovoltaics*, vol. 4, no. 1, pp. 348–354, 2013.

[146] Y. C. Wang and K.-Y. Lin, "3D defect localization of stacked die devices by lock-in thermography (LIT)," in *2018 IEEE International Symposium on the Physical and Failure Analysis of Integrated Circuits (IPFA)*, pp. 1–4, IEEE, 2018.

[147] S. Huth, O. Breitenstein, A. Huber, D. Dantz, U. Lambert, and F. Altmann, "Lock-in ir-thermography-a novel tool for material and device characterization," *Solid state phenomena*, vol. 82, pp. 741–746, 2002.

[148] O. Breitenstein, W. Warta, and M. C. Schubert, *Lock-in thermography: Basics and use for evaluating electronic devices and materials*, vol. 10. Springer, 2019.

[149] M. Asefi, A. Baran, and J. LoVetri, "An experimental phantom study for air-based quasi-resonant microwave breast imaging," *IEEE Transactions on Microwave Theory and Techniques*, vol. 67, no. 9, pp. 3946–3954, 2019.

[150] M. Lazebnik, E. L. Madsen, G. R. Frank, and S. C. Hagness, "Tissue-mimicking phantom materials for narrowband and ultrawideband microwave applications," *Physics in Medicine & Biology*, vol. 50, no. 18, pp. 4245–4258, 2005.

[151] K. Muzaffar, D. Roy, S. Tuli, and S. Koul, "Frequency modulated thermal wave imaging for visualizing power density of electromagnetic waves on plane surfaces," *Research in Nondestructive Evaluation*, vol. 30, no. 2, pp. 65–79, 2019.

[152] D. Alsaedi, A. Melnikov, K. Muzaffar, A. Mandelis, and O. M. Ramahi, "A microwave-thermography hybrid technique for breast cancer detection," *IEEE Journal of Electromagnetics, RF and Microwaves in Medicine and Biology*, 2021. doi: 10.1109/JERM.2021.3072451.

[153] W. Padilla, M. Aronsson, C. Highstrete, M. Lee, A. Taylor, and R. Averitt, "Electrically resonant terahertz metamaterials: Theoretical and experimental investigations," *Physical Review B*, vol. 75, no. 4, pp. 041102R–1– 041102R–4, 2007.

[154] C. M. Studio, "Computer simulation technology," 2017.

[155] M. El Badawe, T. S. Almoneef, and O. M. Ramahi, "A true metasurface antenna," *Scientific reports*, vol. 6, no. 1, pp. 1–8, 2016.

[156] K. Kerlikowske, W. Zhu, A. N. Tosteson, B. L. Sprague, J. A. Tice, C. D. Lehman, and D. L. Miglioretti, "Identifying women with dense breasts at high risk for interval cancer: a cohort study," *Annals of internal medicine*, vol. 162, no. 10, pp. 673–681, 2015.

[157] S. Narod, J. Iqbal, A. Jakubowska, T. Huzarski, P. Sun, C. Cybulski, J. Gronwald, T. Byrski, and J. Lubinski, "Are two-centimeter breast cancers large or small?," *Current oncology*, vol. 20, no. 4, pp. 205–211, 2013.

[158] BREASTCANCER.ORG, "Breast cancer stages," 2021. [Online]. Available: https://www.breastcancer.org/symptoms/diagnosis/stagingstage0. [Last accessed 19 Aug 2021].

[159] L. Hussain, W. Aziz, S. Saeed, S. Rathore, and M. Rafique, "Automated breast cancer detection using machine learning techniques by extracting different feature extracting strategies," in *2018 17th IEEE International Conference On Trust, Security And Privacy In Computing And Communications/12th IEEE International Conference On Big Data Science And Engineering (TrustCom/BigDataSE)*, (New York, United States), pp. 327–331, IEEE, 2018.

[160] N. Wu *et al.*, "Deep neural networks improve radiologists' performance in breast cancer screening," *IEEE transactions on medical imaging*, vol. 39, no. 4, pp. 1184–1194, 2020.

[161] M. Lazebnik, E. L. Madsen, G. R. Frank, and S. C. Hagness, "Tissue-mimicking phantom materials for narrowband and ultrawideband microwave applications," *Physics in Medicine & Biology*, vol. 50, no. 18, p. 4245, 2005.

[162] S. Di Meo, L. Pasotti, I. Iliopoulos, M. Pasian, M. Ettorre, M. Zhadobov, and G. Matrone, "Tissue-mimicking materials for breast phantoms up to 50 ghz," *Physics in Medicine & Biology*, vol. 64, no. 5, p. 055006, 2019.

[163] S. Gabriel, R. Lau, and C. Gabriel, "The dielectric properties of biological tissues: Ii. measurements in the frequency range 10 hz to 20 ghz," *Physics in medicine & biology*, vol. 41, no. 11, p. 2251, 1996.

[164] A. Martellosio, M. Pasian, M. Bozzi, L. Perregrini, A. Mazzanti, F. Svelto, P. Summers, G. Renne, and M. Bellomi, "0.5–50 ghz dielectric characterisation of breast cancer tissues," *Electronics Letters*, vol. 51, no. 13, pp. 974–975, 2015.

[165] S. Di Meo, P. F. Espin-Lopez, A. Martellosio, M. Pasian, M. Bozzi, L. Perregrini, A. Mazzanti, F. Svelto, P. E. Summers, G. Renne, L. Preda, and M. Bellomi, "Dielectric properties of breast tissues: Experimental results up to 50 ghz," in *12th European Conference on Antennas and Propagation (EuCAP 2018)*, pp. 1–5, 2018.

[166] S. Di Meo, P. F. Espin-Lopez, A. Martellosio, M. Pasian, M. Bozzi, L. Peregrini, A. Mazzanti, F. Svelto, P. E. Summers, G. Renne, L. Preda, and M. Bellomi, "Experimental validation of the dielectric permittivity of breast cancer tissues up to 50 ghz," in *2017 IEEE MTT-S International Microwave Workshop Series on Advanced Materials and Processes for RF and THz Applications (IMWS-AMP)*, pp. 1–3, 2017.

[167] H. Bahramiabarghouei, E. Porter, A. Santorelli, B. Gosselin, M. Popović, and L. A. Rusch, "Flexible 16 antenna array for microwave breast cancer detection," *IEEE Transactions on Biomedical Engineering*, vol. 62, no. 10, pp. 2516–2525, 2015.

[168] A. Santorelli, E. Porter, E. Kang, T. Piske, M. Popović, and J. D. Schwartz, "A time-domain microwave system for breast cancer detection using a flexible circuit board," *IEEE Transactions on Instrumentation and Measurement*, vol. 64, no. 11, pp. 2986–2994, 2015.

[169] B. Thors and L. Josefsson, "Radiation and scattering tradeoff design for conformal arrays," *IEEE Transactions on Antennas and Propagation*, vol. 51, no. 5, pp. 1069–1076, 2003.

[170] H. F. Carlak, *Medical Electro-Thermal Imaging*. PhD thesis, Middle East Technical University, 2014.

[171] R. EFJ., "Thermographic terminology," *Acta Thermographica*, pp. 1–30, 1978.

[172] P. Gamagami, "Indirect signs of breast cancer: Angiogenesis study, In All as of Mammography," *MA Blackwell Science*, no. 6, pp. 231–258, 1996.

[173] D. WL, "Evaluation of a palpable breast mass," *The New England Journal of Medicine*, vol. 327, no. 13, pp. 937–942, 1992.

[174] R. M. Sega and J. D. Norgard, "Infrared Measurements of Scattering And Electromagnetic Penetration Through Apertures," *IEEE Transactions on Nuclear Science*, vol. 33, no. 6, pp. 1657–1663, 1986.

[175] K. Muzaffar, L. I. Giri, K. Chatterjee, S. Tuli, and S. Koul, "Fault detection of antenna arrays using infrared thermography," *Infrared Physics & Technology*, vol. 71, pp. 464–468, 2015.

[176] N. Chiyo, M. Arai, Y. Tanaka, and T. Maeno, "Measurement Technique for Electromagnetic Field Intensity Distribution using Infrared 2-D Lock-in Amplifier,"

[177] R. Sikora, T. Chady, and B. Szymanik, "Infrared thermographic testing of composite materials with adhesive joints," in *Proceedings of the 18th World Conference on Nondestructive Testing, Durban, South Africa*, pp. 16–20, 2012.

[178] R. Lawson, "Implications of surface temperatures in the diagnosis of breast cancer," *Canadian Medical Association Journal*, vol. 75, no. 4, p. 309, 1956.

[179] R. N. Lawson and M. Chughtai, "Breast cancer and body temperature," *Canadian Medical Association Journal*, vol. 88, no. 2, p. 68, 1963.

[180] S. A. Feig, G. S. Shaber, G. F. Schwartz, A. Patchefsky, H. I. Libshitz, J. Edeiken, R. Nerlinger, R. F. Curley, and J. D. Wallace, "Thermography, mammography, and clinical examination in breast cancer screening: review of 16,000 studies," *Radiology*, vol. 122, no. 1, pp. 123–127, 1977.

[181] J. Keyserlingk, P. Ahlgren, E. Yu, N. Belliveau, and M. Yassa, "Functional infrared imaging of the breast," *IEEE Engineering in Medicine and Biology Magazine*, vol. 19, no. 3, pp. 30–41, 2000.

[182] M. Gautherie, "Thermopathology of breast cancer: measurement and analysis of in vivo temperature and blood flow," *Annals of the New York Academy of Sciences*, vol. 335, no. 1, pp. 383–415, 1980.

[183] J. P. Agnelli, A. Barrea, and C. V. Turner, "Tumor location and parameter estimation by thermography," *Mathematical and Computer Modelling*, vol. 53, no. 7-8, pp. 1527–1534, 2011.

[184] M. Gautherie and C. M. Gros, "Breast thermography and cancer risk prediction," *Cancer*, vol. 45, no. 1, pp. 51–56, 1980.

[185] R. A. H. Spitalier, D. Giraud, "Does infrared thermography truly have a role in present-day cancer management," *Biomedical Thermology*, pp. 269–278, 1982.

[186] W. Hobbins, "Thermography, highest risk marker in breast cancer," in *Proceedings of the Gynecological Society for the Study of Breast Disease*, pp. 67–282, 1977.

[187] M. Gautherie, "Thermobiological assessment of benign and malignant breast diseases," *American Journal of Obstetrics & Gynecology*, vol. 147, no. 8, pp. 861–869, 1983.

[188] J. D. Haberman, T. J. Love, and J. E. Francis, "Screening a rural population for breast cancer using thermography and physical examination techniques: Methods and results-a preliminary report," *Annals of the New York Academy of Sciences*, vol. 335, no. 1, pp. 492–500, 1980.

[189] H. Usuki, "[evaluation of the thermographic diagnosis of breast disease–relation of thermographic findings and pathologic findings of cancer growth].," *Nihon Gan Chiryo Gakkai shi*, vol. 23 11, pp. 2687–95, 1988.

[190] Y. A. I. Nyirjesy, "Clinical evaluation, mammography and thermography in the diagnosis of breast carcinoma," *Thermology*, no. 1, p. 170, 1986.

[191] Y. Parisky, A. Sardi, R. Hamm, K. Hughes, L. Esserman, S. Rust, and K. Callahan, "Efficacy of computerized infrared imaging analysis to evaluate mammographically suspicious lesions," *American Journal of Roentgenology*, vol. 180, no. 1, pp. 263–269, 2003.

[192] F. González, "Thermal simulation of breast tumors," *Revista mexicana de fisica*, vol. 53, no. 4, pp. 323–326, 2007.

[193] L. Jiang, W. Zhan, and M. H. Loew, "Modeling static and dynamic thermography of the human breast under elastic deformation," *Physics in Medicine & Biology*, vol. 56, no. 1, p. 187, 2010.

[194] H. F. Carlak, N. G. Gençer, and C. Beşikçi, "Medical thermal imaging of electrically stimulated woman breast: a simulation study," in *Engineering in Medicine and Biology Society, EMBC, 2011 Annual International Conference of the IEEE*, pp. 4905–4908, IEEE, 2011.

[195] Y. Ohashi and I. Uchida, "Applying dynamic thermography in the diagnosis of breast cancer," *IEEE Engineering in Medicine and Biology Magazine*, vol. 19, no. 3, pp. 42–51, 2000.

[196] R. R. de Jesus Guirro, M. M. O. L. L. Vaz, L. M. S. das Neves, A. V. Dibai-Filho, H. H. A. Carrara, and E. C. de Oliveira Guirro, "Accuracy and reliability of infrared thermography in assessment of the breasts of women affected by cancer," *Journal of medical systems*, vol. 41, no. 5, p. 87, 2017.

[197] C. A. Balanis, *Advanced engineering electromagnetics*. John Wiley & Sons, 1999.

[198] G. d'Ambrosio, R. Massa, M. D. Migliore, G. Cavaccini, A. Ciliberto, and C. Sabatino, "Microwave excitation for thermographic nde: An experimental study and some theoretical evaluations," *Materials evaluation*, vol. 53, no. 4, pp. 502–508, 1995.

[199] S. Chaudhary, "Dielectric properties of normal and malignant human breast tissues at radiowave and microwave frequencies," *Indian J. of Biochem. Biophs.*, vol. 21, pp. 76–79, 1984.

[200] A. J. Surowiec, S. S. Stuchly, J. R. Barr, and A. Swarup, "Dielectric properties of breast carcinoma and the surrounding tissues," *IEEE Transactions on Biomedical Engineering*, vol. 35, no. 4, pp. 257–263, 1988.

[201] K. Muzaffar, S. Tuli, and S. Koul, "Infrared thermography for electromagnetic field pattern recognition," in *Microwave and RF Conference, 2013 IEEE MTT-S International*, pp. 1–4, IEEE, 2013.

[202] D. Balageas and P. Levesque, "Emir: a photothermal tool for electromagnetic phenomena characterization," *Revue générale de Thermique*, vol. 37, no. 8, p. 725, 1998.

[203] K. Muzaffar, L. I. Giri, K. Chatterjee, S. Tuli, and S. Koul, "Fault detection of antenna arrays using infrared thermography," *Infrared Physics & Technology*, vol. 71, pp. 464–468, 2015.

[204] N. S. Winkler, S. Raza, M. Mackesy, and R. L. Birdwell, "Breast density: clinical implications and assessment methods," *Radiographics*, vol. 35, no. 2, pp. 316–324, 2015.

[205] A. Mashal, F. Gao, and S. C. Hagness, "Heterogeneous anthropomorphic phantoms with realistic dielectric properties for microwave breast imaging experiments," *Microwave and optical technology letters*, vol. 53, no. 8, pp. 1896–1902, 2011.

[206] W. Berg, E. Hendrick, D. Kopans, and R. Smith, "Frequently asked questions about mammography and the uspstf recommendations: A guide for practitioners," *Reston, VA: Society of Breast Imaging*, 2009.

[207] L. A. G. Ries, J. L. Young Jr, G. E. Keel, M. P. Eisner, Y. D. Lin, and M.-J. D. Horner, "Cancer survival among adults: Us seer program, 1988–2001," *Patient and tumor characteristics SEER Survival Monograph Publication*, pp. 07–6215, 2007.

[208] T. Otake, "Cancer and breast density: What are doctors withholding?," 2017.

[209] U. P. S. T. Force *et al.*, "Screening for breast cancer: Us preventive services task force recommendation statement.," *Annals of Internal Medicine*, vol. 151, no. 10, pp. 716–726, 2009.

[210] D. Alsaedi and O. M. Ramahi, "A microwave-thermography hybrid technique for breast cancer detection," *US Provisional Patent*, April 2021.

[211] M. D. Hossain and A. S. Mohan, "Cancer detection in highly dense breasts using coherently focused time-reversal microwave imaging," *IEEE Transactions on Computational Imaging*, vol. 3, no. 4, pp. 928–939, 2017.

[212] W. A. Berg, L. Gutierrez, M. S. NessAiver, W. B. Carter, M. Bhargavan, R. S. Lewis, and O. B. Ioffe, "Diagnostic accuracy of mammography, clinical examination, us, and mr imaging in preoperative assessment of breast cancer," *Radiology*, vol. 233, no. 3, pp. 830–849, 2004.

[213] L. M. Schwartz, S. Woloshin, H. C. Sox, B. Fischhoff, and H. G. Welch, "Us women's attitudes to false positive mammography results and detection of ductal carcinoma in situ: cross sectional survey," *Bmj*, vol. 320, no. 7250, pp. 1635–1640, 2000.

[214] C. D. Lehman *et al.*, "National performance benchmarks for modern screening digital mammography: update from the breast cancer surveillance consortium," *Radiology*, vol. 283, no. 1, pp. 49–58, 2017.

[215] M. T. Ghasr, M. A. Abou-Khousa, S. Kharkovsky, R. Zoughi, and D. Pommerenke, "Portable real-time microwave camera at 24 GHz," *IEEE Transactions on Antennas and Propagation*, vol. 60, no. 2, pp. 1114–1125, 2011.

[216] A. P. Smith *et al.*, "Emerging technologies in breast cancer detection," *Radiology Management*, vol. 26, no. 4, pp. 16–27, 2004.

[217] M. Klemm, J. Leendertz, D. Gibbins, I. Craddock, A. Preece, and R. Benjamin, "Microwave radar-based breast cancer detection: Imaging in inhomogeneous breast phantoms," *IEEE Antennas and Wireless Propagation Letters*, vol. 8, pp. 1349–1352, 2009.

[218] D. Balageas and P. Levesque, "Emir: a photothermal tool for electromagnetic phenomena characterization," *Revue générale de Thermique*, vol. 37, no. 8, pp. 725–739, 1998.

[219] L. G. Ries *et al.*, "Seer survival monograph: cancer survival among adults: Us seer program, 1988-2001, patient and tumor characteristics," *National Cancer Institute, SEER Program, NIH Pub*, no. 07-6215, pp. 193–202, 2007.

[220] M. A. Aldhaeebi, T. S. Almoneef, H. Attia, and O. M. Ramahi, "Near-field microwave loop array sensor for breast tumor detection," *IEEE Sensors Journal*, vol. 19, no. 24, pp. 11867–11872, 2019.

[221] T. Henriksson, M. Klemm, D. Gibbins, J. Leendertz, T. Horseman, A. Preece, R. Benjamin, and I. Craddock, "Clinical trials of a multistatic uwb radar for breast imaging," in *2011 Loughborough Antennas & Propagation Conference*, pp. 1–4, IEEE, 2011.

[222] A. B. De González, M. Mahesh, K.-P. Kim, M. Bhargavan, R. Lewis, F. Mettler, and C. Land, "Projected cancer risks from computed tomographic scans performed in the United States in 2007," *Archives of internal medicine*, vol. 169, no. 22, pp. 2071–2077, 2009.

[223] F. A. Mettler Jr, "Medical radiation exposure in the United States: 2006–2016 trends," *Health Physics*, vol. 116, no. 2, pp. 126–128, 2019.

[224] R. Conceicao, M. O'halloran, M. Glavin, and E. Jones, "Evaluation of features and classifiers for classification of early-stage breast cancer," *Journal of Electromagnetic Waves and Applications*, vol. 25, no. 1, pp. 1–14, 2011.

[225] G. Geetharamani and T. Aathmanesan, "Metamaterial inspired thz antenna for breast cancer detection," *SN Applied Sciences*, vol. 1, no. 6, p. 595, 2019.

[226] M. El Badawe and O. M. Ramahi, "Efficient metasurface rectenna for electromagnetic wireless power transfer and energy harvesting," *Progress In Electromagnetics Research*, vol. 161, pp. 35–40, 2018.

[227] D. M. Sheen, D. L. McMakin, and T. E. Hall, "Three-dimensional millimeter-wave imaging for concealed weapon detection," *IEEE Transactions on microwave theory and techniques*, vol. 49, no. 9, pp. 1581–1592, 2001.

[228] R. Persico, *Introduction to ground penetrating radar: inverse scattering and data processing*. John Wiley & Sons, 2014.

[229] M. Klemm, J. Leendertz, D. Gibbins, I. Craddock, A. Preece, and R. Benjamin, "Microwave radar-based breast cancer detection: Imaging in inhomogeneous breast phantoms," *IEEE Antennas and Wireless Propagation Letters*, vol. 8, pp. 1349–1352, 2009.

[230] S. M. Salvador, E. C. Fear, M. Okoniewski, and J. R. Matyas, "Exploring joint tissues with microwave imaging," *IEEE Transactions on Microwave Theory and Techniques*, vol. 58, no. 8, pp. 2307–2313, 2010.

[231] M. A. Islam and J. L. Volakis, "Wearable microwave imaging sensor for deep tissue real-time monitoring using a new loss-compensated backpropagation technique," *IEEE Sensors Journal*, vol. 21, no. 3, pp. 3324–3334, 2020.

[232] E. C. Fear, S. C. Hagness, P. M. Meaney, M. Okoniewski, and M. A. Stuchly, "Enhancing breast tumor detection with near-field imaging," *IEEE Microwave magazine*, vol. 3, no. 1, pp. 48–56, 2002.

[233] O. Yurduseven, M. F. Imani, H. Odabasi, J. Gollub, G. Lipworth, A. Rose, and D. R. Smith, "Resolution of the frequency diverse metamaterial aperture imager," *Progress In Electromagnetics Research*, vol. 150, pp. 97–107, 2015.

[234] J. Hunt, J. Gollub, T. Driscoll, G. Lipworth, A. Mrozack, M. S. Reynolds, D. J. Brady, and D. R. Smith, "Metamaterial microwave holographic imaging system," *JOSA A*, vol. 31, no. 10, pp. 2109–2119, 2014.

[235] S. Mukherjee, Z. Su, L. Udpa, S. Udpa, and A. Tamburrino, "Enhancement of microwave imaging using a metamaterial lens," *IEEE Sensors Journal*, vol. 19, no. 13, pp. 4962–4971, 2019.

[236] E. Razzicchia, I. Sotiriou, H. Cano-Garcia, E. Kallos, G. Palikaras, and P. Kosmas, "Feasibility study of enhancing microwave brain imaging using metamaterials," *Sensors*, vol. 19, no. 24, p. 5472, 2019.

[237] M. T. Islam, M. Samsuzzaman, M. T. Islam, and S. Kibria, "Experimental breast phantom imaging with metamaterial-inspired nine-antenna sensor array," *Sensors*, vol. 18, no. 12, p. 4427, 2018.

[238] M. T. Islam, M. Islam, M. Samsuzzaman, M. R. I. Faruque, N. Misran, *et al.*, "A negative index metamaterial-inspired uwb antenna with an integration of complementary srr and cls unit cells for microwave imaging sensor applications," *Sensors*, vol. 15, no. 5, pp. 11601–11627, 2015.

[239] N. Engheta and R. W. Ziolkowski, *Metamaterials: physics and engineering explorations*. John Wiley & Sons, 2006.

[240] A. Sihvola, "Metamaterials in electromagnetics," *Metamaterials*, vol. 1, no. 1, pp. 2–11, 2007.

[241] M. Moschetti, M. Ritzwoller, and N. Shapiro, "Surface wave tomography of the western united states from ambient seismic noise: Rayleigh wave group velocity maps," *Geochemistry, Geophysics, Geosystems*, vol. 8, no. 8, 2007.

[242] R. C. Conceição, J. J. Mohr, M. O'Halloran, *et al.*, *An introduction to microwave imaging for breast cancer detection*. Springer, 2016.

[243] W. Chew, "Imaging and inverse problems in electromagnetics," *Advances in Computational Electrodynamics: The Finite-Difference Time-Domain Method*, pp. 653–702, 1998.

APPENDICES

Appendix A

Calculating the differences between the figures of Chapter 3

Several techniques were used utilizing Matlab to extract more differences between the images that have a power expression comparison in this chapter (i.e., Figs. 3.5 - 3.8).

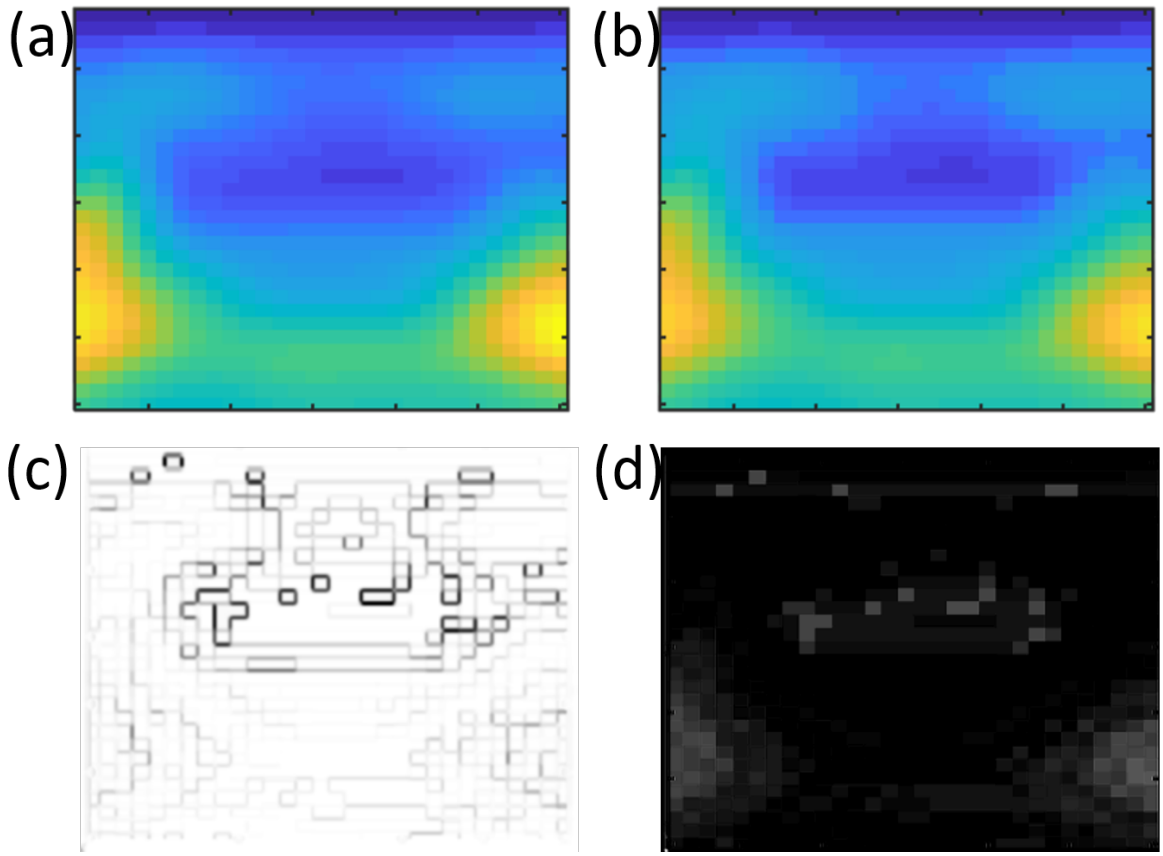

Figure A.1: Using Fig. 3.5, the differences between the power impression of the (a) healthy breast and (b) unhealthy breast are calculated using (c) SSIM map, where the shapes with darker edges show the differences, and (d) images subtraction technique, where the shapes with a lighter color indicate the differences. The percentage difference between images is: 1.3026%.

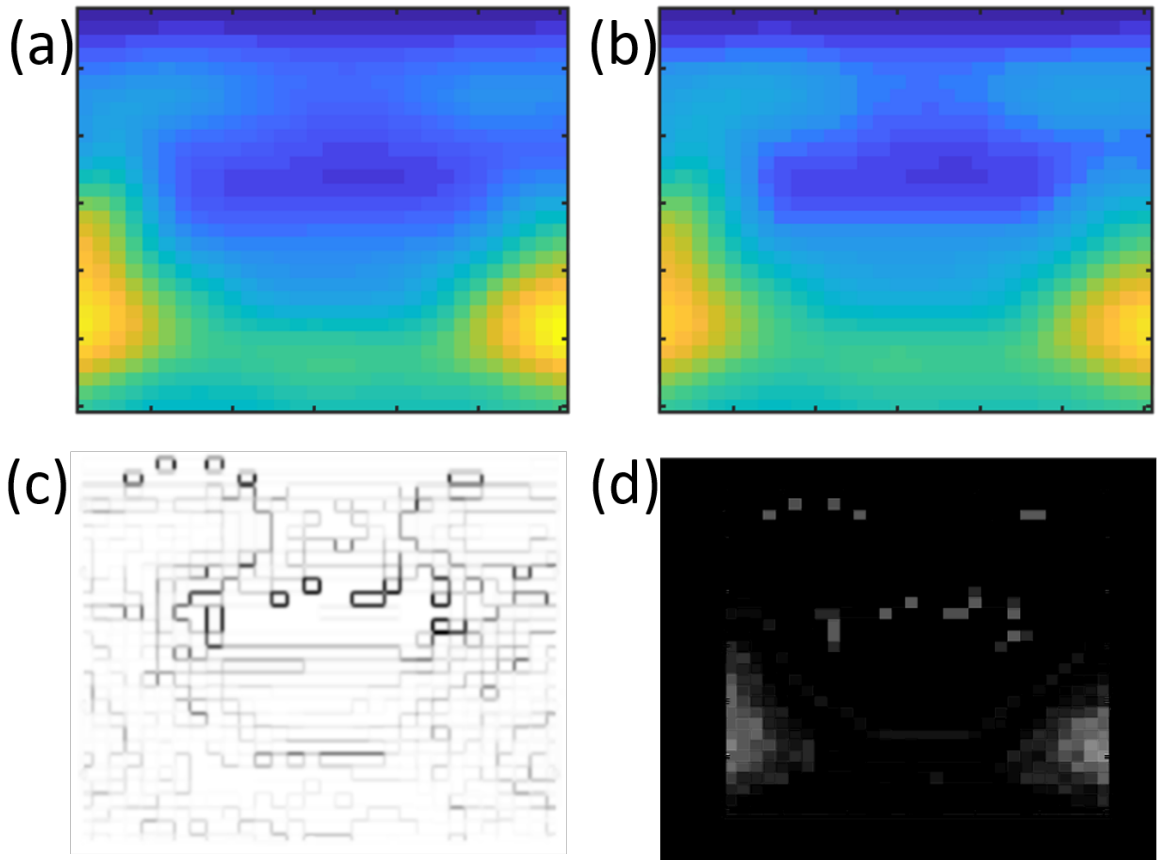

Figure A.2: Using Fig. 3.6, the differences between the power impression of the (a) 4 mm radius tumor and (b) 5 mm radius tumor are calculated using (c) SSIM map, where the shapes with darker edges show the differences, and (d) images subtraction technique, where the shapes with a lighter color indicate the differences. The percentage difference between images is: 1.7516%.

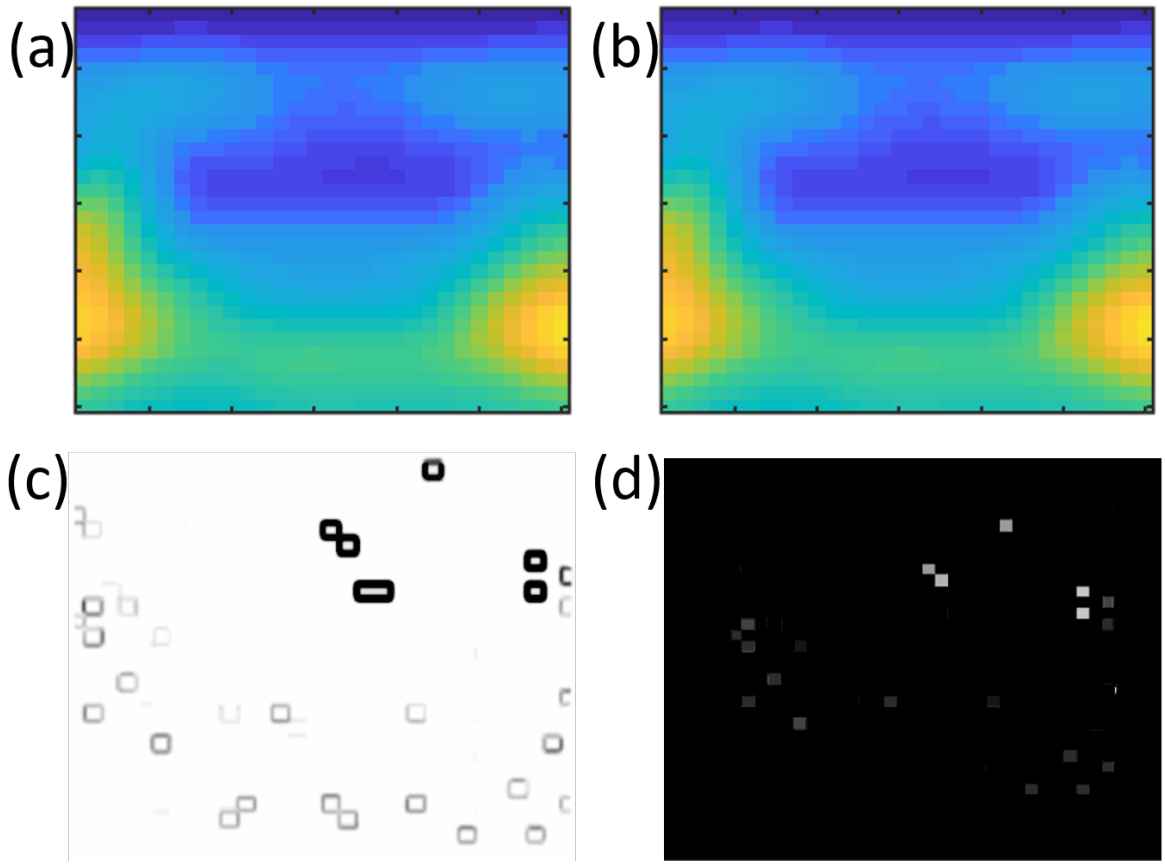

Figure A.3: Using Fig. 3.6, the differences between the power impression of the (a) 5 mm radius tumor and (b) 6 mm radius tumor are calculated using (c) SSIM map, where the shapes with darker edges show the differences, and (d) images subtraction technique, where the shapes with a lighter color indicate the differences. The percentage difference between images is: 0.054879%.

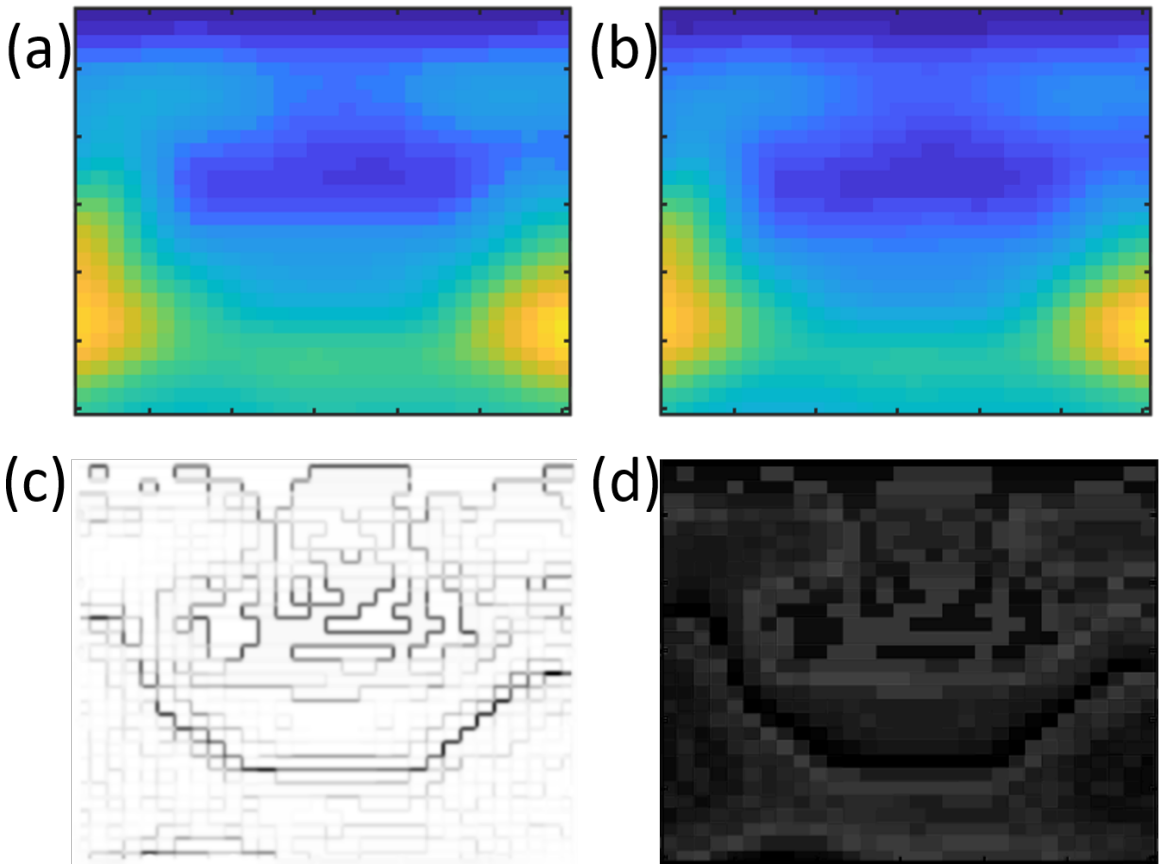

Figure A.4: Using Fig. 3.7, the differences between the power impression of the (a) tumor at location 1 and (b) tumor at location 2 are calculated using (c) SSIM map, where the shapes with darker edges show the differences, and (d) images subtraction technique, where the shapes with a lighter color indicate the differences. The percentage difference between images is: 3.3736%.

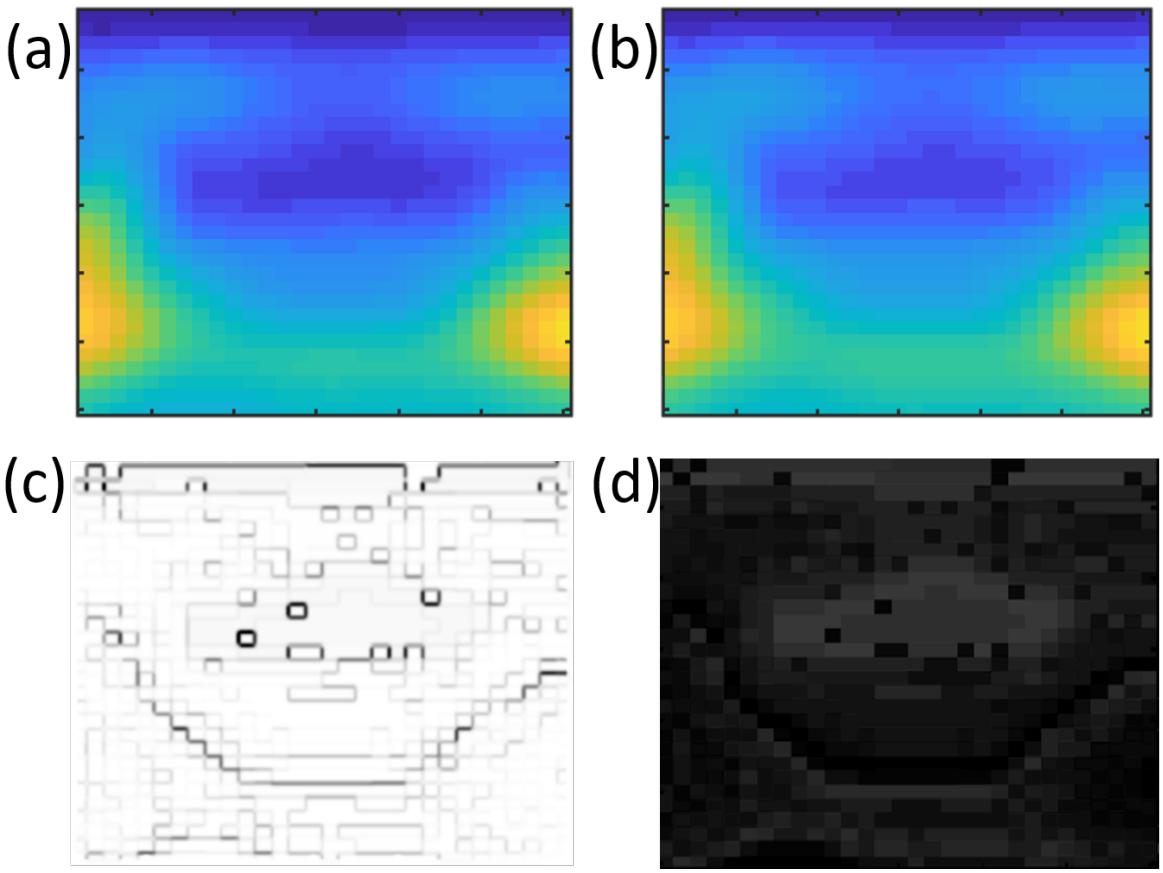

Figure A.5: Using Fig. 3.7, the differences between the power impression of the (a) tumor at location 1 and (b) tumor at location 2 are calculated using (c) SSIM map, where the shapes with darker edges show the differences, and (d) images subtraction technique, where the shapes with a lighter color indicate the differences. The percentage difference between images is: 2.2119%.

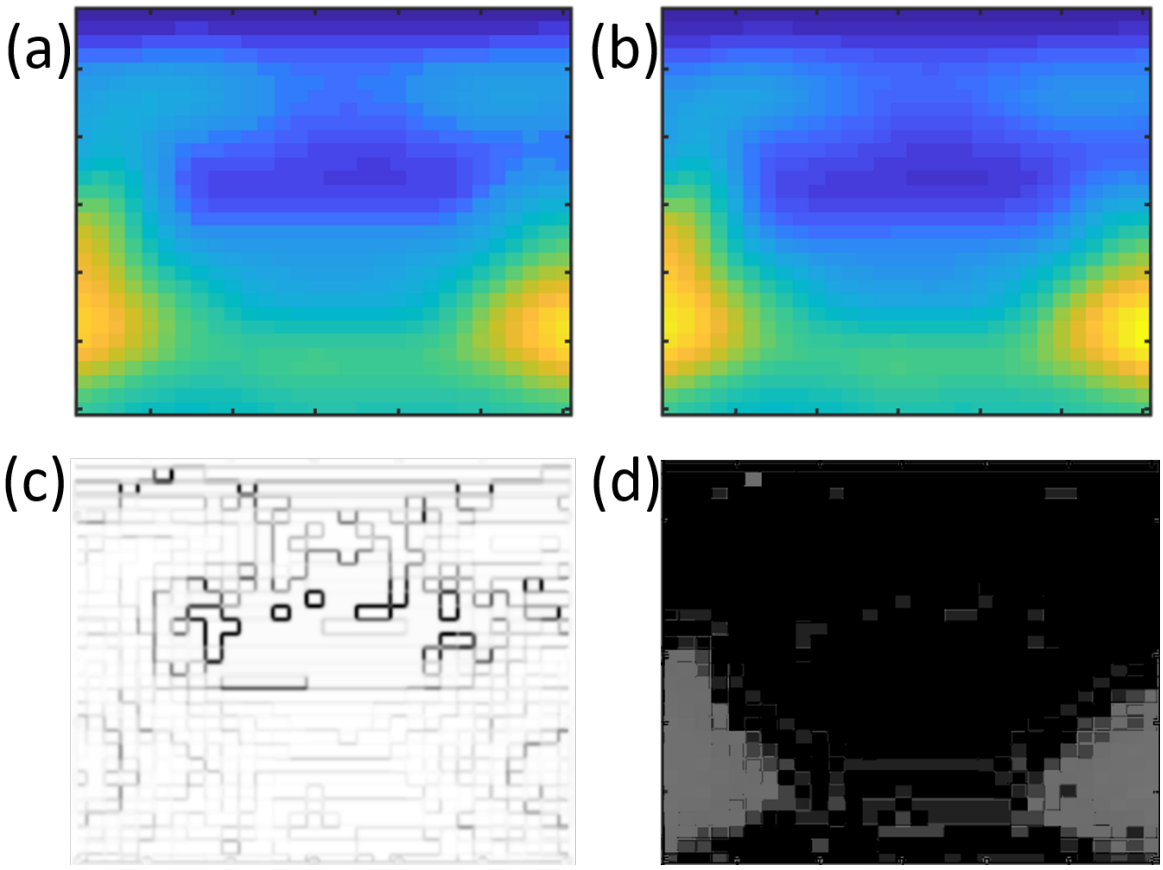

Figure A.6: Using Fig. 3.8, the differences between the power impression of the (a) tumor at depth 15 mm and (b) tumor at depth 20 mm are calculated using (c) SSIM map, where the shapes with darker edges show the differences, and (d) images subtraction technique, where the shapes with a lighter color indicate the differences. The percentage difference between images is: 1.9155%.

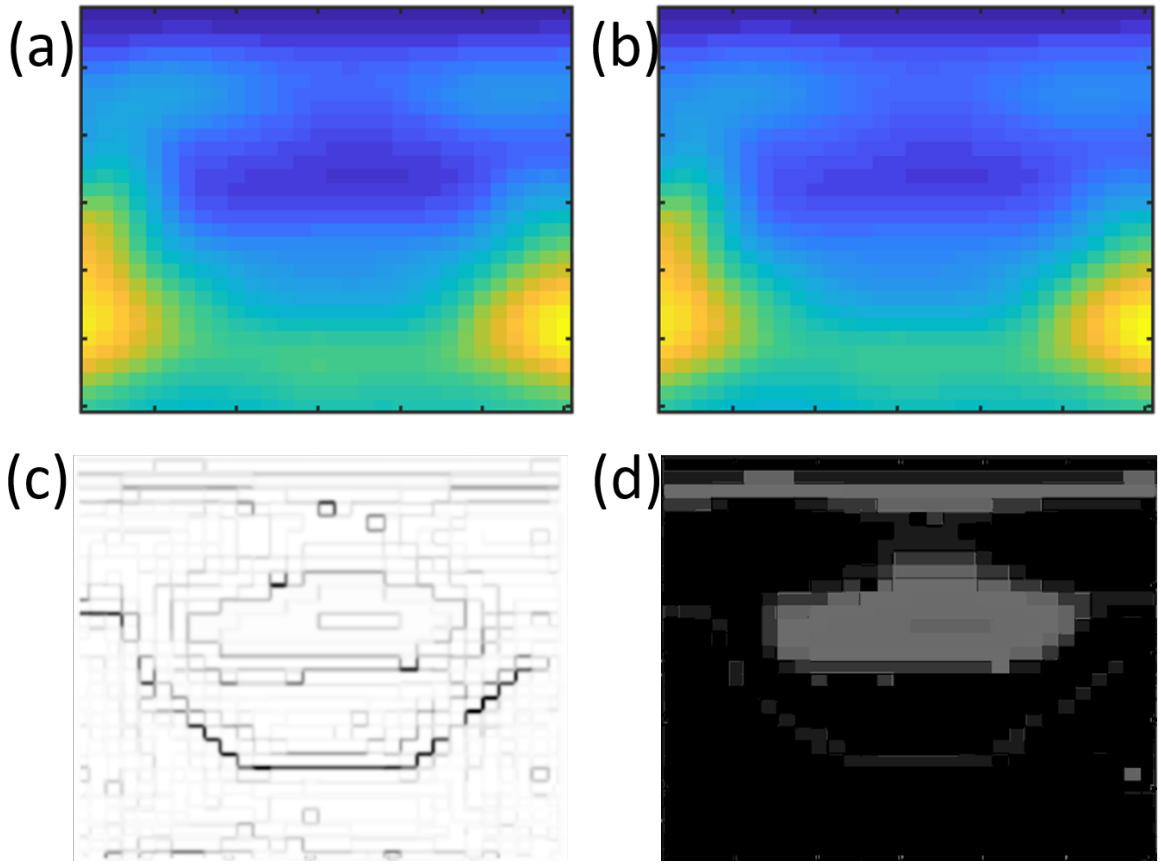

Figure A.7: Using Fig. 3.8, the differences between the power impression of the (a) tumor at depth 20 mm and (b) tumor at depth 25 mm are calculated using (c) SSIM map, where the shapes with darker edges show the differences, and (d) images subtraction technique, where the shapes with a lighter color indicate the differences. The percentage difference between images is: 1.3034%.

Appendix B

Calculating the differences between the figures of chapter 4

Several techniques were used utilizing Matlab to extract more differences between the images that have a power expression comparison in this chapter (i.e., Figs. 4.6, 4.8, 4.9, and 4.10).

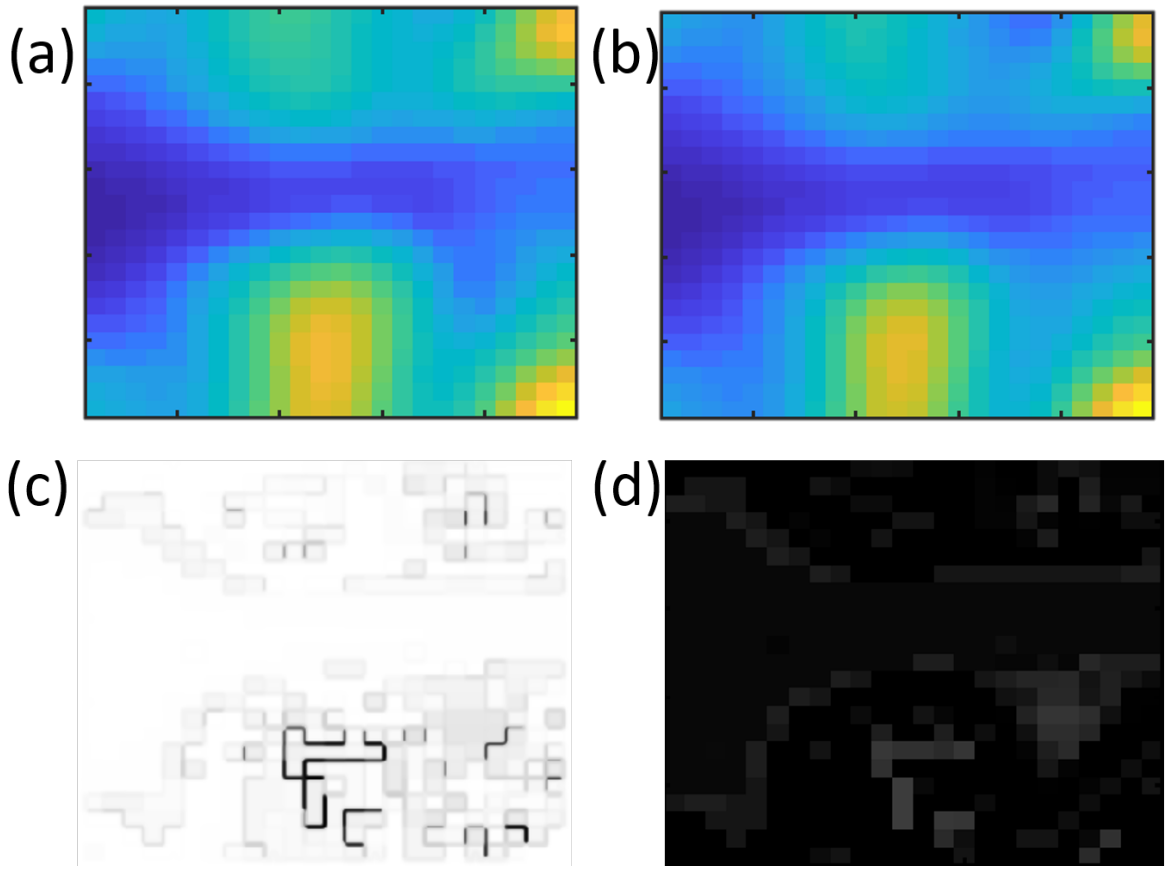

Figure B.1: Using Fig. 4.6, the differences between the power impression of the (a) healthy breast and (b) unhealthy breast are calculated using (c) SSIM map, where the shapes with darker edges show the differences, and (d) images subtraction technique, where the shapes with a lighter color indicate the differences. The percentage difference between images is: 2.1953%.

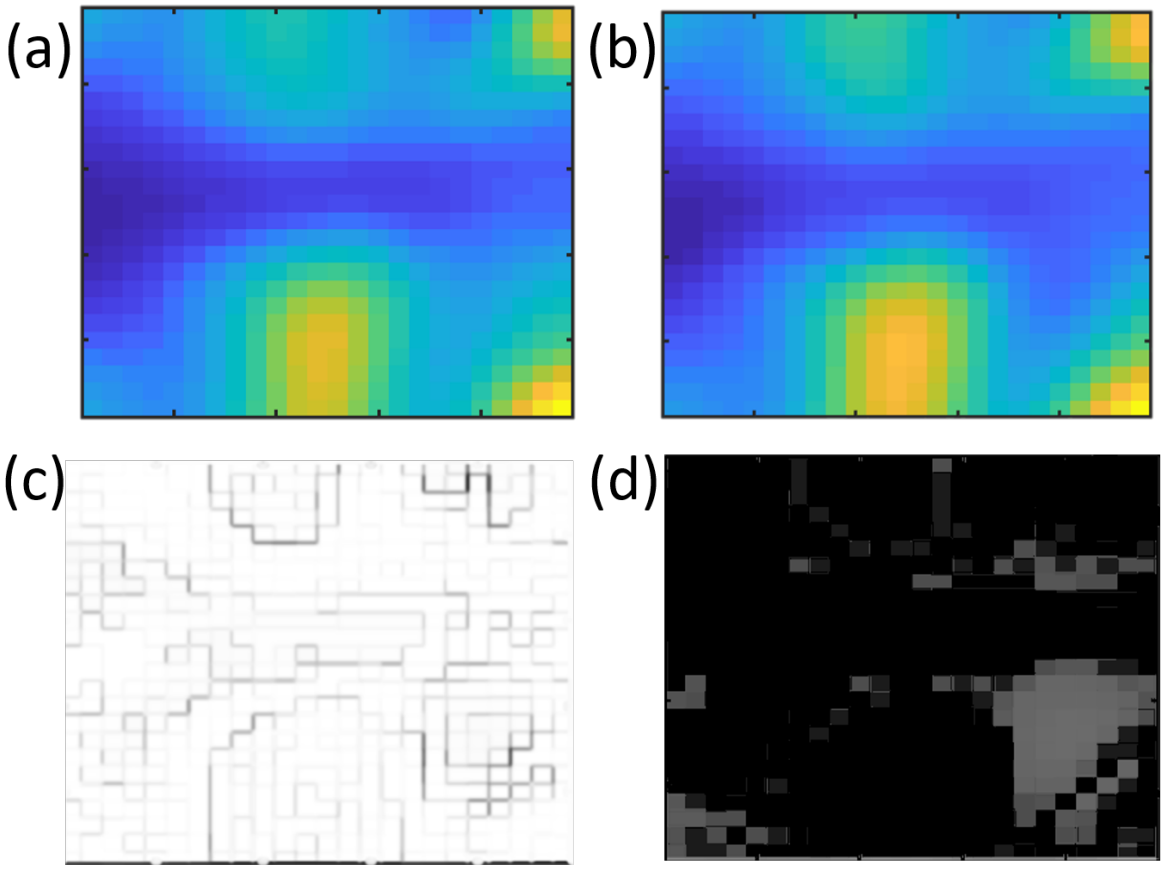

Figure B.2: Using Fig. 4.8, the differences between the power impression of the (a)tumor at location 1 and (b) tumor at location 2 are calculated using (c) SSIM map, where the shapes with darker edges show the differences, and (d) images subtraction technique, where the shapes with a lighter color indicate the differences. The percentage difference between images is: 2.4117%.

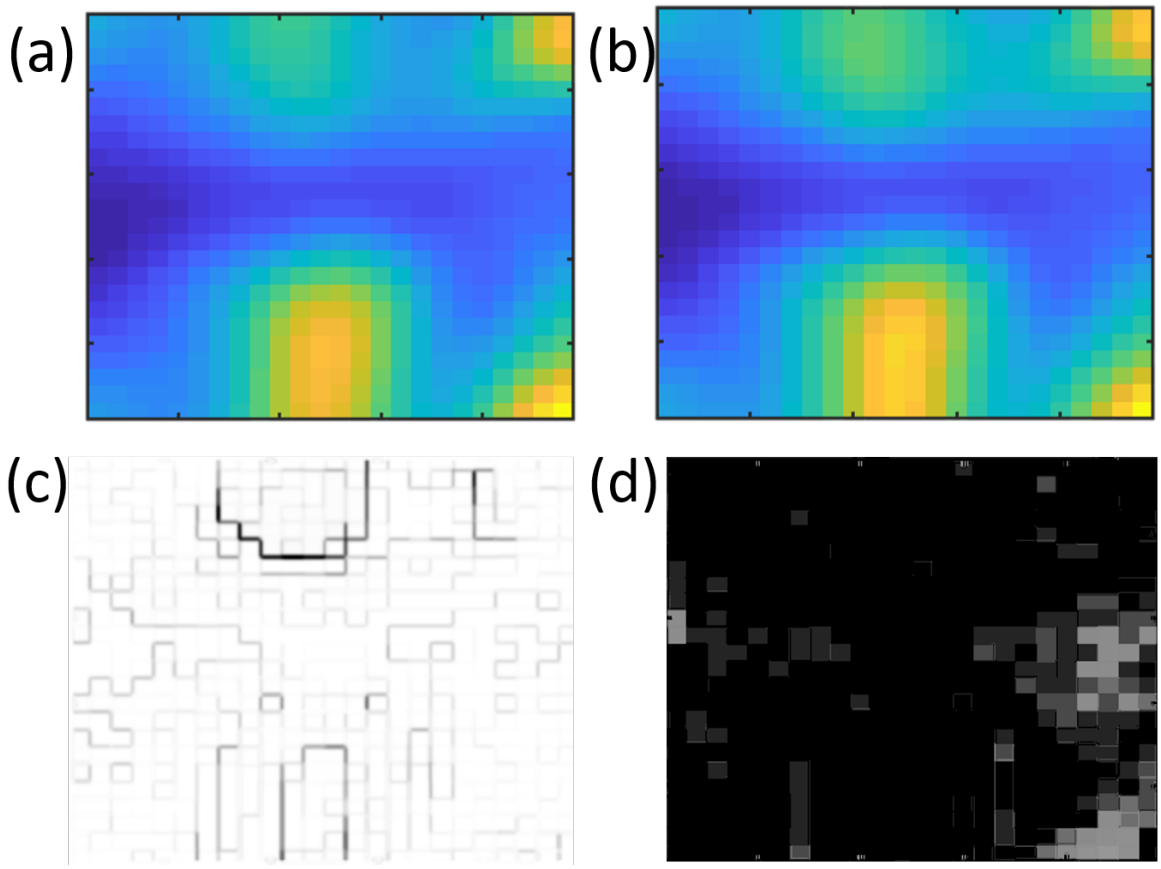

Figure B.3: Using Fig. 4.8, the differences between the power impression of the (a)tumor at location 2 and (b) tumor at location 3 are calculated using (c) SSIM map, where the shapes with darker edges show the differences, and (d) images subtraction technique, where the shapes with a lighter color indicate the differences. The percentage difference between images is: 2.1788%.

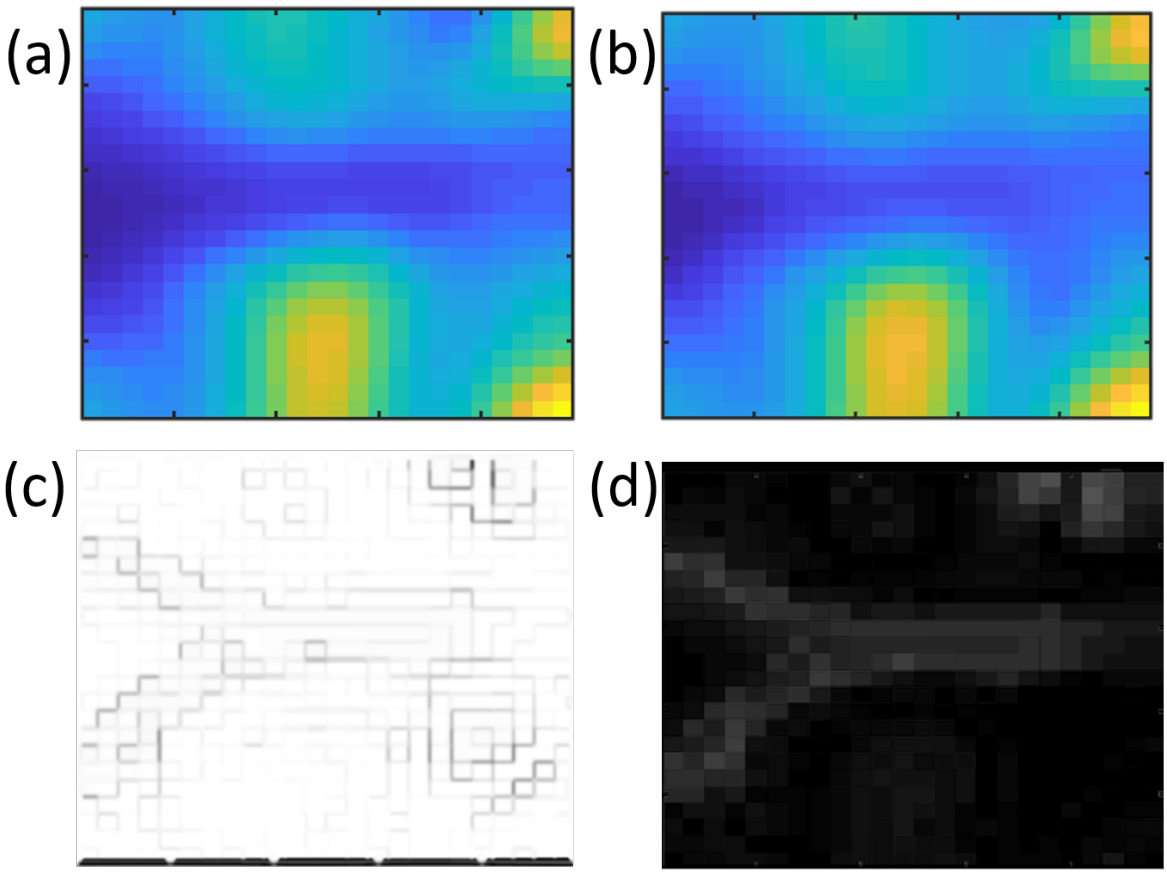

Figure B.4: Using Fig. 4.9, the differences between the power impression of the (a) tumor at depth 40 mm and (b) tumor at depth 50 mm are calculated using (c) SSIM map, where the shapes with darker edges show the differences, and (d) images subtraction technique, where the shapes with a lighter color indicate the differences. The percentage difference between images is: 2.0698%.

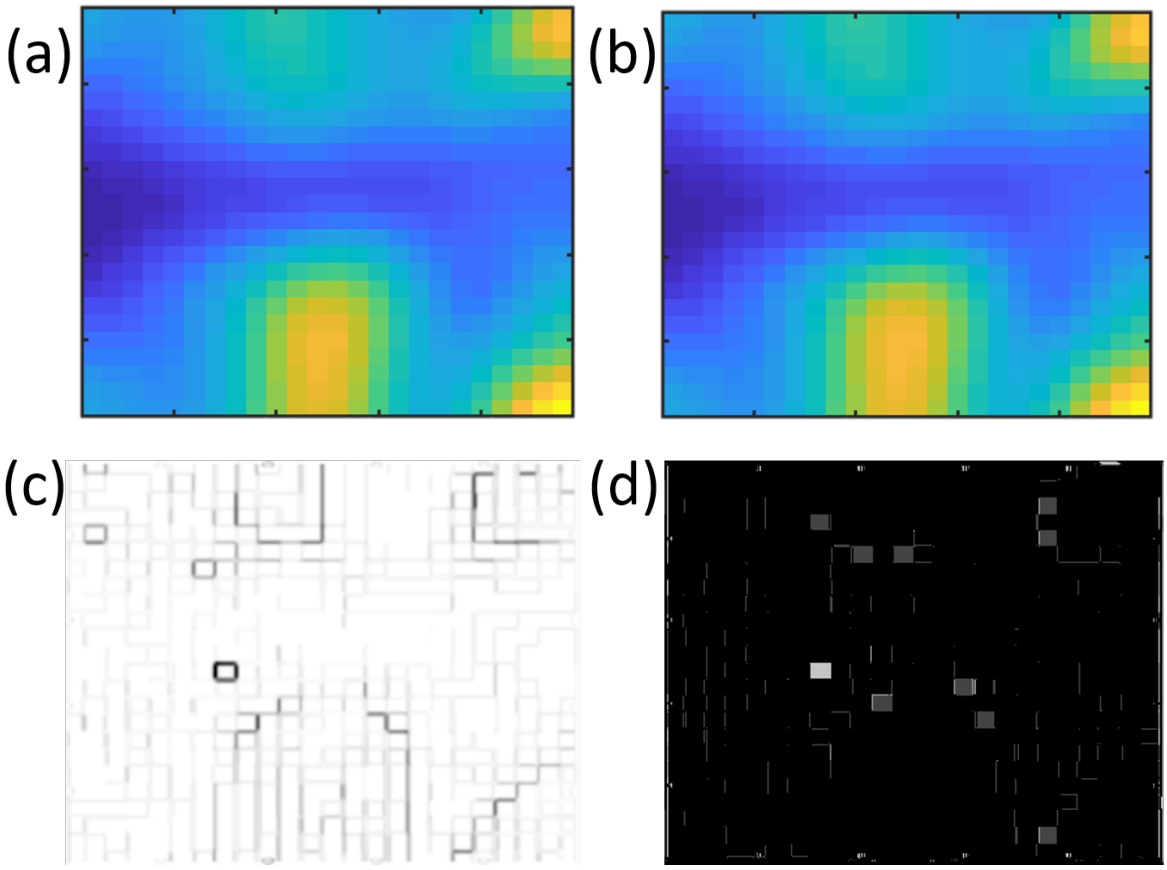

Figure B.5: Using Fig. 4.9, the differences between the power impression of the (a) tumor at depth 50 mm and (b) tumor at depth 60 mm are calculated using (c) SSIM map, where the shapes with darker edges show the differences, and (d) images subtraction technique, where the shapes with a lighter color indicate the differences. The percentage difference between images is: 0.60353%.

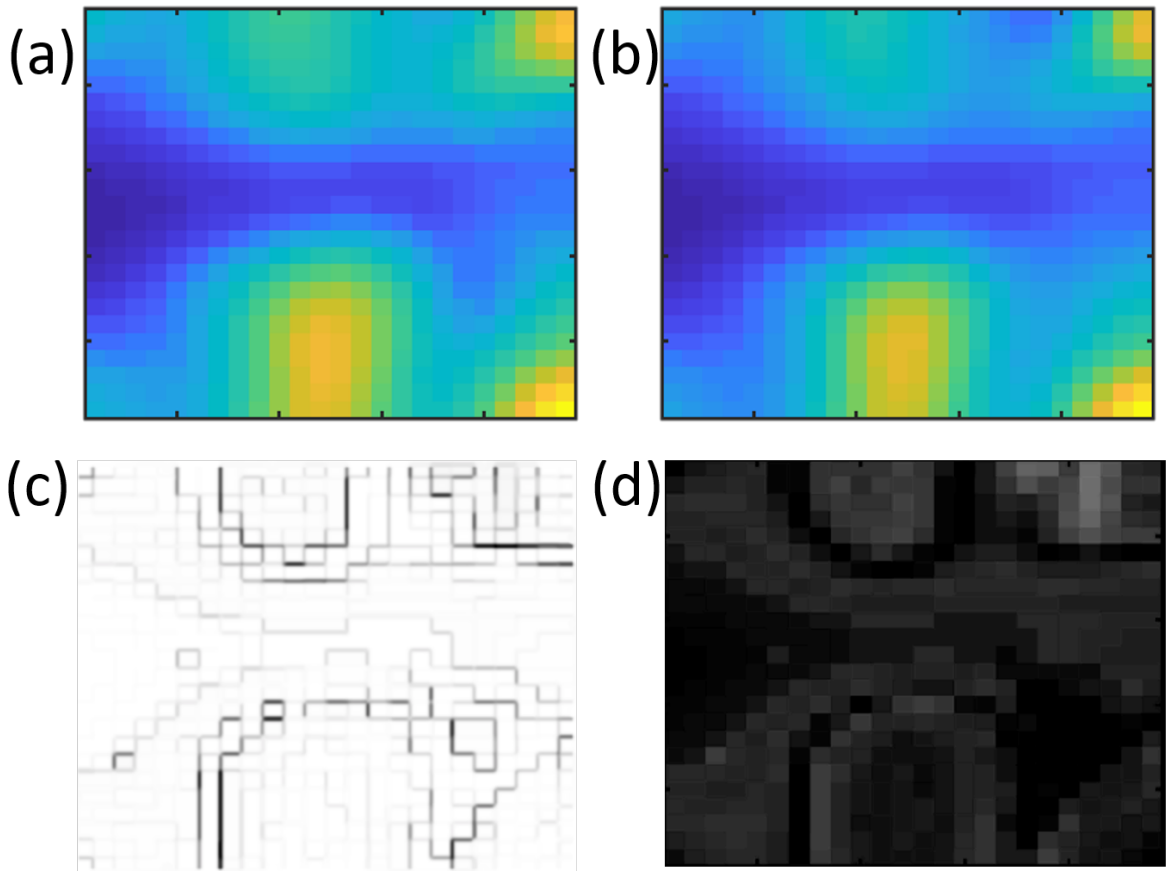

Figure B.6: Using Fig. 4.10, the differences between the power impression of the (a) 3 mm radius tumor and (b) 5 mm radius tumor are calculated using (c) SSIM map, where the shapes with darker edges show the differences, and (d) images subtraction technique, where the shapes with a lighter color indicate the differences. The percentage difference between images is: 3.2811%.

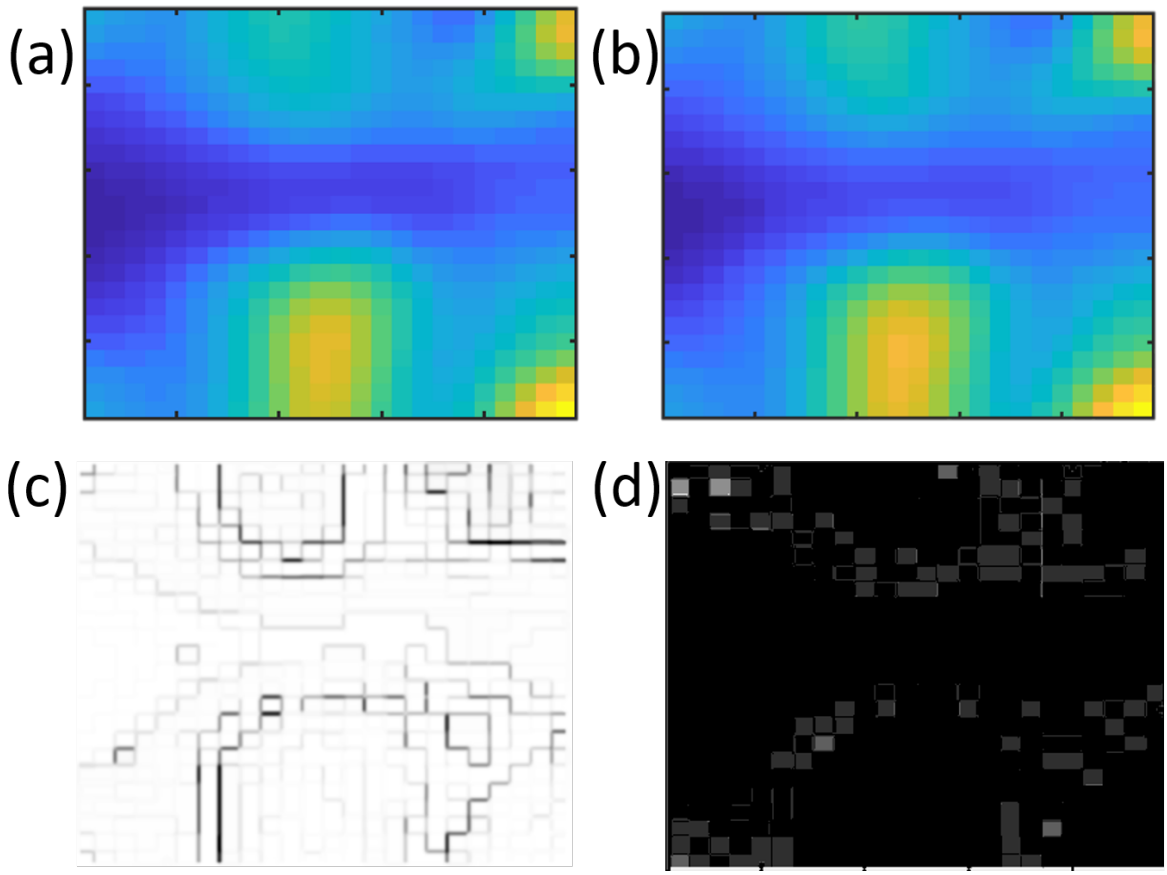

Figure B.7: Using Fig. 4.10, the differences between the power impression of the (a) 5 mm radius tumor and (b) 7.5 mm radius tumor are calculated using (c) SSIM map, where the shapes with darker edges show the differences, and (d) images subtraction technique, where the shapes with a lighter color indicate the differences. The percentage difference between images is: 1.5225%.

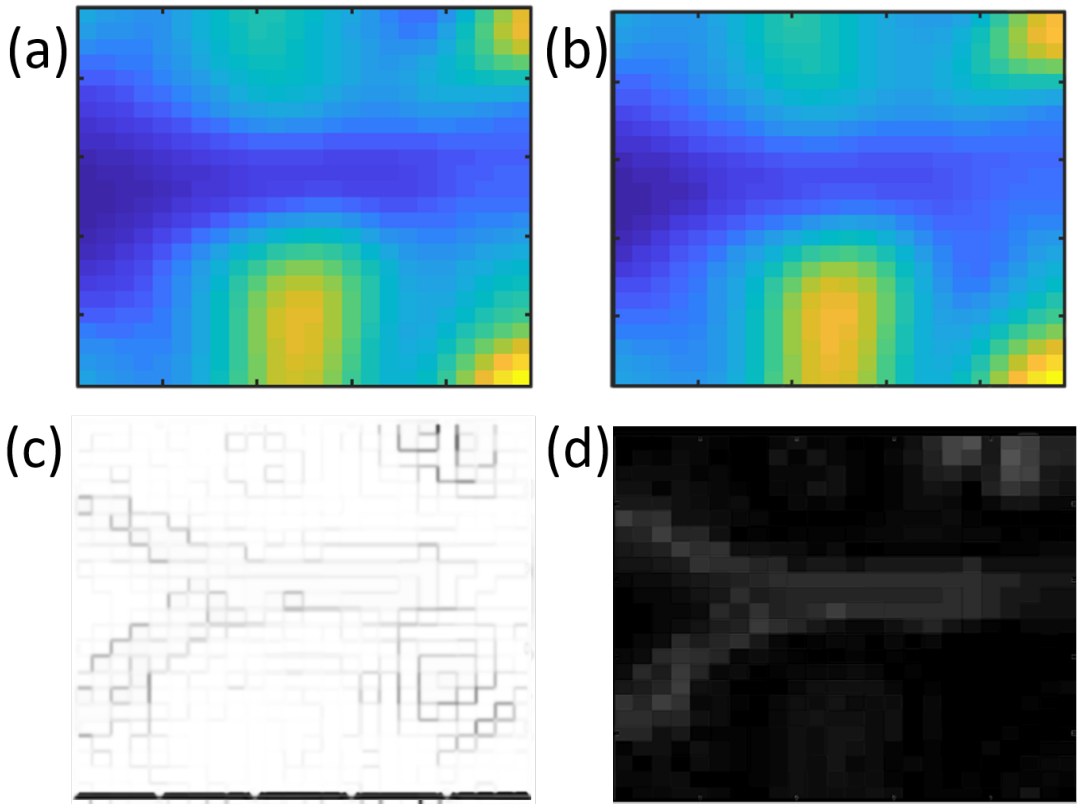

Figure B.8: Using Fig. 4.10, the differences between the power impression of the (a) 7.5 mm radius tumor and (b) 10 mm radius tumor are calculated using (c) SSIM map, where the shapes with darker edges show the differences, and (d) images subtraction technique, where the shapes with a lighter color indicate the differences. The percentage difference between images is: 1.7459%.